POLITECNICO DI TORINO

Master's Degree in Mechanical Engineering

Master's Degree Thesis

RANS simulation of neutral ABL flow over forested complex terrain with wind turbines

Supervisors:
Prof. Eliodoro CHIAVAZZO
Prof. Luca BERGAMASCO
Prof. Pietro ASINARI
Herbert OWEN

Graduate:
Fulvio FUCILE

Academic Year 2019/2020

Abstract

Nowadays wind energy represents one of the most exploited renewable energy sources in the world for generating electricity. During the last two decades, its use and the number of installed wind farms has increased drastically; this rapid growth, which is still ongoing, has led to an ever increasing search for new areas suitable to install WTs. Thus, in addition to the traditional wind energy sites, complex onshore ones have begun to be explored and at present, they are still being investigated. At the same time, many advances have been made in CFD techniques and numerical modeling has become a key tool for industry at several stages of wind farm design; in particular, in those terrains, characterized by a more varied topography and roughness, modeling of the wind flow conditions comes out to be more challenging. This is due to comparatively higher turbulence levels and wind shear, especially when the terrain is forested.
In this context, the present work describes the wind simulation framework for onshore wind farms and aims to perform a RANS simulation of neutral ABL flow over a real forested complex terrain with wind turbines; in particular, it focuses on an existing wind farm located at Rödeser Berg, near Kassel, in northern Hesse, Germany. The idea to participate in this project was born at Fraunhofer Institute for Wind Energy and Energy System Technology (IWES), in Kassel, Germany, who launched this challange to participants, providing input data and terrain information.
This thesis has been developed at the Spanish National Research Center, The Barcelona Supercomputing Center, by using Alya, an in-house High Performance Computing (HPC) multi-physics finite element parallel solver and by exploiting one of the most powerful supercomputer in Europe, the MareNostrum IV; in addition ParaView, a rendering program, and Google Earth have been used.

This thesis articulates in five chapters that are organized in this way:

The first chapter provides an overview about the worldwide development of wind energy, in terms of installed capacity of wind farms, over the last two decades; then it describes the working principle of a Horizontal Axis-WT and all the components which is made up of; after this brief introduction, it goes on by evaluating which are the most important factors to be considered during a preliminary site assessment, and by describing the main features of the site being analysed, the purpose of the measurement campaign and how it has been performed, and finally the importance of the benchmark for validating numerical models.

The second chapter describes the mathematical models that have been adopted, i.e the RANS and the standard-modified $k-\varepsilon$ turbulence one. Then it introduces and explains in detail all the corrections to be applied to the basic models to simulate

properly the windflow over this terrain; these modifications are related to the Coriolis force, forest effect, imposition of a neutral ABL and WTs insertion (simulated as discs). Finally the resulting model is presented, together with BCs to impose on the computational domain and the description of the iterative procedure.

The third chapter describes both surface and volume mesh generation procedure needed respectively to discretize the topography and terrain roughness and to resolve the ABL flow; then an alternative experimental approach is presented, which consists in rotating the mesh and reducing the computational domain; the final meshes, representing this complex terrain, have been generated by means of both methods and for different mesh cell sizes. In the end, the statistics of the meshes are compared.

The fourth chapter shows numerical results, in absence of WTs, at MetMast MM200 (vertical profiles), by comparing them with the experimental ones. Then, mesh convergence analysis is performed; eventually, the postprocess allows to visualise the wind field all over the terrain, at the ground and at different heights (horizontal planes).

The fifth chapter deals with the power generation; more in detail, it describes how to choose and position WTs, and the Alya mesh generation procedure adopted to insert them in the volume mesh computed previously. Then, also in this case, the numerical simulation (with WTs) is performed, which allows to compute both wind field all over the terrain and expected wind power production. Eventually it analyses the mesh convergence and carries out the postprocess, through which is possible to visualise the wake effects induced by WTs.

Acknowledgements

First of all, I would like to thank Prof. Asinari who gave me this opportunity and supported me during my stay and Prof. Chiavazzo and Prof. Bergamasco with whom I concluded the work; secondly Owen and all the BSC staff who helped me with the technical and bureaucratic aspects and finally Sarath Radhakrishnan who helped me in the initial training period.

This master thesis has received support from the European Union's Horizon 2020 research and innovation programme under grant agreement No 824158 (EoCoEII).

Contents

1 Introduction **1**

1.1 Worldwide wind energy data . . . 1
1.2 Working principle of a Horizontal Axis-WT . . . 2
1.3 Preliminary site assessment . . . 3
1.4 Site description . . . 5
1.5 Measurement campaign . . . 9
1.6 The Benchmark . . . 10

2 Governing equations **14**

2.1 RANS model . . . 15
2.2 $k - \varepsilon$ model . . . 20
2.3 Modifications to the basic models . . . 23
2.3.1 Coriolis force . . . 23
2.3.2 Forest effect . . . 24
2.3.3 Atmospheric Boundary Layer . . . 24
2.3.4 WTs effect: actuator disk theory . . . 28
2.4 Resulting model . . . 31
2.4.1 Boundary conditions . . . 32
2.4.2 Iterative procedure . . . 34

3 Surface and volume mesh generation **37**

3.1 Topography surface mesh . . . 38
3.2 ABL volume mesh . . . 44
3.3 An alternative experimental approach: rotated mesh and buffer impact 47
3.4 Statistics of the meshes . . . 52

4 Numerical simulation without WTs **55**

4.1 Results at met mast MM200 . . . 55
4.2 Convergence analysis . . . 65
4.3 Postprocess . . . 68

5 Power generation **81**

5.1 Choice of the WT and positioning . . . 81
5.2 Mesh generation of the wind farm: discs insertion . . . 84
5.3 Numerical simulation with WTs . . . 89
5.3.1 Results . . . 89
5.3.2 Convergence analysis . . . 89
5.3.3 Postprocess . . . 91

6 Conclusions **94**

List of Figures

1.1 Development of installed capacity in the world [1] 1
1.2 Annual new construction in MW in the world [1] 2
1.3 Wind turbine components [2] 3
1.4 Location of the Rödeser Berg site near Kassel, Germany 5
1.5 Rödeser Berg site: terrain height (topography) 6
1.6 Rödeser Berg site: terrain slope 7
1.7 Rödeser Berg site: terrain roughness 7
1.8 Rödeser Berg site: forest height and distribution 8
1.9 Wind rose at Rödeser Berg site [4] 8
1.10 Measurement area, transect and measurement device along it[5] . . . 9
1.11 WS and WP over the measurement area [5] 10
1.12 Experimental wind speed profile at MM200 [4] 11

2.1 Coriolis force, pressure gradient force and resulting path 23
2.2 Structure of the Atmospheric Boundary Layer over one diurnal cycle 25
2.3 Atmospheric stability: stable temperature gradient 26
2.4 Atmospheric stability: unstable temperature gradient 26
2.5 Atmospheric stability: stable, neutral and unstable profile of wind velocity 27
2.6 Inlet, rotor and outlet cross section [15] 29
2.7 Pressure and velocity airflow evolution through the WT [15] 29

3.1 Meshing process: topography, top view 39
3.2 Meshing process: topography, front zoom 39
3.3 Meshing process: domain regions 40
3.4 Meshing process: quadrilateral surface mesh, top view 41
3.5 Meshing process: quadrilateral surface mesh, zoom on the hill 42
3.6 Topography mesh generation: optimized surface mesh, top view . . . 43
3.7 Topography mesh generation: optimized surface mesh, zoom on the hill 44
3.8 ABL mesh generation: side view 46
3.9 ABL mesh generation: zoom inside the volume mesh 46
3.10 ABL mesh generation: quality of the hexahedral elements, top view . 47
3.11 Mesh rotation process without buffer: topography, top view 48
3.12 Mesh rotation process without buffer: domain regions 49
3.13 Rotated mesh without buffer: quadrilateral topography surface mesh, top view 50
3.14 Rotated mesh without buffer: quadrilateral topography surface mesh, zoom on the hill 50

3.15 Rotated mesh without buffer: optimized topography surface mesh, top view 51
3.16 Rotated ABL volume mesh without buffer: quality of the hexahedral elements, top view 51

4.1 Horizontal mean velocity profiles up to 2000 m: comparisons between 20m and 40m cell size for both meshing procedures 56
4.2 Horizontal mean velocity profiles up to 188 m: comparisons between 20m and 40m cell size for both meshing procedures 56
4.3 Wind direction profiles up to 2000 m: comparisons between 20m and 40m cell size for both meshing procedures 57
4.4 Wind direction profiles up to 188 m: comparisons between 20m and 40m cell size for both meshing procedures 57
4.5 TKE profiles up to 2000 m: comparisons between 20m and 40m cell size for both meshing procedures 58
4.6 TKE profiles up to 188 m: comparisons between 20m and 40m cell size for both meshing procedures 58
4.7 Pressure profiles up to 2000 m: comparisons between 20m and 40m cell size for both meshing procedures 59
4.8 Pressure profiles up to 188 m: comparisons between 20m and 40m cell size for both meshing procedures 59
4.9 Horizontal mean velocity profiles up to 2000 m: comparisons between 30m and 60m cell size for both meshing procedures 60
4.10 Horizontal mean velocity profiles up to 188 m: comparisons between 30m and 60m cell size for both meshing procedures 60
4.11 Wind direction profiles up to 2000 m: comparisons between 30m and 60m cell size for both meshing procedures 61
4.12 Wind direction profiles up to 188 m: comparisons between 30m and 60m cell size for both meshing procedures 61
4.13 TKE profiles up to 2000 m: comparisons between 30m and 60m cell size for both meshing procedures 62
4.14 TKE profiles up to 188 m: comparisons between 30m and 60m cell size for both meshing procedures 62
4.15 Pressure profiles up to 2000 m: comparisons between 30m and 60m cell size for both meshing procedures 63
4.16 Pressure profiles up to 188 m: comparisons between 30m and 60m cell size for both meshing procedures 63
4.17 Convergence trend of both momentum and continuity equation for the non-rotated mesh with 30m cell size 66
4.18 Convergence trend of both k and dissipation ε equation for the non-rotated mesh with 30m cell size 66
4.19 Convergence trend of both momentum and continuity equation for the rotated mesh with 30m cell size 67
4.20 Convergence trend of both k and dissipation ε equation for the rotated mesh with 30m cell size 67
4.21 Postprocess: Horizontal mean velocity field around the ABL for the non-rotated mesh with buffer and 30m cell size 68

4.22 Postprocess: Horizontal mean velocity field at the ground for a non-rotated mesh with buffer and 30m cell size 68
4.23 Postprocess: pressure field around the ABL for the non-rotated mesh with buffer and 30m cell size 69
4.24 Postprocess: pressure field at the ground for the non-rotated mesh with buffer and 30m cell size 69
4.25 Postprocess: TKE (k) field around the ABL for the non-rotated mesh with buffer and 30m cell size 70
4.26 Postprocess: TKE (k) at the ground for the non-rotated mesh with buffer and 30m cell size 70
4.27 Postprocess: Dissipation rate ε field around the ABL for the non-rotated mesh with buffer and 30m cell size 71
4.28 Postprocess: Dissipation rate ε at the ground for the non-rotated mesh with buffer and 30m cell size 71
4.29 Postprocess: Horizontal mean velocity field around the ABL for the rotated mesh without buffer and 30m cell size 72
4.30 Postprocess: Horizontal mean velocity field at the ground for the rotated mesh without buffer and 30m cell size 72
4.31 Postprocess: pressure field around the ABL for the rotated mesh without buffer and 30m cell size 73
4.32 Postprocess: pressure field at the ground for the rotated mesh without buffer and 30m cell size 73
4.33 Postprocess: TKE (k) field around the ABL for the rotated mesh without buffer and 30m cell size 74
4.34 Postprocess: TKE (k) field at the ground for the rotated mesh without buffer and 30m cell size 74
4.35 Postprocess: Dissipation rate ε field around the ABL for the rotated mesh without buffer and 30m cell size 75
4.36 Postprocess: Dissipation rate ε field at the ground for the rotated mesh without buffer and 30m cell size 75
4.37 Postprocess: Horizontal mean velocity field for the non-rotated mesh at 60 m height w.r.t MM200 76
4.38 Postprocess: Horizontal mean velocity field for the non-rotated mesh at 70 m height w.r.t MM200 76
4.39 Postprocess: Horizontal mean velocity field for the non-rotated mesh at 80 m height w.r.t MM200 77
4.40 Postprocess: Horizontal mean velocity field for the non-rotated mesh at 105 m height w.r.t MM200 77
4.41 Postprocess: Velocity speed-up field for the non-rotated mesh at 60 m height w.r.t MM200 78
4.42 Postprocess: Velocity speed-up field for the non-rotated mesh at 70 m height w.r.t MM200 78
4.43 Postprocess: Velocity speed-up field for the non-rotated mesh at 80 m height w.r.t MM200 79
4.44 Postprocess: Velocity speed-up field for the non-rotated mesh at 105 m height w.r.t MM200 79

5.1 Power curve of Vestas V90-3MW [7] 82

5.2 Mesh generation of the wind farm: ABL volume mesh and regions to be removed . . . 84
5.3 Mesh generation of the wind farm: disc generation and meshing . . . 85
5.4 Mesh generation of the wind farm: upwind/downstream disc mesh . . 86
5.5 Mesh generation of the wind farm: upwind/downstream disc mesh . . 87
5.6 Mesh generation of the wind farm: splitting upwind/downstream mesh 88
5.7 Convergence trend of both momentum and continuity equation for the final hybrid mesh . . . 90
5.8 Convergence trend of both k and dissipation ε equation for the final hybrid mesh . . . 90
5.9 Postprocess: Horizontal mean velocity field (modulus only) for the final hybrid mesh at 105 m (hub height) w.r.t MM200 . . . 91
5.10 Postprocess: Horizontal mean velocity field (vectors) for the final hybrid mesh at 105 m (hub height) w.r.t MM200 . . . 92
5.11 Postprocess: Velocity speed-up field for the final hybrid mesh at 105 m (hub height) w.r.t MM200 . . . 92

List of Tables

1.1 Provided data at MM200 [4] 11

3.1 Statistics of the meshes: non-rotated mesh with buffer 53
3.2 Statistics of the meshes: non-rotated mesh with buffer 53
3.3 Statistics of the meshes: rotated mesh without buffer 53
3.4 Statistics of the meshes: rotated mesh without buffer 53

4.1 Experimental data at MM200 64
4.2 Numerical results at MM200 64
4.3 Relative errors in percentage at MM200 65

5.1 Technical specifications of Vestas V90-3MW [8] 82
5.2 C_t and C_p values as function of U_∞ 83
5.3 WTs locations 83
5.4 Statistics of the final hybrid mesh 88
5.5 Numerical results at the four Vestas V90-3MW 89

Nomenclature

WT	Wind Turbine
WTs	Wind Turbines
TKE	Turbulent Kinetic Energy
ABL	Atmospheric Boudary Layer
LAD	Leaf Area Density
PAD	Plant Area Density
NEWA	New European Wind Atlas
CFD	Computational Fluid Dynamics
w.r.t	with respect to
BCs	Boundary Conditions
RANS	Reynolds Averaged Navier–Stokes

Chapter 1

Introduction

Over the last two decades, the theme of global pollution, cause of the continous and rapid climate changes, has become so relevant that it can no longer be neglected; more specifically, air pollution, caused by the large amount of fossil fuels used and their associated greenhouse gas emissions, has experienced worrying levels; in this sense, renewable energies represent the key factor to improve air quality and human health and, at the same time, their use, especially on a large scale, allow to achieve the required energy targets.
For this reason, many countries are making a step change to set their own economies on a low-carbon and resource-efficient policy; as a consequence, renewable energy consumption has increased fastly, thanks also to the falling costs.
In particular, among the possibile green solutions, wind energy is surely one of the most widespread and exploited.

1.1 Worldwide wind energy data

Wind energy systems, infact, have been extensively studied and greatly improved during these years; this has therefore led to the construction of ever more performing wind turbines and of an higher number of wind farms, both onshore and offshore, that traduces in a higher value of installed capacity.
Figure 1.1 shows the increasing trend of installed capacity over eighteen years; looking more closely, it has risen from 17,4 GW in 2000 to almost 540 GW at the end of 2017.

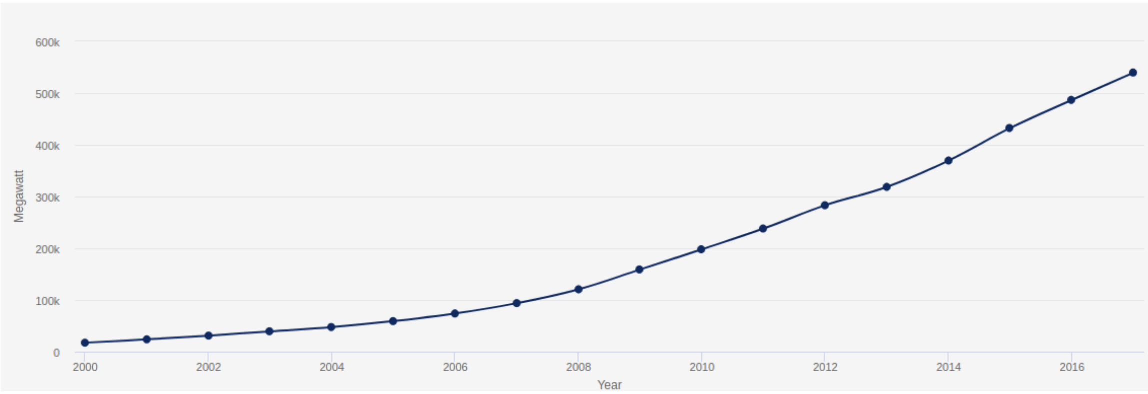

Figure 1.1: Development of installed capacity in the world [1]

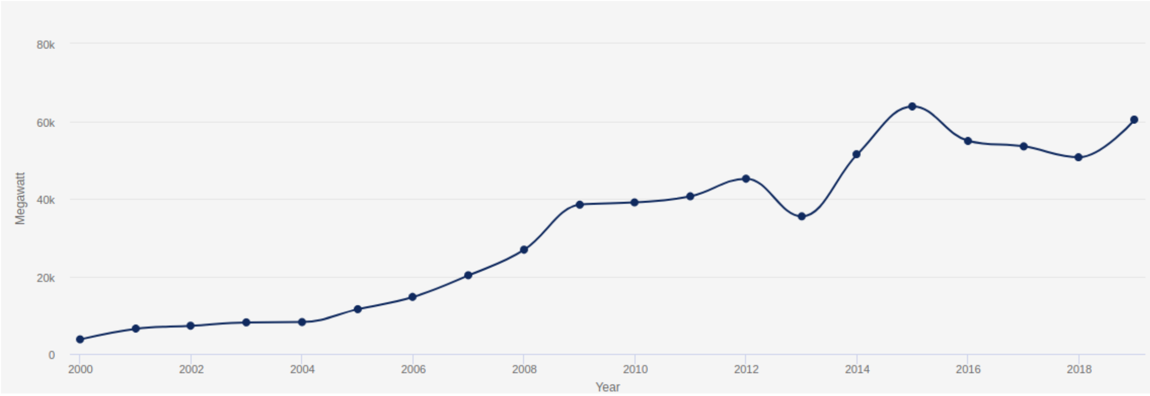

Figure 1.2: Annual new construction in MW in the world [1]

Figure 1.2, instead, shows the increment of installed capacity from 2000 until 2019, on a yearly basis. Only in 2019, it was around 60 GW.

1.2 Working principle of a Horizontal Axis-WT

When dealing with wind farms, to be intented as wind applications on medium or large scale, one important aspect to specify right away is that WTs are always of the type horizontal axis; in contrast, for small and residential wind applications, vertical axis ones are used. This is basically due to the difference in size between the two, and consequently in the performance, since they are strictly correlated; in fact, the higher the dimension of the WT, the higher will be the performance in terms of output power. Moreover, as it can be easily guessed, the former refer to a horizontal rotating axis while the latter to a vertical one.
After this brief explanation about the main distinction between them and their usage, considering that the present work concerns a really existing wind farm, for now on, the horizontal axis WTs will be indicated for simplicity as WTs.
The way they operate, from an energetic point of view is pretty simple; they harness the kinetic energy carried by the wind to generate the electrical one. More in detail, the wind turns the rotor, comprising the blades and the hub, which in turn, through a gear box that works as a speed increaser, spins an induction generator so as to produce electricity. This one, through the cabling inside the tower, is sent to a transformer station, then to the grid and finally to users.
Here below, figure 1.3 provides a detailed view of a WT and its components. It is worthwhile to specify that WT shown here, as well as the ones used in this work, always refer to upwind turbines, since the rotor is positioned on the windward side of the tower.

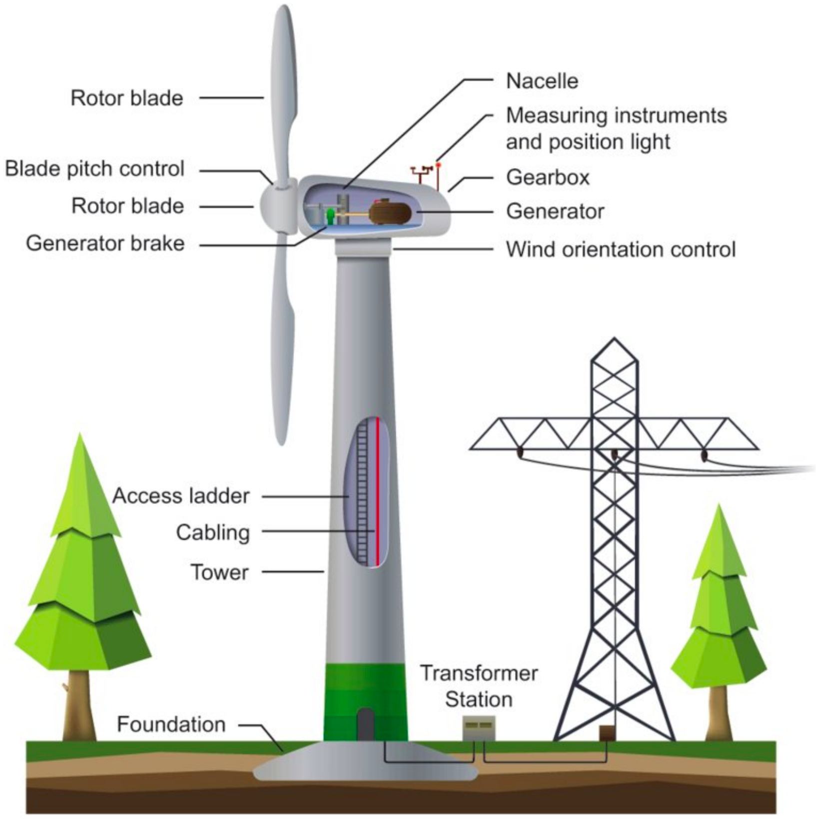

Figure 1.3: Wind turbine components [2]

The nacelle, which is located at the top of the tower, contains the gear box, with the low and high-speed shafts, and the generator plus some other devices, i.e the controller and brake. During operation, in fact, wind conditions such as speed or direction can vary, even drastically, and so monitoring and consequently adapting WT to the different working conditions is fundamental, for the safety of the WT itself but also to maximise energy production. For these reasons, the blade pitch control, which allows the rotation of the blades around the pitch axis, and a yaw drive, through the rotation around the yaw one, enable to orient the rotor and to maintain the proper blade angle in order to achieve optimal rotor speed, while the brake and the controller are used respectively to stop the rotor mechanically or electrically, in case of emergency, i.e for high wind speeds (around 25 m/s) and to activate the WT in the opposite situation, i.e when wind speeds are too low for economically viable operation; usually an anemometer is used to measure the wind speed.

1.3 Preliminary site assessment

When it comes to designing a wind farm, the first step to do, clearly, is to choose the appropriate site where it has to be built; this represents a crucial aspect for future project developments, from both a technical and financial point of view; however it is worthwhile to specify that the present work does not analyse the economical aspects but only the technical ones. Anyway, the choice is not straightforward but it requires some basic initial considerations.

The most important aspect to consider is the wind potential associated with the site; the more the site is ventilated and the wind speeds are high, the more the site will be suitable for the construction of a wind farm; this is because the power generated by each single WT, by definition, is proportional to the cube of the wind speed.
In this sense, the wind potential strongly varies whether the site is onshore or offshore; the latter usually experiences higher and more consistent wind speeds than the former; this is basically due to the absence of obstacles (e.g buildings, trees, hilly, mountain), which cause friction, that consequently leads to a reduction of the wind speed. For this reason, in case of onshore sites, large open fields would be preferred to valleys or forested and hilly/mountainous terrains; but in the last two cases, when required, since the wind speed is proportional to the height, the wind farm should be placed on the top of the hill/mountain rather than at the bottom; in this way it is possible to compensate for the wind speed reduction. However, this represents in any case a common practice, because regardless the presence of obstacles, the terrain itself, even when it is flat, provides friction, slowing the wind flow at low heights.
All these terrains, i.e hilly, mountainous, and/or forested, and more precisely all those characterized by strong variations of the orography and roughness, are classified as complex terrains.
Another relevant aspect to be taken into account is the atmospheric turbulence, which can be defined as the set of seemingly random and continuously changing air motions that are superimposed on the wind's average motion. Turbulence can be quantified with a metric called turbulence intensity, that's the standard deviation of the horizontal wind speed divided by the average wind speed over some time period, typically 10 minutes, or with the turbulence kinetic energy (TKE), that's based on the squares of the variations in velocities. The standard deviations of all three components of the flow are squared, summed together and divided by two. Typical values of TKE range from 0.05 m^2/s^2 at night to 4 m^2/s^2 or greater during the day[3]; most of the time, TKE is preferred because both the horizontal and vertical components of the flow are considered, allowing in this way to get a better estimation of the turbulence, especially when the contribution of the vertical component is strong. However, they both give an idea of how much the wind fluctuates in a certain time period; therefore, the more the wind fluctuations are rapid the more the turbulence will be high.
It is generated by friction and interactions between air flows and ground surface, and it affects wind energy in several ways, specifically through power performance effects, impacts on turbine loads, fatigue and wake effects, and noise propagation[3]. It can be due to the solar radiation, in the morning and/or afternoon, which heats the ground that in turns warms the air above, causing that to rise, or due to the presence of canopy; this one infact causes a wind speed reduction below the canopy level itself and the strong difference in speed with the wind flowing above that, leads to an increasing wind shear and consequently turbulence.
Besides, in complex terrain, it can be even more enhanced than in flat onshore or offshore sites, because wind flow, due to directional variations in terrain, is continously deflected, causing turbulent wakes next to and downwind of the obstacle. On the top of these evaluations, and considering that all these phenomena occur contemporary, turbulence varies along the height, tending to be higher near the ground

surface, where it typically generates, than at high altitudes, but also during the day. Some other minor aspects are related to the amount of physical space available, to the structural stability of the soil (when onshore), and to the accessibility to the site for an easy construction, ongoing operations, maintenance and overall safety. All these preliminary evaluations can be done by having access to existing data from topographic maps, state wind resource maps, nearby publicly available wind resource data, and other weather measurement sites so as to make a rough estimation of the site suitability and so of the feasibility of the project.
The state wind resource maps, in fact, provide informations about wind power class at different sites; the wind power classes are seven, and each one defines the wind speed range and turbulence level at different heights; but, despite this, the main issue is that those data are characterized by a relatively large uncertainty and so they should not be used to make a detailed evaluation. For this reason, once the promising site to install wind turbines is choosen, a more detailed wind resource site assessment is required; this is usually performed through a field campaign on site.

1.4 Site description

At this point, after this brief overview about some general technical aspects concerning the choice of the site, the present work focuses on an existing wind farm located in Rödeser Berg, that's a forested hill 379 m above mean sea level, in northern Hesse, Germany. This work comes from a challenge, launched by Fraunhofer Institute for Wind Energy and Energy System Technology (IWES), in Kassel, Germany, which first performed a measurement campaign on site (named "NEWA Forested Hill Experiment Kassel") and then asked to participants to simulate some real wind flow conditions (obtained from field measurement), by means of proper numerical modelling methods.

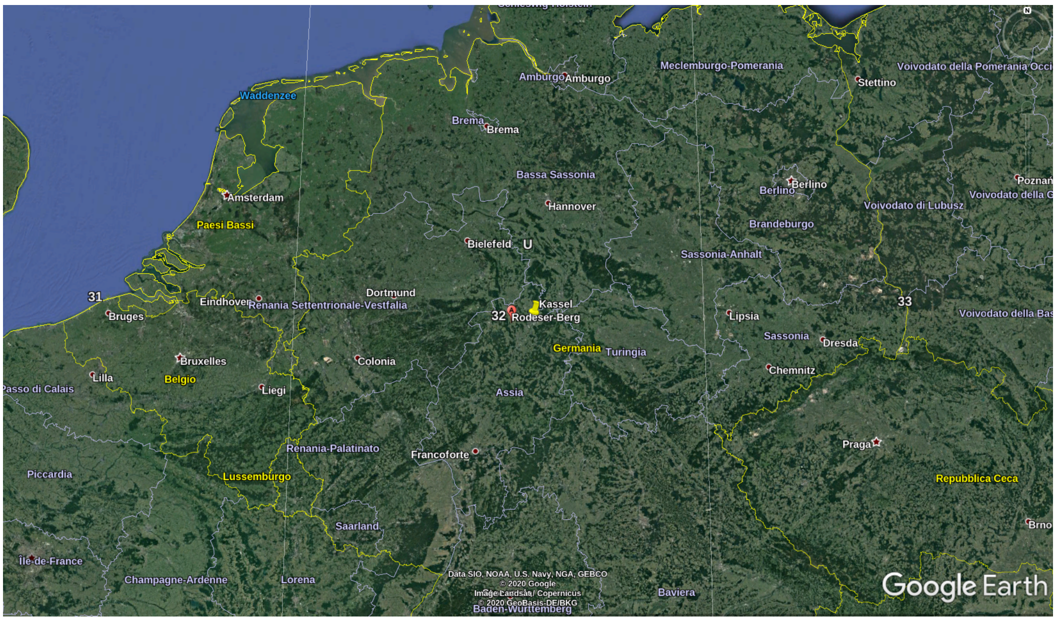

Figure 1.4: Location of the Rödeser Berg site near Kassel, Germany

What's really interesting about the Rödeser Berg site, which is located 20 km northwest of Fraunhofer IWES, is that it is a forested hilly terrain, and so, due to its peculiar topography and roughness, is classified as a slightly complex terrain. In this sense, the aim of the present work is to model properly the wind flow over complex terrains. The region being analysed, extends over an area of approximately 10x10 km2, and the terrain height varies from a maximum of 400m at the Rödeser Berg hill to a minimum of 200m in the surrounding area.In general, the terrain surrounding Rödeser Berg site is very heterogeneous.
Furthermore, the terrain is not entirely forested but it consists of a patchy landscape of mainly agricultural land use, forest and some settlements; for this reason the terrain roughness is not homogenous, but it varies over the whole site. All terrain information, i.e terrain height, inclination and roughness, forest heigh and LAD, has been provided by the Fraunhofer IWES, through files in netCDF or CSV format and with 10x10 m resolution; then, these files have been also managed and converted into kml format, so as to display them on Google Earth for a clearer view.
Here below, figures 1.5, 1.6 and 1.7 show respectively the terrain height, slope and roughness; figure 1.8 instead represents the forest height and its distribution over the terrain. As it can be noted, in each figure, there is an inner region and an outer one. The former, centered in the Rödeser Berg hill, is the wind farm region, where the measurement campaign has been performed and it covers an area of 5x5 km. The latter, instead, which is set to be homogeneous and flat (no forest), is used to delimit the wind farm region and to drive the numerical simulation. This concept is explained more in detail in the Chapter 3, related to the mesh generation.

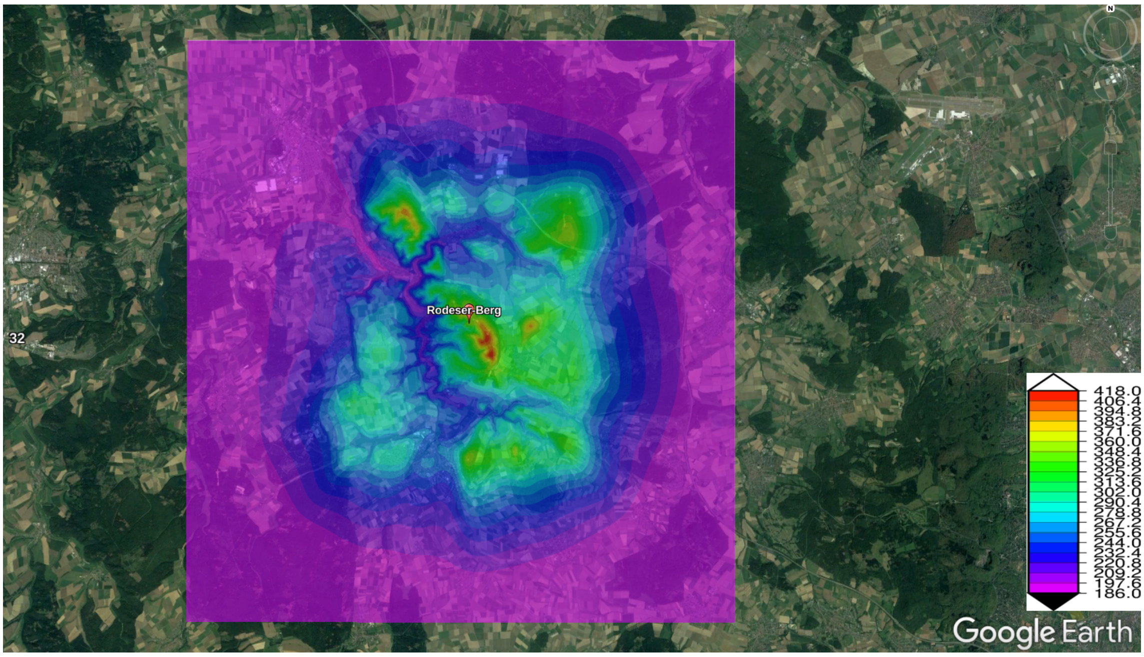

Figure 1.5: Rödeser Berg site: terrain height (topography)

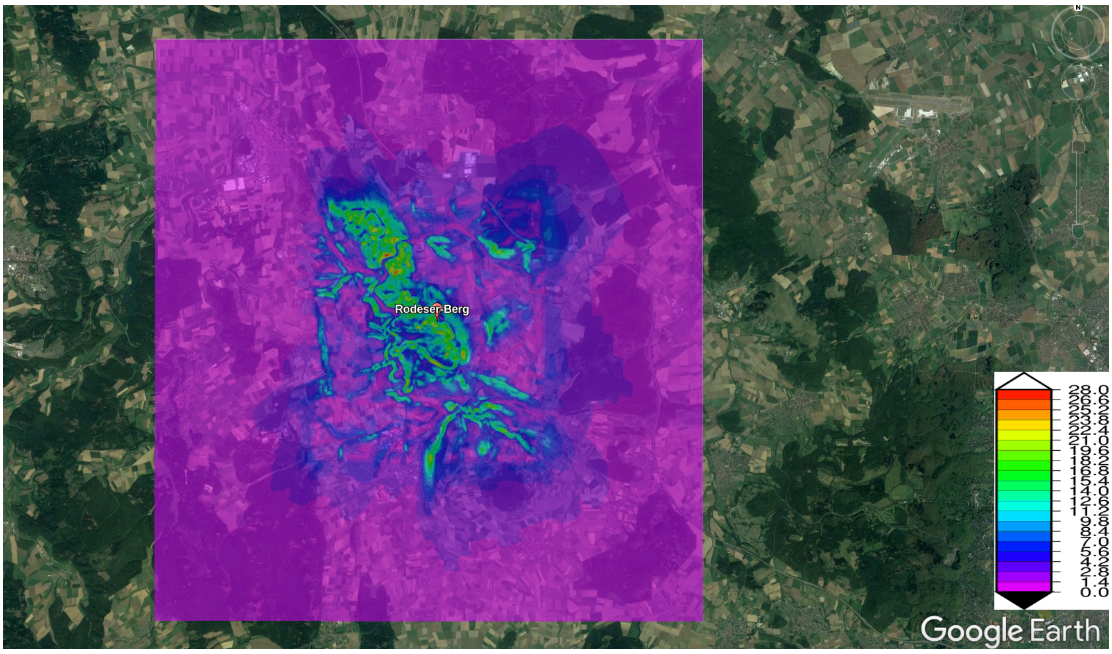

Figure 1.6: Rödeser Berg site: terrain slope

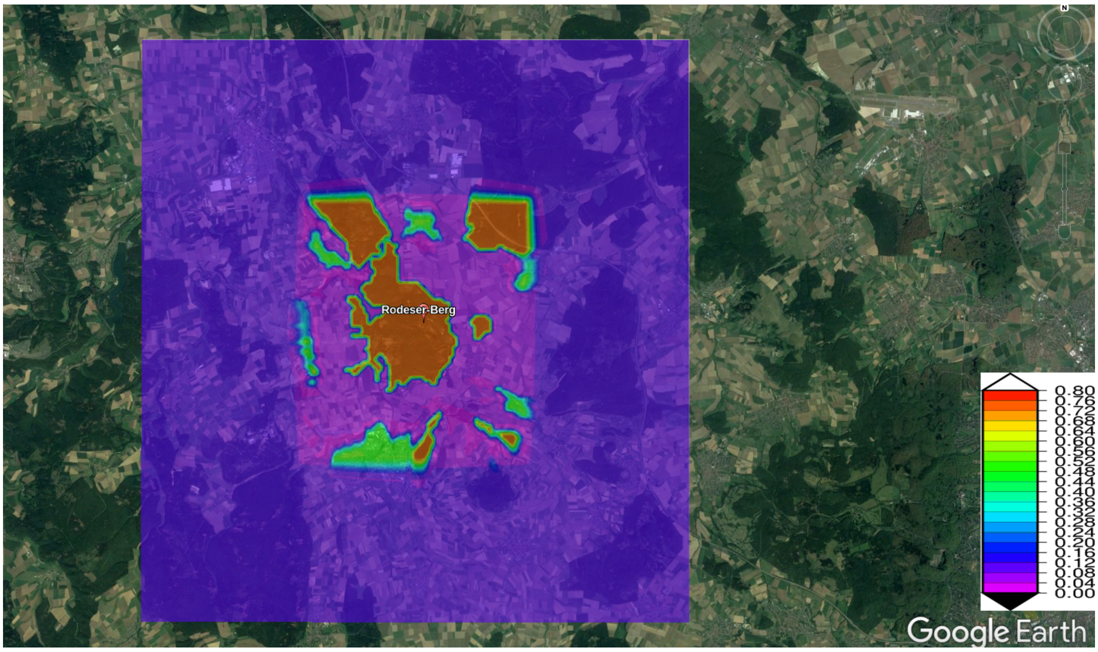

Figure 1.7: Rödeser Berg site: terrain roughness

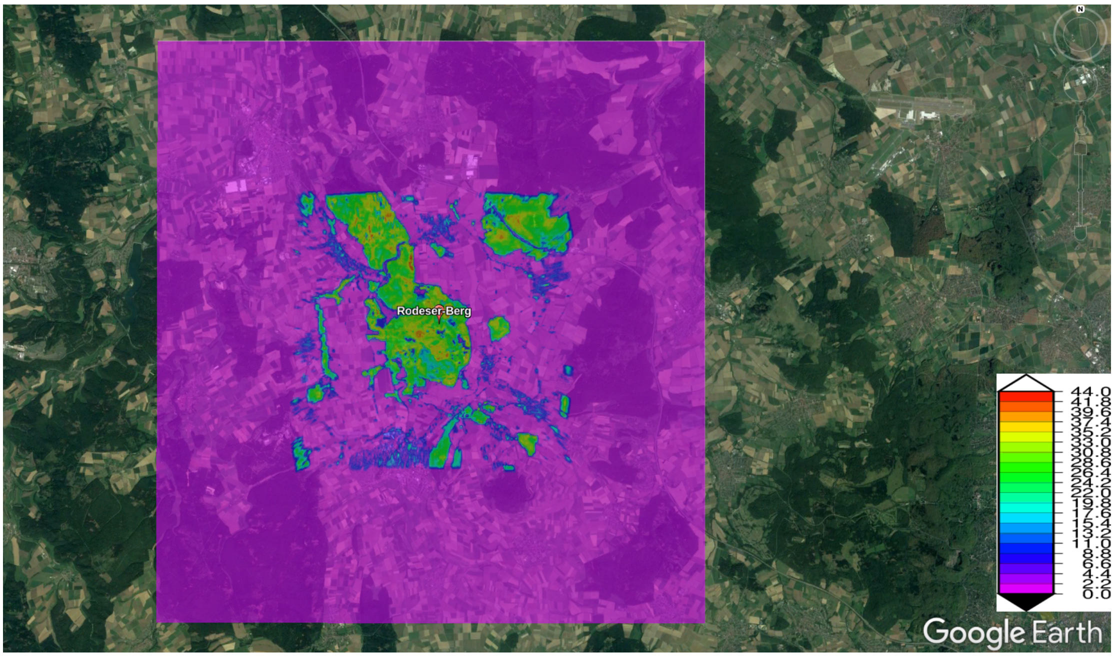

Figure 1.8: Rödeser Berg site: forest height and distribution

Another fundamental aspect to be considered, for both the measurement campaign and the numerical simulation, is represented by the wind flow direction; this one, in fact, changes continously in time and with height. The problem is that, dealing with a variable wind direction would make impossibile to perform any kind of measurement or simulation. For this reason, it is common practice to evaluate what is called wind rose, through which it is possible to determine the prevailing wind direction. Here below figure 1.9 shows the wind rose at Rödeser Berg site. The prevailing wind direction is 217°.

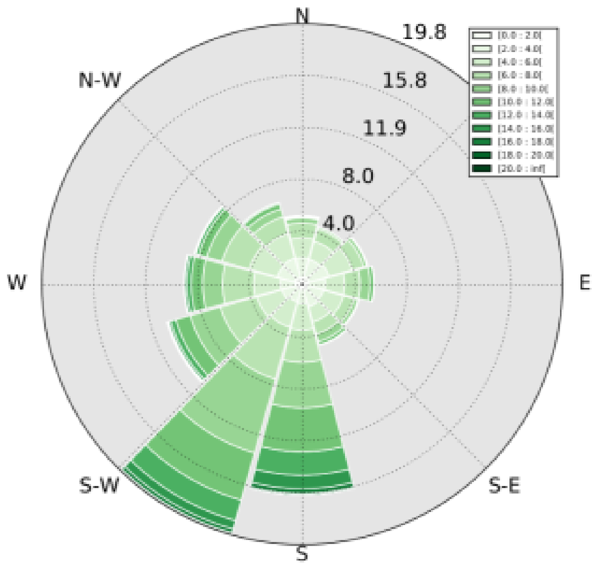

Figure 1.9: Wind rose at Rödeser Berg site [4]

1.5 Measurement campaign

The field measurement consisted of a 3 month intensive campaign and a 1 year long-term campaign from November 2016 to October 2017. The main target was to capture and map the flow over (from hundreds of meters to few km) and all around the ridge of the forested hill in the prevailing wind direction, i.e 217°[4]; so, in order to accomplish this task, a 5.5 km long transect along that direction (217°, counted clockwise against north) has been chosen and then probed with a dense array of instrumentation[5]. The hill is aligned orthogonal with respect to the transect.
In total 17 wind measurement systems have been used: 9 long-range Doppler scanning lidars (four of the nine scanning lidars pairwise performed multi-lidar scans), 6 lidar/sodar vertical wind profilers and 2 tall met masts. The 1 year long-term campaign, with two tall masts, started in parallel to the intensive campaign.
Both meteorological masts, MM200 and MM140, with heights of respectively 200 m and 140 m, were equipped with sonic and cup anemometers at multiple levels; the first represents the origin of the transect [UTMX=513590, UTMY=5690182, 32U] and is used to measure the vertical wind profile and turbulence conditions at the top of Rödeser Berg while the second, used to determine the inflow conditions, is the initial point of the transect, i.e the point from which the flow crossing the hill is spatially resolved.
Here below figure 1.10 shows some measurement sites, such as MM140, MM200, WP1 and WP5; the red circle, centered in MM200, delimits the whole measurement area, while the green line represents the transect inclined of 217°.

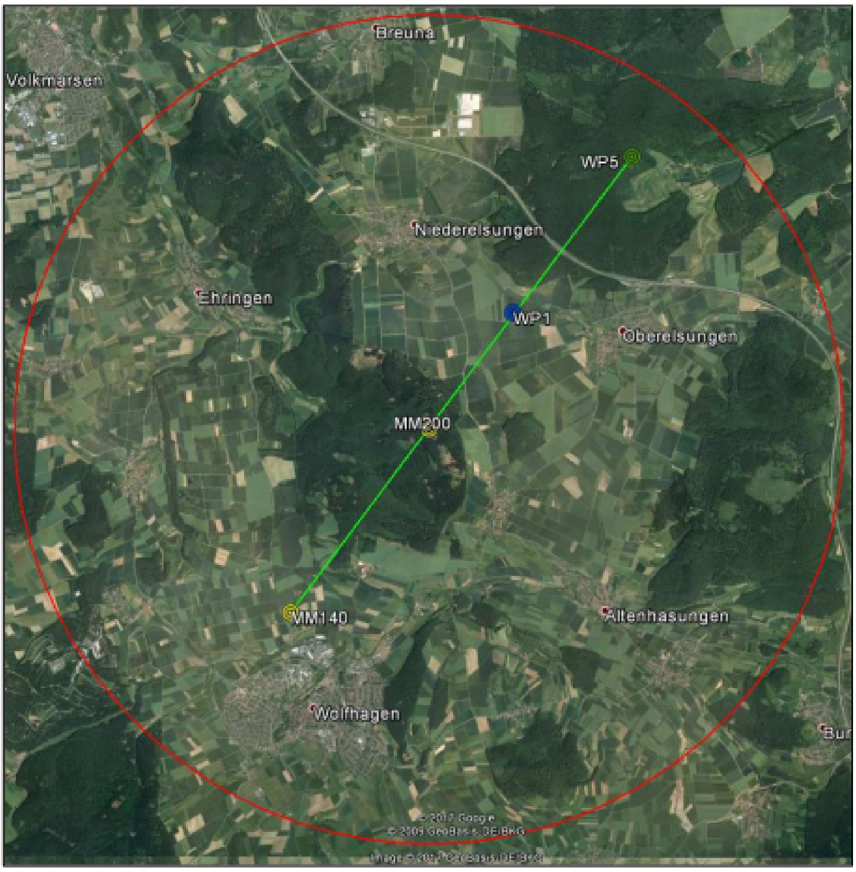

Figure 1.10: Measurement area, transect and measurement device along it[5]

(a) WS

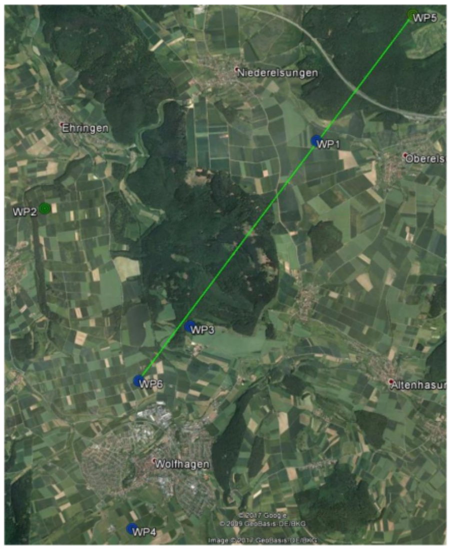

(b) WP

Figure 1.11: WS and WP over the measurement area [5]

Here above, instead, figures 1.11(a) and 1.11(b) show the positions of all the other measurement devices, indicated as WP (lidar profiler) and WS (lidar scanner). Their name depend on the function they assolve, ie respectively wind profiler and wind scanning.

Centering the transect at MM200 allows to split it into two parts so as evaluate the flow upwind and downwind of the hill. Actually, at the beginning of the experiment a wind farm, on top of the Rödeser Berg, was already installed. It consists of four Enercon E-101-3,05 MW turbines[5]. The present work, instead, considers four Vestas V90-3MW.

1.6 The Benchmark

The aim of the benchmark, consists of determining how well the micro-scale model adopted is able to simulate the wind flow over a terrain, which is, in this particular case, forested and complex; this is done by trying to match the measured wind profiles in specified conditions with the numerical ones. The task was to model numerically the wind flow over the Rödeser Berg site (in the prevailing wind direction), in stationary condition with neutral stratification by using the wind velocities and directions measured at 60m and 188m above the ground level, at metmast MM200, which is the only reference.

On the next page, figure 1.12 shows the experimental wind speed profile at MM200 (from the ground up to 200m), provided by the Fraunhofer IWES. An important aspect to specify is that this wind condition holds for 30 min only, from 11:20 to 11:50 on 17.11.2016 and the reason for which this one is being analysed is strictly related to the ABL stratification, which is neutral. This concept is better explained in section 2.3.3, named ABL.

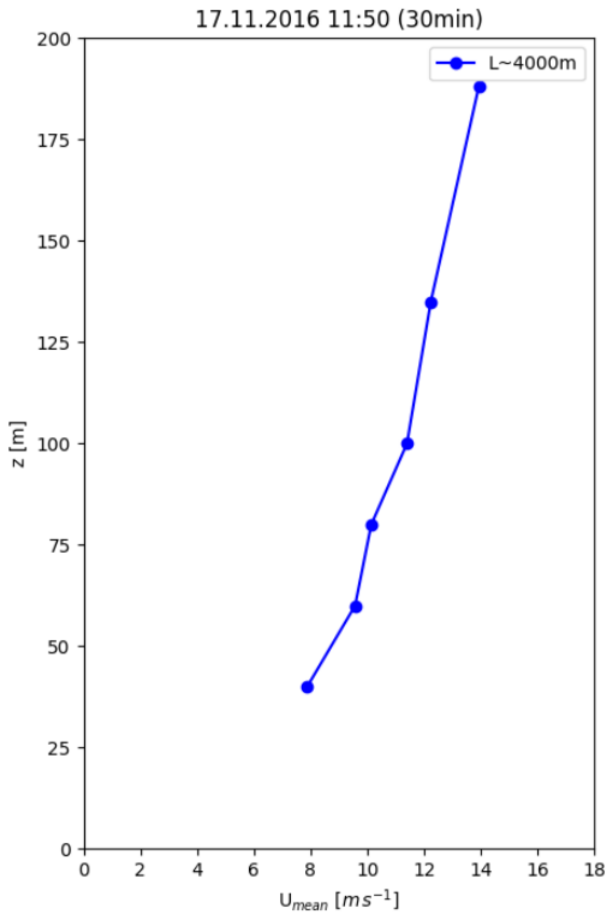

Figure 1.12: Experimental wind speed profile at MM200 [4]

The table below, indicates the experimental wind speed and direction values at MM200, at two different heights, for this particular condition. The high value of the OL instead, is representative of the neutral stratification. The choice to have target wind speeds and directions within the first 200 m above the ground, rather than referring to geostrophic values, was partly due to the lack of measurements and partly to the desire to analyse wind variables, as precisely as possible, in that part of the boundary layer (the lowest one), where turbulence and the forest effect are more enhanced; in fact, by setting a fixed geostrophic wind speed, there would be the risk to under or overestimate the modelled wind speed w.r.t the measured one, in the surface layer.

	at 60 m	at 188 m
Wind speed	9.6 m/s	13.9 m/s
Wind direction	219.7°	221.7°
Obukhov Length	4000 m	-

Table 1.1: Provided data at MM200 [4]

In particular, it was asked to match the wind speed profile at MM200 and those two wind velocities and directions, and to compare the wind flow conditions found experimentally with the ones obtained numerically, at different locations, so as to validate the numerical model. Unfortunately experimental data have not been published yet and even on the NEWA website (https://map.neweuropeanwindatlas.eu/) micro-scale data can't be downloaded. For this reason the present work aims to match the wind speed profile at MM200 and then, through the postprocess, it shows the behaviour of the wind flow all over the terrain at those two heights.

Chapter 2

Governing equations

After performing a preliminary site assessment, choosing the site where wind farm will be built and carrying out the measurement campaign, the following stage of wind resource assessment, consists in defining the mathematical model in order to simulate properly the wind flow, that is in this case over a complex terrain.
In this context, the existing CFD modeling strategies can be grouped in two main categories, i.e Large Eddy Simulation (LES) and Reynolds Averaged Navier–Stokes (RANS).
In particular, LES models have been introduced recently with promising results, but they are still costly at wind farm scales and difficult to converge to a statistical steady state solution; basically, they focus on the behaviour of the largest eddies and, at the same time, allow to approximate also the smallest ones by modeling the effect of the unresolved scale.
In contrast, RANS ones, provide a steady-state solution and are widely used in research and industry due to its trade-off between accuracy and computational cost.
The present work has been developed using Alya, a finite-element multi-physics parallel solver, which solves the Reynolds Averaged Navier–Stokes (RANS) equations using a standard $k - \varepsilon$ turbulence model, modified according to Apsley and Castro[9]; this modification is applied to limit the turbulent length scale, so as to adapt the resulting model to the particular ABL. Besides, it is also well known that, when WTs are present, RANS equations with the standard $k-\varepsilon$ model significantly overestimates Reynolds stresses [11] behind actuator discs, resulting on a enhanced underestimation of velocities and on an excessive wake damping.
Furthermore, in order to perform the simulation correctly and so to get numerical results as accurate as possible, several other aspects must be taken account such as the presence of a (patchy) canopy, the effect induced by the WTs, and the Coriolis effect. Therefore, to understand in detail how the two basic models are modified, this chapter firstly describes the RANS and standard $k - \varepsilon$ turbulence model, secondly analyse all the corrections to be made to models and finally it presents the resulting model and BCs to be used to perform the simulation, together with the description of the iterative procedure adopted.

2.1 RANS model

The Navier-Stokes equations, expressed in tensor (or index) notation and in conservative form, for an incompressible isothermal Newtonian fluid, are:

$$\frac{\partial u_i}{\partial x_i} = 0 \tag{2.1}$$

$$\rho\frac{\partial u_i}{\partial t} + \rho\frac{\partial}{\partial x_j}(u_i u_j) = -\frac{\partial p}{\partial x_i} + \frac{\partial}{\partial x_j}(2\mu s_{ij}) \tag{2.2}$$

These two equations, i.e (1)-(2), represent respectively the continuity and momentum equation; where $i, j = 1, 2, 3$ and the strain-rate tensor s_{ij} is given by:

$$s_{ij} = \frac{1}{2}(\frac{\partial u_i}{\partial x_j} + \frac{\partial u_j}{\partial x_i}) \tag{2.3}$$

and substituting Eq. (3) in (2), the momentum equation can be written as:

$$\rho\frac{\partial u_i}{\partial t} + \rho\frac{\partial}{\partial x_j}(u_i u_j) = -\frac{\partial p}{\partial x_i} + \mu\frac{\partial^2 u_i}{\partial x_i \partial x_j} \tag{2.4}$$

and dividing it by ρ:

$$\frac{\partial u_i}{\partial t} + \frac{\partial}{\partial x_j}(u_i u_j) = -\frac{1}{\rho}\frac{\partial p}{\partial x_i} + \nu\frac{\partial^2 u_i}{\partial x_i \partial x_j} \tag{2.5}$$

Equations (1) and (5) can be expressed also in matrix form as:

$$\nabla \cdot \boldsymbol{u} = 0 \tag{2.6}$$

$$\frac{\partial \boldsymbol{u}}{\partial t} + \nabla \cdot (\boldsymbol{u}\boldsymbol{u}) = -\nabla(\frac{p}{\rho}) + \nu\nabla^2\boldsymbol{u} \tag{2.7}$$

Equivalently, Eq. (4) can be written as:

$$\frac{\partial(\rho\boldsymbol{u})}{\partial t} + \nabla \cdot (\rho\boldsymbol{u}\boldsymbol{u}) = -\nabla p + \nabla \cdot \boldsymbol{\tau} \tag{2.8}$$

whereas:

$$\nabla \cdot (\boldsymbol{u}\boldsymbol{u}) = \boldsymbol{u} \cdot \nabla\boldsymbol{u} + \boldsymbol{u}(\nabla \cdot \boldsymbol{u}) \tag{2.9}$$

and considering Eq. (6), it becomes

$$\nabla \cdot (\boldsymbol{u}\boldsymbol{u}) = \boldsymbol{u} \cdot \nabla \boldsymbol{u} \tag{2.10}$$

So Eq. (5) and (7) can be re-written as:

$$\frac{\partial u_i}{\partial t} + u_j \frac{\partial u_i}{\partial x_j} = -\frac{1}{\rho}\frac{\partial p}{\partial x_i} + \nu \frac{\partial^2 u_i}{\partial x_i \partial x_j} \tag{2.11}$$

$$\frac{\partial \boldsymbol{u}}{\partial t} + \boldsymbol{u}\nabla \cdot \boldsymbol{u} = -\nabla(\frac{p}{\rho}) + \nu \nabla^2 \boldsymbol{u} \tag{2.12}$$

It is worthwhile to remind that Navier Stokes equations written above refer to instantaneous quantities (instantaneous velocity u_i and pressure p); at this point, the idea is to focus on the mean behavior of the flow rather than resolving the fluctuating quantities as it would require very fine meshes and small time-steps; this is done by resorting to the Reynolds decomposition, which allows to separate the flow variable (like velocity, or pressure) into the mean (time-averaged) and the fluctuating component.
This tool is quite useful, especially, in turbulent flows, where the field properties become random functions of space and time. Hence, the field variables u_i and p must be expressed as the sum of mean and fluctuating parts as:

$$u_i(x_i, t) = U_i(x_i, t) + u_i'(x_i, t), \quad p(x_i, t) = P(x_i, t) + p'(x_i, t) \tag{2.13}$$

Now, considering that the most interesting part between the two is the time average-mean value, the next step is to compute $\overline{u_i} = \lim_{T\to\infty} \frac{1}{T}\int_{t_0}^{t_0+T}(U_i + u_i')dt$ where the bar is indicating the average operator, and the mean and fluctuating parts satisfy (mean of the fluctuating quantity is equal to zero)

$$\overline{u_i} = U_i, \quad \overline{u_i'} = 0 \tag{2.14}$$

$$\overline{p} = P, \quad \overline{p'} = 0 \tag{2.15}$$

Here, T represents the averaging interval. This interval must be large compared to the typical time scales of the fluctuations so it will yield to a stationary state.

Therefore, the application of time averaging (or Reynolds averaging), clearly, traduces in a statistical approach to turbulence modeling, and in fact is appropriate for stationary turbulence or slowly varying turbulent flows, i.e., a turbulent flow that, on average, does not vary much with time. It is important to notice that the distinction between steady or unsteady flow has not made yet; the time average, in fact, can be either in time or iterative. This basically means that by taking the average between different ranges or values of t, the mean value will be approximately the same.
Now, inserting Eq. (13) into (1)-(2), and taking the mean part (time averaged) only, the two equations are written as:

$$\frac{\partial U_i}{\partial x_i} = 0 \tag{2.16}$$

$$\rho \frac{\partial U_i}{\partial t} + \rho \frac{\partial}{\partial x_j}(U_i U_j) = -\frac{\partial P}{\partial x_i} + \frac{\partial}{\partial x_j}(2\mu S_{ij} - \rho \overline{u_i' u_j'}), \tag{2.17}$$

where S_{ij} is the mean strain-rate tensor

$$S_{ij} = \frac{1}{2}(\frac{\partial U_i}{\partial x_j} + \frac{\partial U_j}{\partial x_i}) \tag{2.18}$$

So inserting Eq. (18), the momentum equation becomes

$$\rho \frac{\partial U_i}{\partial t} + \rho \frac{\partial}{\partial x_j}(U_i U_j) = -\frac{\partial P}{\partial x_i} + \frac{\partial}{\partial x_j}(\mu \frac{\partial U_i}{\partial x_j} - \rho \overline{u_i' u_j'}), \tag{2.19}$$

The two terms on the left hand side of this equation represent the change in mean momentum of a fluid element owing to the unsteadiness in the mean flow and the convection by the mean flow. This change is balanced by the isotropic stress owing to the mean pressure field, the viscous stresses, and apparent stress owing to the fluctuating velocity field, generally referred to as the Reynolds stress.
The quantity $\boldsymbol{\tau}_{ij}^R = -\rho \overline{u_i' u_j'}$ is known as the Reynolds stress tensor and it represents an added stress contribution to the fluid (it is symmetric and thus has six components).
It is is a convective term, which is independent of viscosity; it depends only on turbulent flow field and is the responsible for the increased mixing and larger wall shear stresses (which are properties of turbulent flows). Instead, the last two term of Eq. (19) represent together τ_{ij}, i.e the total shear stress, which considers both viscosity and Reynolds stress tensor contribution:

$$\tau_{ij} = \mu \frac{\partial U_i}{\partial x_j} - \rho\overline{u_i' u_j'} \tag{2.20}$$

Now dividing by ρ and considering that $\nu = \mu/\rho$, it becomes:

$$\frac{\partial U_i}{\partial t} + \frac{\partial}{\partial x_j}(U_i U_j) = -\frac{1}{\rho}\frac{\partial P}{\partial x_i} + \frac{\partial}{\partial x_j}(\nu \frac{\partial U_i}{\partial x_j} - \overline{u_i' u_j'}) \tag{2.21}$$

and then, recalling Eq. (10):

$$\frac{\partial U_i}{\partial t} + U_j \frac{\partial U_i}{\partial x_j} = -\frac{1}{\rho}\frac{\partial P}{\partial x_i} + \nu \frac{\partial^2 U_i}{\partial x_i \partial x_j} - \frac{\partial \overline{u_i' u_j'}}{\partial x_j} \tag{2.22}$$

or equivalently:

$$\frac{\partial U_i}{\partial t} + U_j \frac{\partial U_i}{\partial x_j} = -\frac{1}{\rho}\frac{\partial P}{\partial x_i} + \nu \frac{\partial^2 U_i}{\partial x_i \partial x_j} + \frac{1}{\rho}\frac{\partial \tau_{ij}^R}{\partial x_j} \tag{2.23}$$

and in the matrix form Eq.(23) becomes:

$$\frac{\partial \boldsymbol{U}}{\partial t} + \boldsymbol{U}\nabla \cdot \boldsymbol{U} = -\nabla(\frac{p}{\rho}) + \nu\nabla^2 \boldsymbol{U} + \frac{1}{\rho}\nabla \cdot \boldsymbol{\tau}^R \tag{2.24}$$

At this point, it is important to specify that by dropping the time derivative in the governing equations, turbulence will be steady; otherwise, if the time derivative is kept, turbulence will be unsteady.
The Reynolds-averaged approach to turbulence modeling requires that the Reynolds stress term, which is nonlinear, in Eq. (22), be appropriately modeled to close the RANS equation for solving. A common method employs the Boussinesq hypothesis to relate the Reynolds stress tensor to the mean strain rate tensor (therefore to the mean velocity gradient):

$$\tau_{ij}^R = -\rho\overline{u_i' u_j'} = 2\mu_T S_{ij} - \frac{2}{3}\rho k \delta_{ij} \tag{2.25}$$

or in matrix form as:

$$\boldsymbol{\tau}^R = -\rho\overline{\boldsymbol{u'}\boldsymbol{u'}} = \mu_T[\nabla \boldsymbol{U} + (\nabla \boldsymbol{U})^T] - \frac{2}{3}\rho k \boldsymbol{I} \tag{2.26}$$

where δ_{ij} is the Kronecker delta, $\boldsymbol{I}$ is the identity matrix and the turbulence kinetic energy, k, is defined as:

$$k = \frac{1}{2}\overline{\boldsymbol{u}'\boldsymbol{u}'} = \frac{1}{2}(\overline{u'^2} + \overline{v'^2} + \overline{w'^2}) \tag{2.27}$$

where u, v and w are the three istantaneous velocity component and $\nu_T = \mu_T/\rho$ is the kinetic (or tubulent) eddy viscosity assumed as an isotropic scalar quantity. Now, recalling Eq. (23)-(24) and substituting respectively Eq. (25)-(26) inside them, the two equations written using the index notation and in matrix form become:

$$\frac{\partial U_i}{\partial t} + U_j \frac{\partial U_i}{\partial x_j} = -\frac{1}{\rho}[\frac{(\partial P + \partial \frac{2}{3}\rho k)}{\partial x_i}] + \frac{\partial}{\partial x_j}[\frac{1}{\rho}(\mu + \mu_T)\frac{\partial U_i}{\partial x_j}] \tag{2.28}$$

$$\frac{\partial \boldsymbol{U}}{\partial t} + \boldsymbol{U}\nabla \cdot \boldsymbol{U} = -\frac{1}{\rho}(\nabla P + \frac{2}{3}\rho \nabla k) + \nabla \cdot [\frac{1}{\rho}(\mu + \mu_T)\nabla \boldsymbol{U}] \tag{2.29}$$

Once the equations have been averaged and Boussinesq approximation introduced into them, the simplified RANS model can be written as:

$$\nabla \cdot \boldsymbol{u} = 0 \tag{2.30}$$

$$\frac{\partial \boldsymbol{u}}{\partial t} + \boldsymbol{u} \cdot \nabla \boldsymbol{u} - \nabla \cdot (\nu_t \nabla^s \boldsymbol{u}) + \nabla(\frac{p}{\rho}) = 0 \tag{2.31}$$

whereas the turbulent eddy viscosity is modeled as:

$$\nu_t = C_\mu \frac{k^2}{\varepsilon} \tag{2.32}$$

By decomposing the instantaneous properties into mean and fluctuating parts, three unknown quantities have been introduced, but, unfortunately, there are no additional equations gained; therefore, this means the system is not yet closed and so to obtain the closure of the problem, the $k - \varepsilon$ turbulence model is introduced.

2.2 $k-\varepsilon$ model

Most of the time, flows occurring in nature and in engineering applications, are turbulent. Defining turbulence is quite complicated and a proper model has to be used. Turbulence is irregular and random and so it requires to be treated with a statistical approach; it occurs for high Reynolds number $Re = \frac{uL}{\nu}$ and causes high levels of fluctuating vorticity; it is always dissipative and the viscous shear stresses degrade the kinetic energy of the flow.
The standard $k-\varepsilon$ model is a semi-empirical model based on model transport equations for the turbulence kinetic energy k and its dissipation rate ε. In the derivation of the $k-\varepsilon$ model, it was assumed that the flow is fully turbulent, and the effects of molecular viscosity are negligible. The standard $k-\varepsilon$ model is therefore valid only for fully turbulent flows (high Reynolds number).
Despite this two equation model is very robust and widely used, it is also well-established that it requires an additional mixing length limitation model and appropriate model constants to adapt to the ABL flow and so to accurately predict wind intensity profiles; besides the Coriolis effect is fundamental and it must be taken into account. For this reason the closure turbulence model used in this work is the standard-modified $k-\varepsilon$ model. The two equations for the turbulence kinetic energy and (specific) dissipation rate are:

$$\frac{\partial k}{\partial t} + U_j \frac{\partial k}{\partial x_j} = \tau_{ij} \frac{\partial U_i}{\partial x_j} - \varepsilon + \frac{\partial}{\partial x_j}[(\nu + \nu_t/\sigma_k)\frac{\partial k}{\partial x_j}] \tag{2.33}$$

$$\frac{\partial \varepsilon}{\partial t} + U_j \frac{\partial \varepsilon}{\partial x_j} = C_1 \frac{\varepsilon}{k} \tau_{ij} \frac{\partial U_i}{\partial x_j} - C_2 \frac{\varepsilon^2}{k} + \frac{\partial}{\partial x_j}[(\nu + \nu_t/\sigma_\varepsilon)\frac{\partial \varepsilon}{\partial x_j}] \tag{2.34}$$

where the kinetic eddy viscosity is modeled as before:

$$\nu_t = C_\mu \frac{k^2}{\varepsilon} \tag{2.35}$$

Eq. (33)-(34) can be also expressed in matrix form as:

$$\frac{\partial k}{\partial t} + \boldsymbol{U} \cdot \nabla k = \tau^R : \nabla \boldsymbol{U} - \varepsilon + \nabla \cdot [(\nu + \frac{\nu_t}{\sigma_k})\nabla k] \tag{2.36}$$

$$\frac{\partial \varepsilon}{\partial t} + \boldsymbol{U} \cdot \nabla \varepsilon = C_1 \frac{\varepsilon}{k} \tau^R : \nabla \boldsymbol{U} - C_2 \frac{\varepsilon^2}{k} + \nabla \cdot [(\nu + \frac{\nu_t}{\sigma_\varepsilon})\nabla \varepsilon] \tag{2.37}$$

The two terms on the left hand side of (33)-(34), or equivalently of (36)-(37), represent the change in TKE and dissipation rate of a fluid element owing to the unsteadiness in the mean flow and the convection by the mean flow; the terms instead on the right hand side of both equations, from left to right, represent respectively the production, dissipation and diffusion term.
They have been manipulated so there are no terms including velocity fluctuations, besides the Reynolds stress tensor and the turbulence dissipation rate. Also in this case, the Reynolds stress tensor is modeled using the Boussinesq approximation.
The simplified equation for TKE, in matrix form can be written as:

$$\frac{\partial k}{\partial t} + \boldsymbol{u} \cdot \nabla k - \nabla \cdot (\frac{\nu_t}{\sigma_k} \nabla k) + \frac{C_\mu}{\nu_t} k^2 = P_k \tag{2.38}$$

and inserting Eq. (35), it becomes:

$$\frac{\partial k}{\partial t} + \boldsymbol{u} \cdot \nabla k - \nabla \cdot (\frac{\nu_t}{\sigma_k} \nabla k) = P_k - \varepsilon \tag{2.39}$$

whereas the equation for dissipation rate is:

$$\frac{\partial \varepsilon}{\partial t} + \boldsymbol{u} \cdot \nabla \varepsilon - \nabla \cdot (\frac{\nu_t}{\sigma_\varepsilon} \nabla \varepsilon) + \frac{C_2}{k} \varepsilon^2 = C_1' C_\mu k S \tag{2.40}$$

or alternatively:

$$\frac{\partial \varepsilon}{\partial t} + \boldsymbol{u} \cdot \nabla \varepsilon - \nabla \cdot (\frac{\nu_t}{\sigma_\varepsilon} \nabla \varepsilon) = \frac{\varepsilon}{k} (C_1' P_k - C_2 \varepsilon) \tag{2.41}$$

In the turbulence equations (39)-(41), the term P_k is the kinetic energy production due to shear stress and can be written as:

$$P_k = \nu_t S$$

whereas S in matrix form is:

$$S = \nabla^s \boldsymbol{u} : \nabla^s \boldsymbol{u}$$

with ∇^s denoting the symmetrical gradient operator. The coefficients of the $k - \epsilon$ modified model, following Panofsky and Dutton [10], are:

$$C_\mu = 0.0333, C_1 = 1.176, C_2 = 1.92, \sigma_k = 1.0, \sigma_\varepsilon = 1.238$$

whereas σ_ε is computed as:

$$\sigma_\varepsilon = \frac{\kappa^2}{C_\mu^{\frac{1}{2}}(C_2 - C_1)}$$

where $\kappa = 0.41$ is the Von Karman constant.
Taking σ_ε as a function of the other constants is necessary so that the logarithmic profile in the surface boundary layer can be correctly reproduced.
C_μ is a model constant usually calibrated in terms of the relation between friction and TKE (see Eq.(32)).

The coefficient C_1' in the RHS of the dissipation equation (41) is a modified coefficient, originally proposed by Apsley and Castro [9], to prevent the increase of mixing length, computed as:

$$l_m = C_\mu^{\frac{3}{4}} k^{\frac{3}{2}} / \varepsilon$$

above a maximum value l_{max} when accounting for Coriolis effects:

$$C_1' = C_1 + (C_2 - C_1)\frac{l_m}{l_{max}}$$

where l_{max}, i.e the maximum limited mixing length is calculated as:

$$l_{max} = 0.00027\frac{|\boldsymbol{u}_g|}{2|\boldsymbol{\omega}|\sin\lambda}$$

being $|\boldsymbol{u}_g|$ the modulus of the geostrophic wind velocity at the top of the domain and λ the latitude (set to 51.3 °). Note that, if no Coriolis forces are considered (i.e. $|\boldsymbol{\omega}| = 0$), then $l_{max} \to \infty$ and $C_1' = C_1$.

P_k instead is the production of TKE due to shear stress:

$$P_k = 2\nu_t \nabla^s \boldsymbol{u} : \nabla^s \boldsymbol{u}$$

where the symmetric gradient is given by:

$$\nabla^s \boldsymbol{u} = 0.5(\nabla \boldsymbol{u} + \nabla^T \boldsymbol{u})$$

2.3 Modifications to the basic models

2.3.1 Coriolis force

The Coriolis force is an inertial or fictitious force that acts on objects that are in motion within a reference frame that rotates with respect to an inertial frame [12]. In a reference frame with clockwise rotation, i.e in the southern hemisphere, Coriolis force always deflects to the left hand side of the streamwise direction whereas in one with counterclockwise rotation, i.e in the northern hemisphere, Coriolis force always deflects to the right hand side of the streamwise direction. Deflection of an object due to the Coriolis force is called the Coriolis effect. The Coriolis force is taken into account in the momentum equation and is expressed as:

$$\boldsymbol{f}_C = -2\boldsymbol{\omega} \times \boldsymbol{u} \tag{2.42}$$

where $\boldsymbol{u}$ is the velocity field and $\boldsymbol{\omega}$ the Earth's angular velocity.
Here below Image 2.1 shows the Coriolis force, the pressure gradient force and the resulting path identified respectively by the blue, red and black vector; in particular, the resulting one, provides information about the deflection of the Coriolis force.

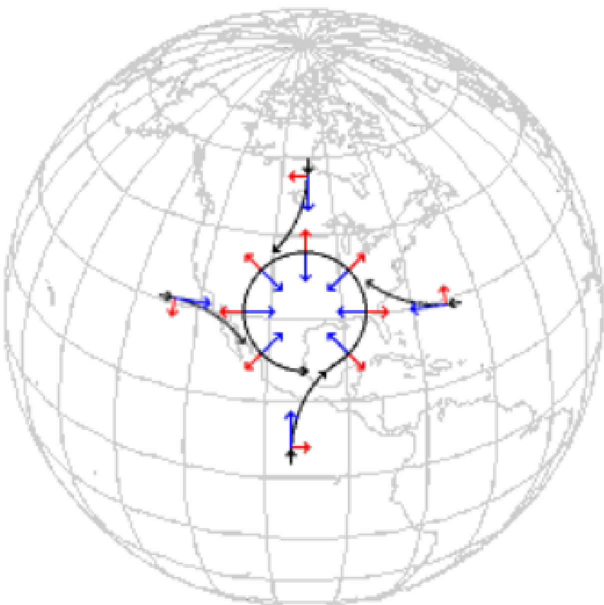

Figure 2.1: Coriolis force, pressure gradient force and resulting path

2.3.2 Forest effect

The presence of a forest (patchy in this case) alters the wind profile and influences energy production. Therefore taking into account the forest (or canopy) effect on the wind in the CFD model is fundamental and it allows to enhance the wind resource assessment.
The simplest approach to model the forest is to modify the surface friction and include a displacement height. This method can be used with both linear models or CFD simulations and it consists in generating a logarithmic profile that starts from the actual profile observed over the forest itself. A better alternative method, that can only be used in CFD models, is to consider the forest in the RANS equations, more specifically in the momentum one, and at the sime time both in turbulent kinetic energy and dissipation rate equations, as additional resistance terms induced by the porous region and thus they differ from conventional surfaces since the exchange may be distributed at several model levels.
Between all the possible canopy models, the Sogachev's one has been used in this work; in particular, it differs from the other canopy models because it does not introduce any modification to the equation for k and it supposes that the drag dissipation due to the forest equals the drag production due to the canopy.
The drag force generated by the canopy and insterted in the momentum equation, is indicated as $\boldsymbol{f}_{can}$ and is expressed as:

$$\boldsymbol{f}_{can} = -c_d LAD|\boldsymbol{u}|\boldsymbol{u} \tag{2.43}$$

where $c_d = 0.2$ is the drag coefficient used to simulate the forest, and LAD is the Leaf Area Density expressed in m^{-1}. In the turbulence equation instead, for ε, the additional term is represented by $C_3 c_d LAD|\boldsymbol{u}|k$. Contrary to other canopy models , Sogachev's one does not introduce any new constants since C_3 is defined as:

$$C_3 = (C_1 - C_2)12C_\mu^{1/2} \tag{2.44}$$

However, despite the relevant impact exerted by the canopy at the terrain surface and slighlty above that, the increasing in the WTs height has allowed WTs themselves to be positioned well above the forest, where influence of the canopy is reduced, but nevertheless present.

2.3.3 Atmospheric Boundary Layer

The Atmospheric Boundary Layer (ABL) corresponds to the lowest portion of the atmosphere where phenomena such as friction, turbulence and mixing are quite enhanced; furthermore these ones vary in time and space and so this region may experience a large diurnal variation in wind, (potential) temperature, and stability. The ABL is typically $0.5 - 1km$ deep, and it accounts for about the 10% of the total

mass of the atmosphere.
It also comprises a sub-region, the nearest one to the ground, named Atmospheric Surface Layer (ASL), where the wind flow (e.g wind speed and direction) is strongly affected by the topography and roughness (which cause friction); this layer, clearly, being inside the ABL is shorter than the ABL itself and is typically $50 - 150m$ deep.

The ABL can be also identified as that region in which the horizontal wind speed goes from zero along the surface of the Earth (cause of frictional forces) to the geostrophic value $\boldsymbol{U_g}$ in the free troposphere. Thus, geostrophic wind occurs at high height and is obtained by the balance between the Coriolis force, which is the centrifugal force applied on an air parcel arising from the rotation of the Earth, and the horizontal component of the pressure gradient.
The upper boundary can be determined by the altitude at which the wind vector is approximately equal to the geostrophic wind and it is usually characterized by a temperature inversion; in particular, if this one is strong, the mixing process with air from above gets stucked. In the ABL, clouds are missing, but haze or mist could be present.

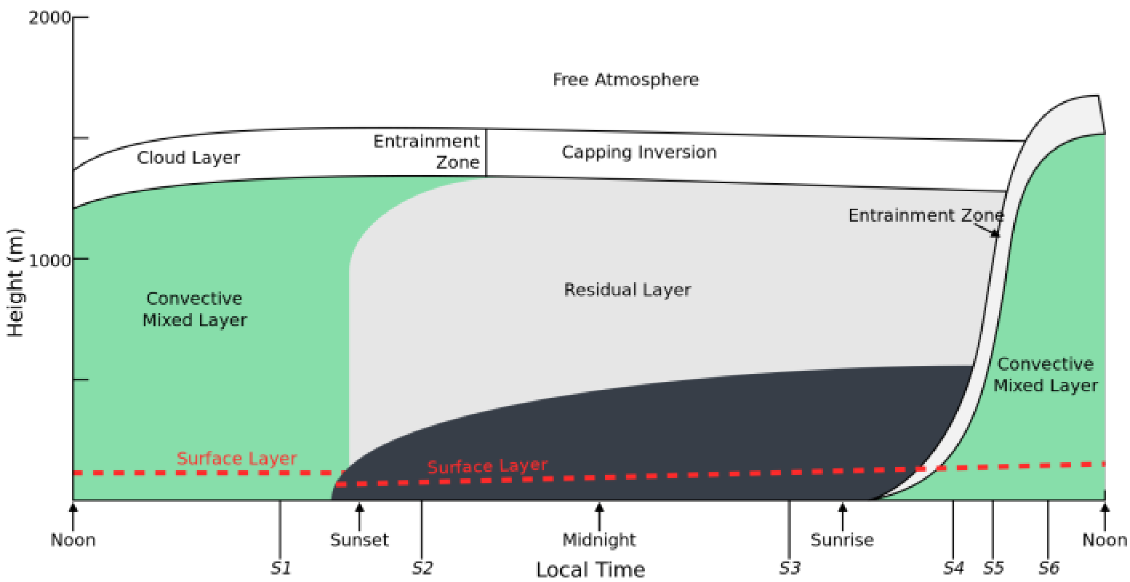

Figure 2.2: Structure of the Atmospheric Boundary Layer over one diurnal cycle

The high turbulence level in this layer, especially in the ASL, is due to heating of the ground, and adiabatic or even stronger (super-adiabatic) temperature gradients resulting from radiative processes involving the ground itself. Besides, wind shear as well, exerts a strong impact on that, which is even more pronounced when the terrain is forested.
For these reasons, two important parameters, that have to be considered when assessing the stability of the ABL, are the potential temperature and wind velocity, which change in time and with height. In particular three possible real scenarios may occur:

$\partial\theta/\partial z = 0$ for neutral stability condition,

$\partial\theta/\partial z > 0$ for stable condition (at night),

$\partial\theta/\partial z < 0$ for unstable condition (during daytime),

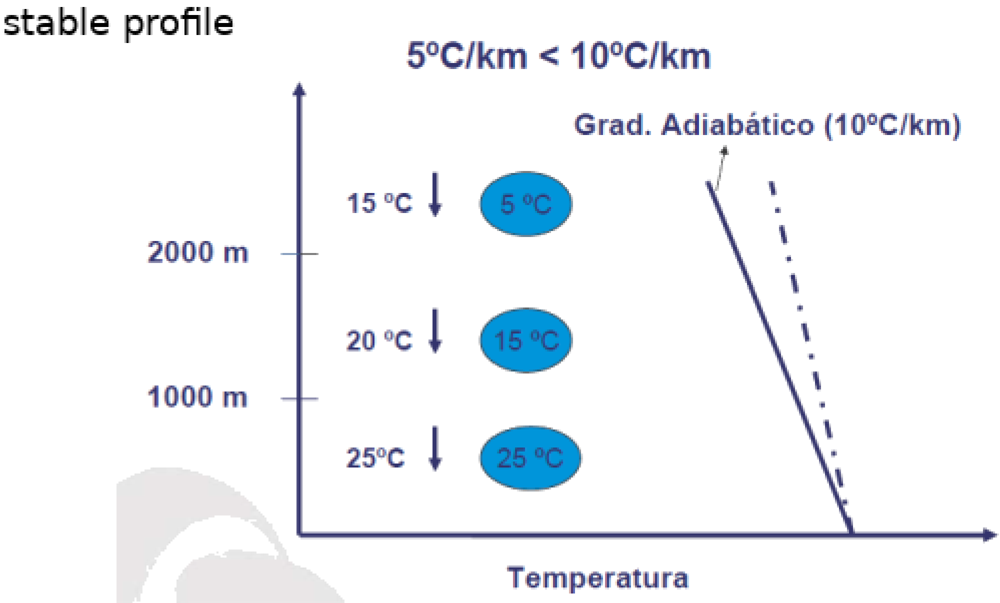

Figure 2.3: Atmospheric stability: stable temperature gradient

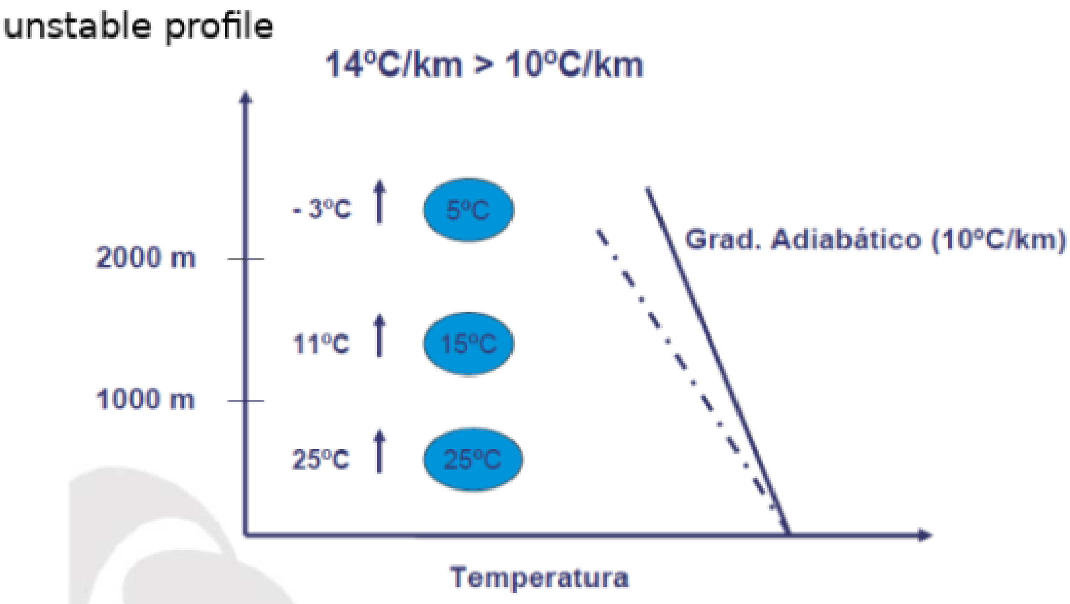

Figure 2.4: Atmospheric stability: unstable temperature gradient

For a neutral condition instead the temperature gradient will be vertical.

Figure 2.5 instead shows the wind velocity profiles for stable (blue line), neutral (green line) and unstable (red line) condition.

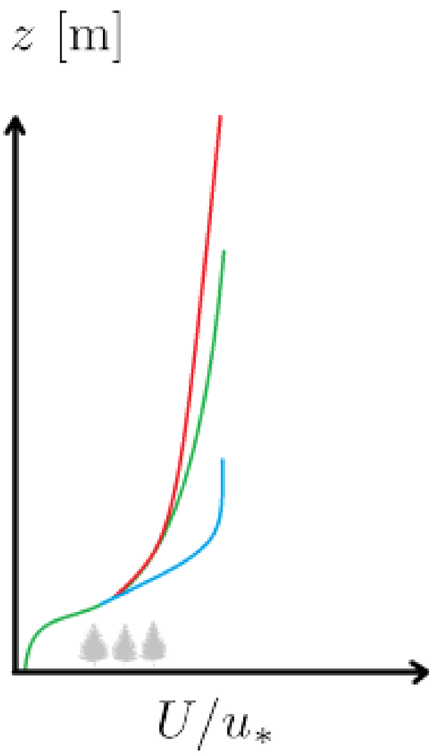

Figure 2.5: Atmospheric stability: stable, neutral and unstable profile of wind velocity

Between all these three possible conditions occuring during the day, most of the time the neutral one represents an average situation; this is the reason for which, instead of dealing with both stable and unstable ABL conditions at different times, simulating a neutral ABL condition results to be a fairly good approximation.
For neutral ABLs, Zilitinkevich and Esau [13] suggest to make a distinction between truly neutral flows, developing in a neutrally stratified fluid, and conventionally neutral flows, developing against a stable stratification. Hess [14] has concluded that the truly neutral ABL is an idealised case that "does not seem to exist in the atmosphere, or is so rare that it has not been well observed".
On top of that, since in the present study, data provided by Fraunhofer IWES come from a measurement campaign (real data), between those two neutral conditions, this work considers the second one, i.e a conventionally neutral atmospheric boundary layer (CNBL).
In this context, a fundamental parameter to define the ABL stratification is the Obukhov length L; this one is a parameter with dimension of length that is used to scale the height above the ground, yielding to a dimensionless stability parameter, $(z-d)/L$, that expresses the relative impacts of shear and buoyancy in the production/consumption of TKE.
It is defined by:

$$L = -\frac{u_*^3 T}{\kappa g \overline{w'\theta'}} \tag{2.45}$$

where z is the height, d is the displacement height, κ is the Von Karman constant, u_* is the friction velocity (a measure of surface stress), $\overline{w'\theta'}$ is a kinematic virtual temperature flux at the surface, T is a reference virtual temperature, and g is the gravitational acceleration. The ratio g/T defines the buoyancy parameter, with Tv which often refers to the surface air temperature, consistent with the Boussinesq approximation.
The Obukhov length, is typically of order one to tens of meters, and it comes out to be positive (negative) for stable (unstable) stratification, tending to infinite for a neutral stratification ($\overline{w'\theta'} = 0$). The dimensionless Obukhov stability parameter $(z - d)/L$, typically ranges from –5 to 5, with positive (negative) values indicating stable (unstable) values, and tending to 0 in a neutral stratification; the last one condition, is exactly what verifies in the present work, where $L = 4000m$ at $z = 60m$, and so the ratio tends to 0.

2.3.4 WTs effect: actuator disk theory

When WTs are insterted into the domain, clearly, the airflow modifies as it passes through them. In fact, the extraction of wind kinetic energy across a WT generates an aerodynamic wake region downstream of the rotor. The wake region is generally associated with a few key characteristics such as a pressure differential, increased turbulence (caused by rotation of the wake field, disruption of the air flow across the rotor blades and vortices at the blade tips) and an expanding wake area downstream of the WT in conjunction with a velocity deficit.

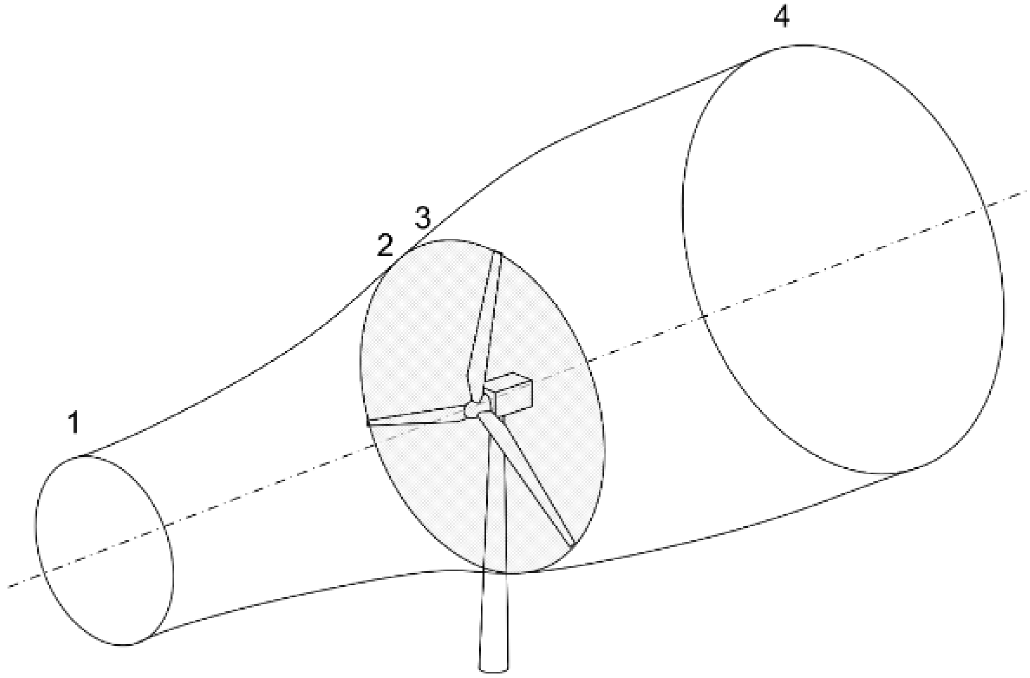

Figure 2.6: Inlet, rotor and outlet cross section [15]

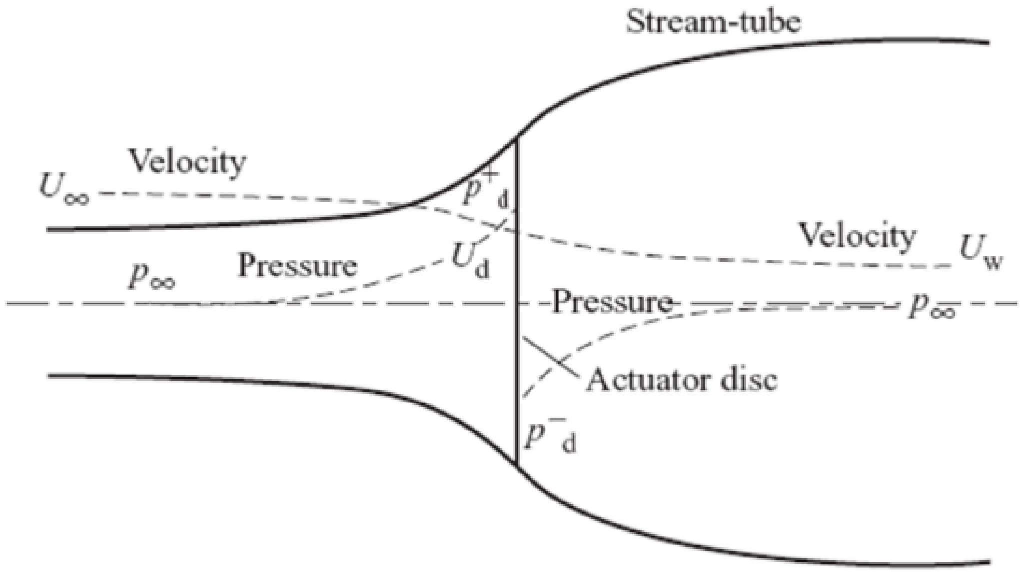

Figure 2.7: Pressure and velocity airflow evolution through the WT [15]

Figure 2.7, provides the shape of the velocity and pressure curves as the wind gets through the turbine. The WT insertion, introduces a gap of pressure through the disk, whereas the velocity is continuous. As it can be seen, a high pressure area forms upstream of the rotor and a lower one downstream. This pressure change is due to the work of the rotor blades on the air passing over them. The force applied by the air on the blades results in an opposite force exerted on the air stream, which in turn causes a rotation of the air column. This low pressure column of rotating air expands as it moves downstream of the WT and finally dissipates as equilibrium

is achieved with the surrounding airflow [15].
WTs are modeled as actuator discs and treated as a sink of momentum by imposing a uniform force term, which is exerted by each WT (disc) over the flow, and that can be expressed as:

$$F = \frac{1}{2}\rho C_t(U_\infty)U_\infty^2 A \tag{2.46}$$

$$C_t = 4a(1-a)$$

whereas, the wind power is written as:

$$P = \frac{1}{2}\rho C_p(U_\infty)U_\infty^3 A \tag{2.47}$$

$$C_P = 4a(1-a)^2$$

In the momentum equation instead, the specific force is considered:

$$\boldsymbol{f} = \frac{1}{2}\frac{C_t}{\Delta}U_\infty^2 \boldsymbol{n}_d \tag{2.48}$$

where the thrust coefficient C_t and the power coefficient C_p are provided by manufacturers as thrust and power coefficient curve depending on the undisturbed wind velocity $C_{tm}(U_\infty)$ (see Section 5.1), A is the rotor swept area and Δ is the thickness of the disc.
For this specific task (actuator disc modeling), Alya uses a robust nonlinear method to calculate the thrust coefficient and free stream velocity for each wind turbine. The main issue is related to the complexity in estimating the free stream velocity U_∞ (and therefore C_t) because the wind turbine power and thrust curves are usually provided for single-machine operation rather than operation involving wakes generated from other WTs.
For this reason, the approach consists in relating the free stream velocity U_∞ to the velocity at hub height U_{hub} in terms of the thrust coefficient using 1-D momentum theory; unfortunately, for high thrust coefficients, this theory is no longer valid and an empirical relationship is used to obtain the theoretical thrust coefficient C_{ta}:

$$C_{ta}(a) = \begin{cases} 4a(1-a) & a < 0.4 \\ 0.889 - (0.0203 - (a-0.143)^2)/0.6427 & a \geq 0.4 \end{cases} \tag{2.49}$$

$$a = 1 - \frac{U_{hub}}{U_\infty} \tag{2.50}$$

where a is the axial induction factor. The velocity at hub height U_{hub} is computed as the wind velocity component perpendicular to the disc surface averaged over the entire disc volume. To compute the proper value of U_{hub} (and C_t), Alya performs an iterative procedure. Given an initial guess for U_∞, firstly C_{tm} (U_∞) is computed; secondly, the induction factor a is updated in terms of $C_{ta} = C_{tm}(U_\infty)$ by using the inverse of Eq.(48) (the first one) and, finally, a new U_∞ is calculated in terms of a, by using the inverse of Eq.(48) (the second one) until U_∞ converges to a fixed value; this is done by verifying that $C_{tm} = C_{ta}$.
Introducing Eq.(50) in (49), the iterative problem can be re-written in terms of U_∞ and it requires to solve the following non-linear equation:

$$f(U_\infty) = C_{tm}(U_\infty) - C_{ta}(1 - \frac{U_{hub}}{U_\infty}) = 0 \tag{2.51}$$

To solve Eq.(51) Alya uses the bisection method, which takes advantage of the fact that the equation is one-dimensional; in this way it allows avoiding to compute the derivatives of the target function f.

2.4 Resulting model

Considering the flow as incompressible and isothermal (neutral stability) and applying all the corrections discussed so far, the modified $k-\varepsilon$ RANS resulting model is written as:

$$\nabla \cdot \boldsymbol{u} = 0 \tag{2.52}$$

$$\frac{\partial \boldsymbol{u}}{\partial t} + \boldsymbol{u} \cdot \nabla \boldsymbol{u} - \nabla \cdot (\nu_t \nabla^s \boldsymbol{u}) + \nabla(\frac{p}{\rho}) + \frac{1}{2}\frac{C_t}{\Delta} U_\infty^2 \boldsymbol{n}_d = -2\boldsymbol{\omega} \times \boldsymbol{u} - c_d LAD|\boldsymbol{u}|\boldsymbol{u} \tag{2.53}$$

$$\frac{\partial k}{\partial t} + \boldsymbol{u} \cdot \nabla k - \nabla \cdot (\frac{\nu_t}{\sigma_k} \nabla k) = P_k - \varepsilon \tag{2.54}$$

$$\frac{\partial \varepsilon}{\partial t} + \boldsymbol{u} \cdot \nabla \varepsilon - \nabla \cdot (\frac{\nu_t}{\sigma_\varepsilon} \nabla \varepsilon) = \frac{\varepsilon}{k}(C_1 P_k - C_2 \varepsilon + C_3 c_d LAD |\boldsymbol{u}| k) \tag{2.55}$$

$$\nu_t = C_\mu \frac{k^2}{\varepsilon} \tag{2.56}$$

where the unknowns are the velocity field $\boldsymbol{u}$, pressure p, turbulent kinetic energy k, dissipation rate of turbulent kinetic energy ε, and turbulent viscosity ν_t computed by means of Eq.(56).
The first term on the right hand side of momentum equation (53) models the Coriolis force, being $\boldsymbol{\omega}$ the Earth's angular velocity. The fifth term on the left hand side of equation (53) is the actuator disc force, which is active only inside the disc volume, where C_t is the thrust coefficient, U_∞ is the free-stream velocity at hub height, $\boldsymbol{n}_d$ the disc normal unit vector (pointing opposite to inflow), and Δ is the thickness of the disc. The forces inside each disc volume are uniformly distributed.

2.4.1 Boundary conditions

In order to perform correctly the simulation, proper boundary conditions need to be applied to the Navier Stokes (52)-(53) and turbulence $k-\epsilon$ (53)-(54) equations. The whole computational domain is subdivided into four boundaries, i.e inflow, outflow, bottom and top.
Lateral boundary are automatically set as either inflows or outflows based on the angle they form with respect to a 1-D wind profile obtained by solving the previous set of equation over flat terrain with a fixed surface roughness and a specified geostrophic wind velocity and direction.
A boundary is defined as an inflow if its outwards pointing normal forms an angle greater then 85° with respect to the one dimensional wind profile and as an outflow otherwise.

- The bottom boundary, corresponds to the ground and at this surface a wall law satisfying the Monin-Obukhov equilibrium is imposed to both momentum and turbulence equations removing a boundary layer of thickness δ_w. The imposed shear stress $\boldsymbol{\tau}_w$ is tangent to the wall and is evaluated in terms of two velocity scales, defined as u_{*u} and u_{*k}, and related respectively to the tangent velocity and the turbulent kinetic energy:

$$\boldsymbol{\tau}_w = -u_{*v} u_{*k} \frac{\boldsymbol{u}(z = \delta_w)}{|\boldsymbol{u}|(z = \delta_w)} \tag{2.57}$$

The negative sign is because its direction is opposed to the velocity.

$$u_{*u} = \kappa \frac{|\boldsymbol{u}|(z = \delta_w)}{ln(1 + \frac{\delta_w}{z_0})} \tag{2.58}$$

$$u_{*k} = C_\mu^{\frac{1}{4}} k^{\frac{1}{2}} \tag{2.59}$$

where $\boldsymbol{u}$ is the component of the velocity tangent to the wall and $|\boldsymbol{u}|$ identifies its norm. The friction velocity u_{*u} is obtained from the neutral atmospheric velocity profile at a distance δ_w from the wall (set to 1 m), being κ the Von Karman constant and z_0 the roughness (length) of the terrain.
For the turbulent kinetic energy instead, zero diffusion through the wall is imposed:

$$\nabla k \cdot \boldsymbol{n} = 0$$

whereas ε is computed as:

$$\varepsilon = \frac{u_{*k}^3}{\kappa(\delta_w + z_0)} = \frac{C_\mu^{\frac{3}{4}} k^{\frac{3}{2}}}{\kappa(\delta_w + z_0)} \tag{2.60}$$

The velocity $\boldsymbol{u}(z = \delta_w)$ in the previous equation represents the unknown vector being solved from set of Eq (52)-(56); thus on the ground, the boundary condition applied for the velocity is the following:

$$\boldsymbol{u} \cdot \boldsymbol{n} = 0, \quad \boldsymbol{n} \cdot \sigma \cdot \boldsymbol{g}_1 = \tau_w \cdot \boldsymbol{g}_1, \quad \boldsymbol{n} \cdot \sigma \cdot \boldsymbol{g}_2 = \tau_w \cdot \boldsymbol{g}_2 \tag{2.61}$$

where σ is the Cauchy stress tensor, $\boldsymbol{n}$ is the vector normal to the boundary and $\boldsymbol{g}_1$ and $\boldsymbol{g}_2$ are two vectors that span the space tangent to the boundary.

- The top boundary (or top domain) is managed by imposing symmetry boundary conditions for tangential velocity and turbulence unknowns:

$$\frac{\partial \boldsymbol{u}}{\partial n} = 0$$

$$\frac{\partial k}{\partial n} = 0$$

$$\frac{\partial \varepsilon}{\partial n} = 0$$

The normal velocity component is fixed to zero (i.e. $\boldsymbol{u} \cdot \boldsymbol{n} = 0$) and pressure is set to geostrophic value.

- On the inflow boundary, the procedure consists in generating, from a single-column (1D) precursor simulation (i.e. flat terrain and uniform roughness) a vertical profiles which are subsequently imposed for inflow velocity $\boldsymbol{u}$ and turbulence unknowns k and ε.

- On the outflow boundary geostrophic pressure and no shear stress are imposed for the momentum equation and symmetric boundary conditions (no gradient) are imposed for the turbulence unknowns (for the turbulence equations).

2.4.2 Iterative procedure

The RANS and $k - \varepsilon$ model equations, are discretized using a stabilized finite element method which is based on equal interpolation for all the unknowns. Instead, for what concerns the stabilization scheme, the Algebraical Subgrid Scale method (ASGS) extended for nonlinear equations, has been used in Alya, which provides stability to convection and Coriolis dominating terms in the momentum equation and to convection and reactive terms in the turbulence equations, removing spurious oscillations.
The ASGS stabilization method allows also to stabilize pressure, enabling equal interpolation spaces for pressure and velocity. The velocity-pressure problem is decoupled using an Orthomin solver that converges to the monolithic scheme. A robust finite element scheme written in block-triangular form is obtained for the $k-\varepsilon$ equations (54)-(55).
Despite the diffusion and reaction coefficients in $k-\varepsilon$ equations are positive, the numerical scheme is not always able to ensure positiveness and so when sign variations occur in the reactive terms, they lead to loss of stability. For this reason, in order to avoid instabilities and numerical convergence issues, ε and k are not allowed to drop below a predefined limit.
In addition, the innermost iterative loops of the k and ε equations (54)-(55) are

linearized using a Newton-Raphson scheme for the quadratic terms, considering ν_t and P_k constants within the innermost loops.
Once the algebraical set of equations is defined , a Deflated Conjugate Gradient solver with a linelet pre-conditioner [27] is used to solve the pressure, and a Generalized Minimizing Residual (GMRES) solver is used for the velocity and turbulence unknowns, resulting in un-symmetric problems.

Chapter 3

Surface and volume mesh generation

The first stage of wind farm numerical modelling consists in the mesh generation. Typically, the computational domains involved are large (scale of kilometers) and, at the same time, the local wind dynamics have to be captured precisely over the terrain and around turbines (scale of meters); such a combination of large domains and small spatial scales, generally indicated as multi-scales computational domains, and the need to increase the extent and/or the resolution of the simulations, can result in quite complex space discretizations leading to a high number of computational cells (elements/nodes) and, consequently, to large computational solver requirements; to accomplish this task, the present work takes advantage of one of the most powerful supercomputers present in Europe, at the BSC-CNS, the MareNostrum IV.
Ideally, meshes should preserve topographic features, resolve the terrain ABL and, at the same time, if WTs are inserted, capture the relevant wake scales. More specifically, the meshes generated in this work, are tailored to simulate a neutral ABL flow on Rödeser Berg hill and the WTs are modeled as actuator discs.
The whole mesh generation process consists of three main steps: first, it is necessary to discretize the underlying topography by generating a semi-structured surface mesh without WTs (see Section 3.1); second, in order to capture and resolve the ABL flow, an ABL volume (structured) mesh is required; this mesh, made up of hexahedral elements, is generated from the surface one by means of an extruding procedure combined with a quality optimization (see Section 3.2); third, if WTs are considered, the mesh around them is removed and the actuator discs, used to emulate their effects, are embedded in the ABL volume mesh and discretized using hexahedra.
Eventually, in order to capture the effects of WTs, that cause wind speed deficit, an increase of turbulent kinetic energy and interactions among wakes, the final mesh requires a higher resolution radially, upstream and downstream of WTs; thus the ABL volume mesh and discs are coupled by resorting to a finer unstructured tetrahedral mesh and using different tetrahedral/pyramid templates to generate a conformal hex-dominant hybrid mesh; this is done in order to provide smooth element size transitions across scales so as to avoid extending the higher resolution zones around the discs all over the domain (see Section 5.1).
All these meshing steps, clearly, affect the simulation accuracy and computational requirements of the solver since they impact the mesh quality and increase the num-

ber of elements/nodes of the mesh.
The wind farm mesher, developed by A. Gargallo-Peiró et al.[6] at BSC-CNS, and implemented in Alya as an external model-independent pre-process program, is fully automatic and it needs only some input data such as topography, roughness, wind inflow direction and WT characteristics. Then, resulting meshes will be used to solve the RANS equations with a $k-\epsilon$ turbulence model adapted to a neutral ABL.

3.1 Topography surface mesh

The generation of the topography surface mesh, that defines the boundary of the volume one, is performed through the following four steps:

1. Setting the topography geometry.
   The underlying topography can be provided to Alya in many formats, such as netCDF, CSV or point clouds, i.e XYZ. Then the mesher unifies all the input frameworks by converting them into a triangle mesh, that is used as a geometry representation. In addition, since data are real, topography as well as roughness can be perturbed by noise that can be either originally in the topography/roughness or generated during the extraction procedure.
   Therefore, if necessary, this meshing procedure allows to remove this noise by performing a signal process smoothing. In the present case, this operation has been performed for both, because the terrain data provided by the Fraunhofer IWES were real (not filtered). Following, it defines a parameterization of the target surface, i.e the topography, that maps a point (node) in the parametric plane to a point in the topography. In this case, it is a discrete parameterization that finds the surface triangle to which the point belongs, and computes the exact location of this point in the topography[6].

Figure 3.1: Meshing process: topography, top view

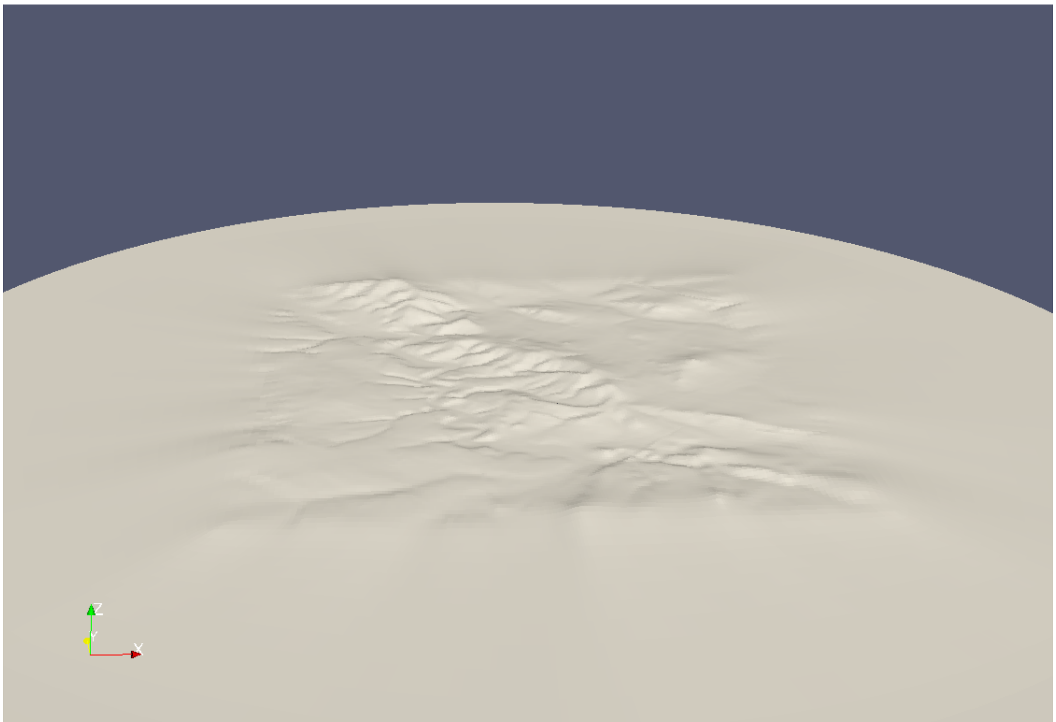

Figure 3.2: Meshing process: topography, front zoom

2. Generating a planar semi-structured quadrilateral mesh.
   The mesher generates an initial planar semi-structured quadrilateral mesh (2D). In particular, it works so as to set three different zones with three different levels of resolution (see figure 3.3). The centrall area, i.e the wind farm one, is the most relevant because it is the region in which WTs will be placed, and for this reason it is characterized by a higher resolution (w.r.t to the other two). Then there are the transition area, which surrounds the farm and has elements of increasing size outwards, and the elliptical buffer area, i.e the external one, which is characterized by a lower resolution (coarse mesh) and is used to impose the inflow/outflow boundary conditions. Among them, only the transition and wind farm zones contain real topography and roughness data whereas, in contrast, the buffer zone is set to be flat in order to guarantee consistence with the inflow profiles.

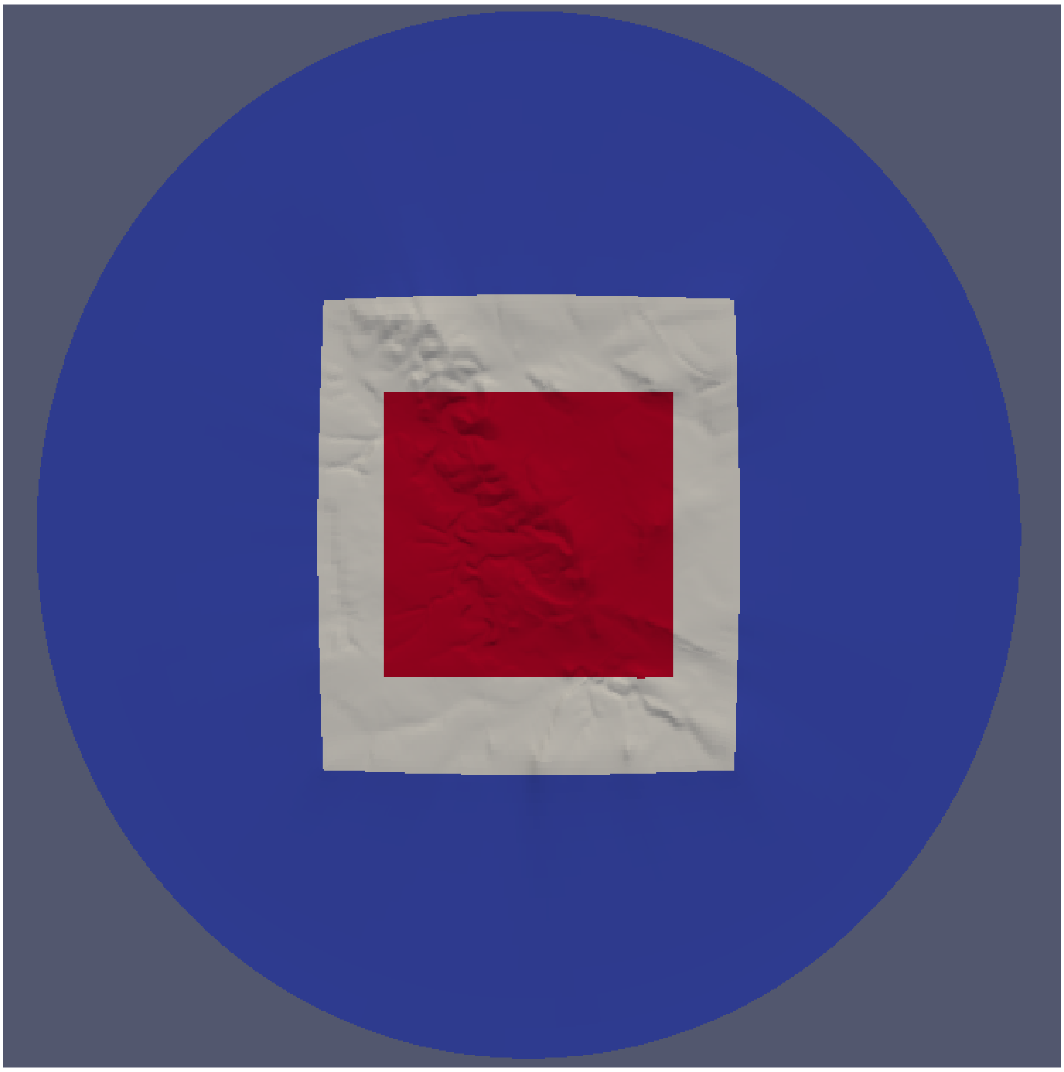

Figure 3.3: Meshing process: domain regions

The mesh size at the farm and buffer areas are the two user input parameters that determine the surface mesh size. In this work, many mesh sizes at the farm have been tested, such as 20, 30, 40 and 60 m, while at the buffer it has

been kept fixed to 100 m.
Firstly, the mesh of the farm area is created by generating a structured quadrilateral mesh on the plane aligned to the input direction (217°). This process results in a quadrilateral domain composed by quadrilateral elements of the size imposed to discretize the desired topography features (20,30,40 or 60 m). Secondly, since the resolution of the farm and buffer areas may be different, the mesher generates a transition area that smoothly matches the element size of the farm and buffer area.
Finally, to make the imposition of boundary conditions simpler, the quadrilateral domain in the buffer zone is transformed so as to make it slightly rounded; this is done in order to avoid the discontinuities that the corners of the structured mesh can induce and to impose in a continuous manner the input/output flow conditions. In this way, a semi-structured quadrilateral planar mesh is obtained.

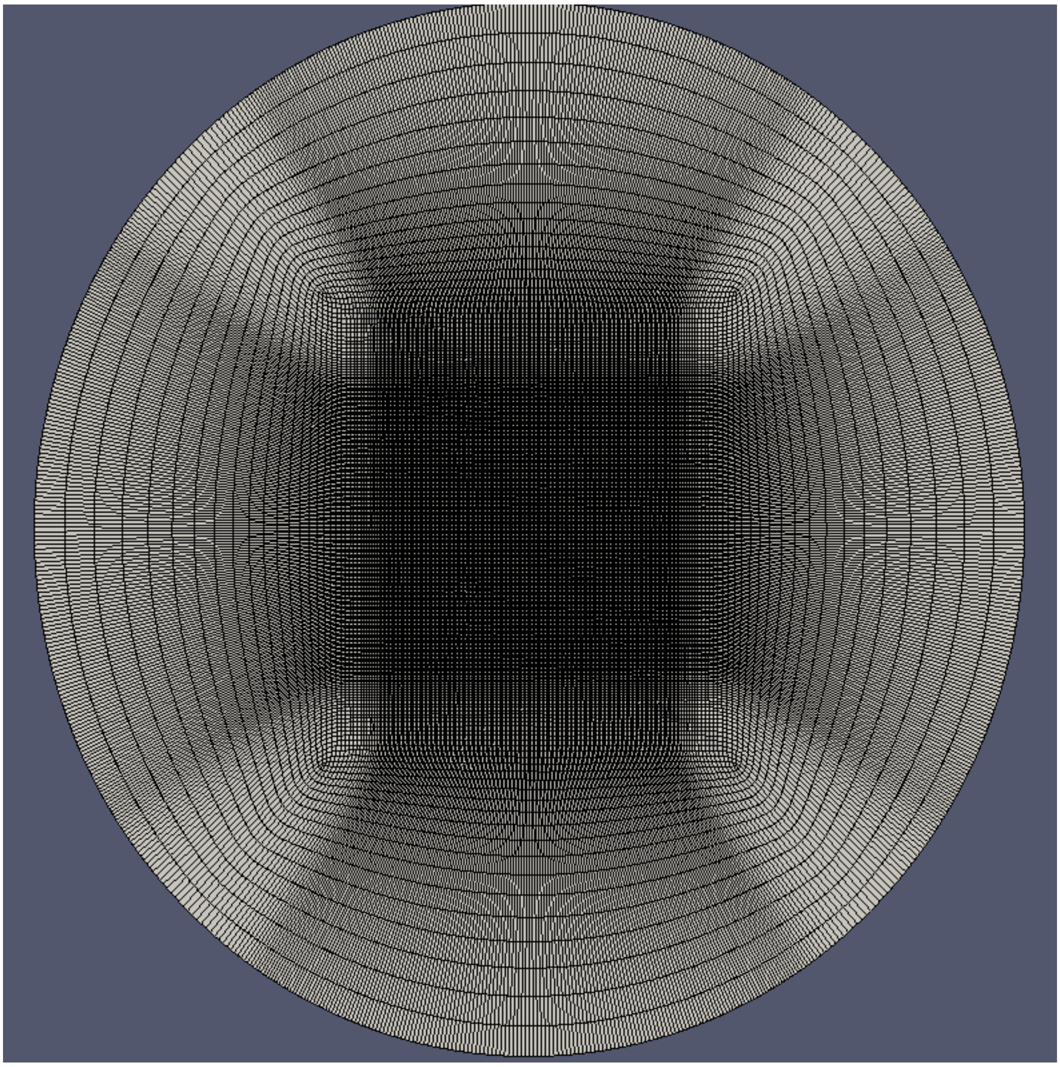

Figure 3.4: Meshing process: quadrilateral surface mesh, top view

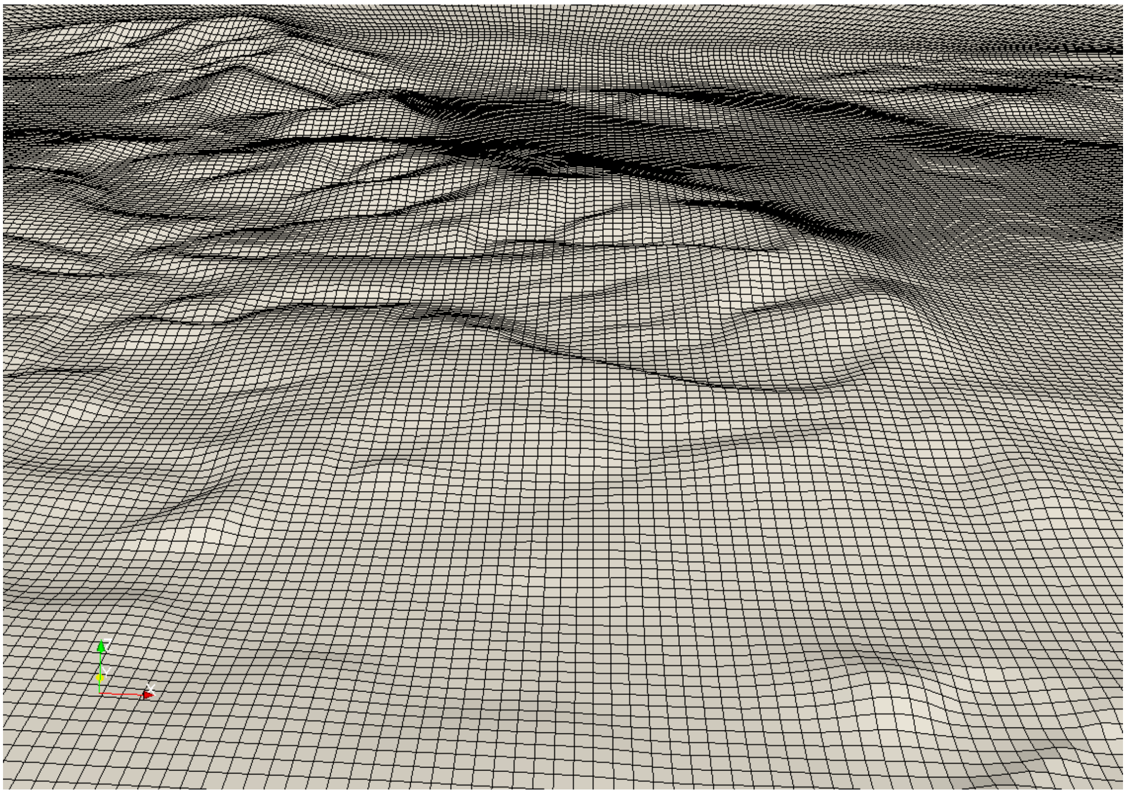

Figure 3.5: Meshing process: quadrilateral surface mesh, zoom on the hill

3. Generating an initial topography surface mesh.
   The following step after getting a planar configuration consists of mapping the nodes to the exact topography by means of the surface parameterization, obtaining a surface mesh.
   It is worthwhile to highlight that in the resulting surface mesh, distorted elements can be present. This may be caused by the fact that quadrilaterals, that were square in the plane, can be mapped to almost invalid configurations in areas of the topography where there are high terrain gradients[6]. Therefore, it is compulsory to check the validity of the elements and to quantify how much it varies w.r.t the desired configuration.
   To measure if an element is valid, and to quantify how much it differs from the desired configuration, the distortion measure is used; it quantifies in the range $[\,1, \infty)$ the deviation of an element w.r.t to an ideal configuration.
   In alternative, the validity of an element can be expressed in term of quality, which is the inverse of the distortion. and provides a value in $[0, 1]$, being 0 an invalid configuration, and 1 the desired one[6].

4. Surface mesh optimization.
   The last step of the generation process of the surface mesh consists of the optimization of the location of the mesh nodes on the exact topography to

obtain a final mesh which minimizes the elemental distortion (so maximizing the quality). For each element of the surface, the mesher defines its ideal correspondent, which is an orthogonal quadrilateral of the desired size. At this point, the target of the procedure is to make sure that each surface element reassembles its ideal as precisely as possible, taking into account that a surface element has its nodes constrained to the topography[6].

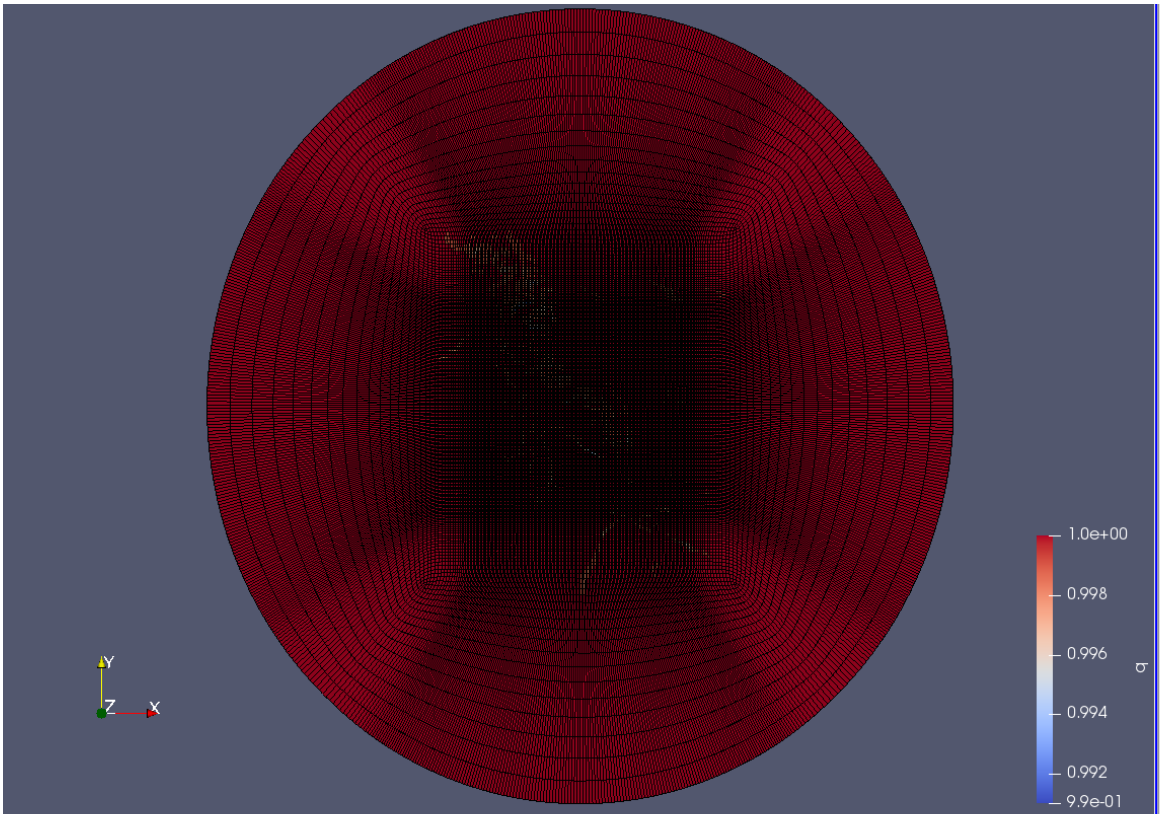

Figure 3.6: Topography mesh generation: optimized surface mesh, top view

Figures 3.6 and 3.7 display the optimized semi-structured quadrilateral surface mesh and at the bottom-right, q is indicating the quality of the quadrilateral surface elements; these two images, as well as figures 3.4 and 3.5 are referring to one only mesh cell size, which is equal, in this case, to 30 m (30m x 30m).
As previously described, other mesh cell sizes have been tested (20,40 and 60 m) but clearly, being the number of nodes and elements of the mesh itself quite high in all the cases, it would be impossible to notice, from graphical representations only, the slight differences between the various tested cases; this is the reason why one only mesh is shown; it is meant just for visual demonstration.

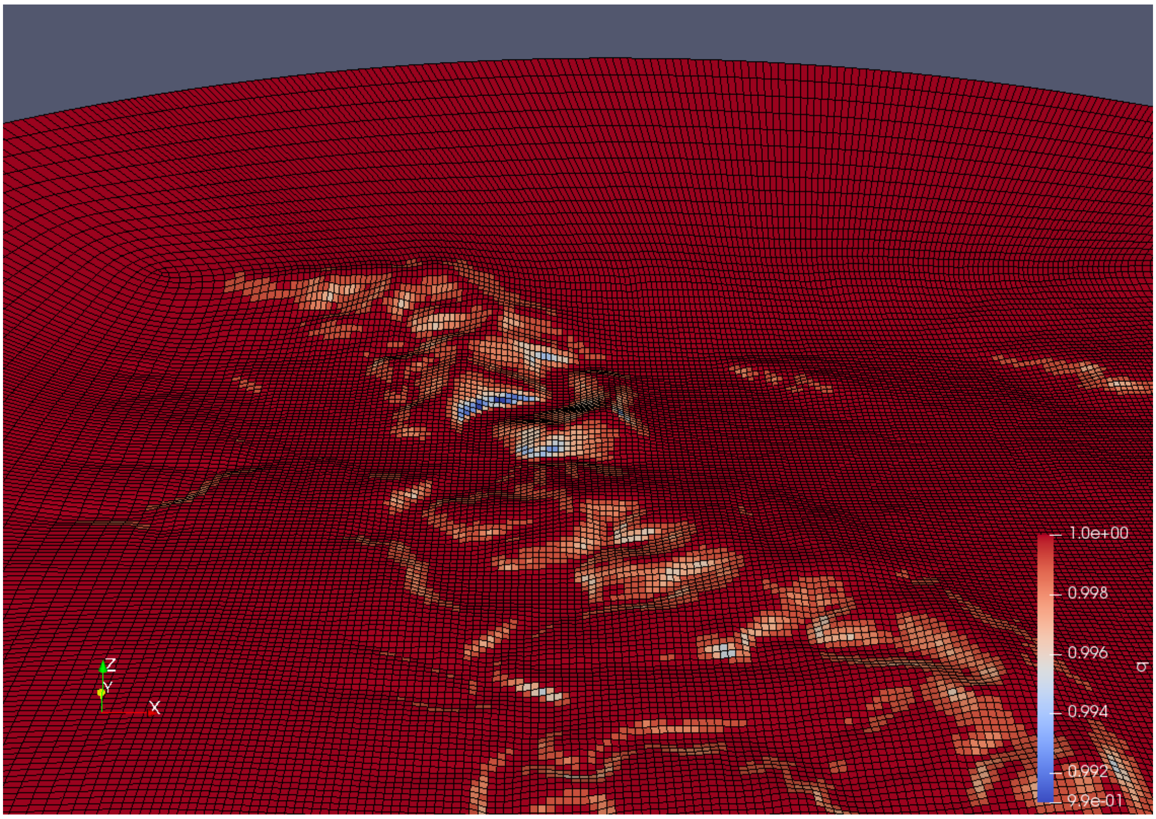

Figure 3.7: Topography mesh generation: optimized surface mesh, zoom on the hill

Another important aspect to specify is that, since the mesh quality strongly affects the volume mesh and in turn the results of the numerical simulation, the surface mesh optimization, set as optional in the input file, actually comes to be a compulsory choice for improving results; in fact, this optimization procedure (developed by Owen at BSC-CNS in Alya) allows to almost double the mesh quality.

3.2 ABL volume mesh

The semi-structured ABL volume mesh is generated by extruding, along the vertical direction, the quadrilateral topography surface mesh (optimized) into layers and when it comes to generate a wind farm mesh, it is fundamental, because it represents the starting point to generate a mesh adapted to the WTs, simulated as discs (see Chapter 5, Power generation). Herein, the input file requires to insert the growth factor (or growing ratio) of the boundary layer, in a range that varies between 1.05 and 1.25, so as to have higher vertical resolution near the ground; in this case 1.15 has been choosen. Then, an anisotropy in the first layer of the order of 1/100 or 1/1000 is set, depending on the case and the region of the domain. The (iterative) extruding procedure, to compute each new sweeping layer, consists of two main steps:

1. Compute new layer maximizing projected area.
   Given the previous layer, it generates a new one of hexahedra by sweeping

each node using an extruding length and an extruding direction. The current extrusion length is calculated in a standard manner using a geometrical law of the desired growing ratio, instead for what concerns the extruding direction, the pseudo-normal of the nodes adjacent to each node is used to compute a new direction that maximizes the orthogonality of the new generated layer. Furthermore, the mesher blends the pseudo-normal with the vertical direction in order to enforce the mesh growing towards the ceiling, set by default to 2 km (above the highest terrain elevation), and to get to the top orthogonally to the planar ceiling. Also in this case, as for the surface mesh, to perform an optimization of the final mesh, the mesher sets an ideal element for each generated physical element, that is, in this case, an hexahedron[6].

2. Optimize the new layer to improve the mesh quality.
   Once the mesher generates a new layer, it optimizes that w.r.t the corresponding ideal elements set before; and although the meshing program sweeps them using the best projection plane, the constraint of being generated from a topography mesh prevents the mesh from being optimal; In fact, in certain zones characterized by high topographic gradients, this projection can result on low quality elements.
   Therefore, before generating a new layer of elements, it optimizes the current one. More in detail, it does not optimize all the previously generated elements but just the new low-quality ones generated in the new layer.
   Once the sweeping process is concluded, the mesh has been optimized only locally to guarantee that the previous extruded layers where defining a valid configuration for the new layer being generated. Therefore, the mesh is not globally optimized yet; thus, after the topology of the final mesh has been set, a final mesh optimization is performed.

Figure 3.8 shows the ABL volume mesh and the generated layers, that in the present case are 49. This mesh, when WTs are not considered, is the final one, and it will be provided to the Alya solver (based on finite elements method) to solve the RANS equations with $k - \epsilon$ turbulence model. Clearly, the choice to optimize the mesh, as well as to reduce mesh cell sizes, lead, on one hand, to get more precise numerical results but one the other hand to an higher number of solver iterations and time step iterations to achieve a stationary solution; so it is always necessary to find a compromise between them.
Figure 3.9, instead, provides a view inside the domain; the layers, here represented for clarity reasons only along the lateral boundary, extend through the whole domain (volume), i.e all over the surface mesh.
Figure 3.10 depicts the quality of the hexahedral elements, belonging to the layers and extending along the height of the domain; it is indicated as qex, at the bottom right.

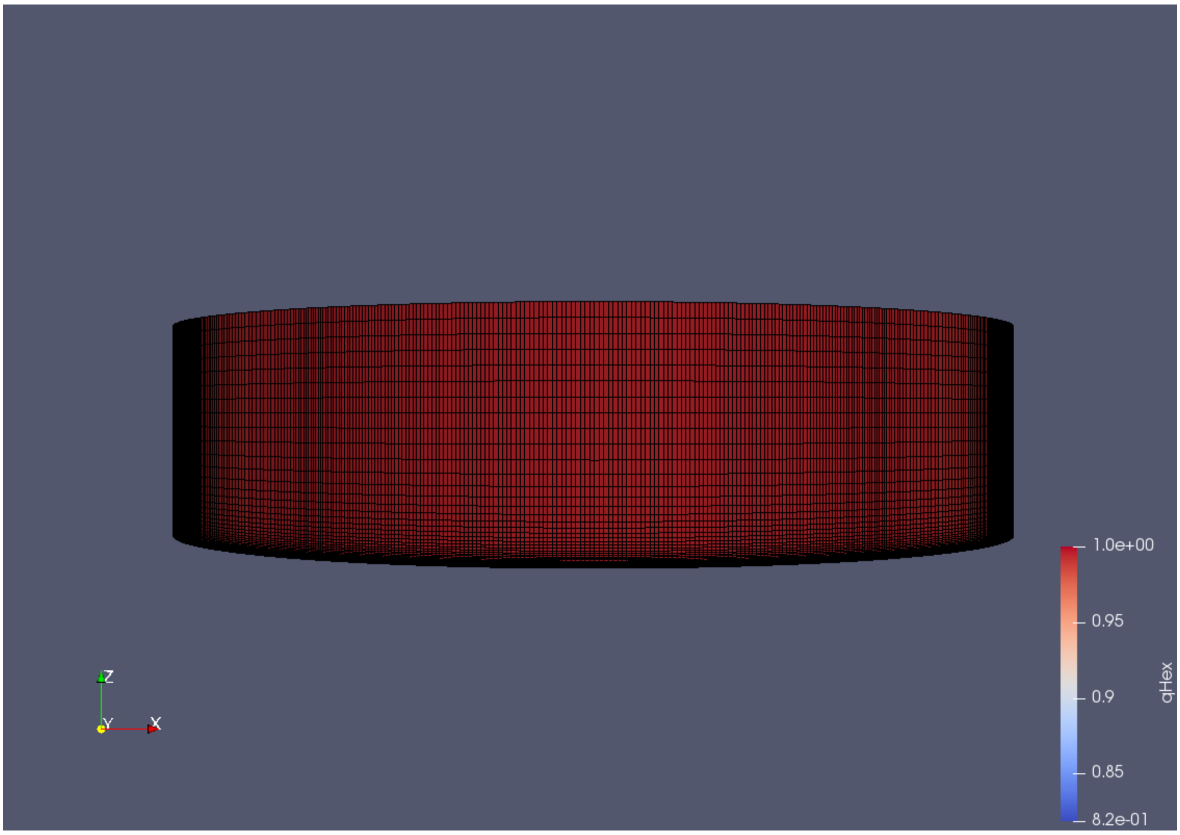

Figure 3.8: ABL mesh generation: side view

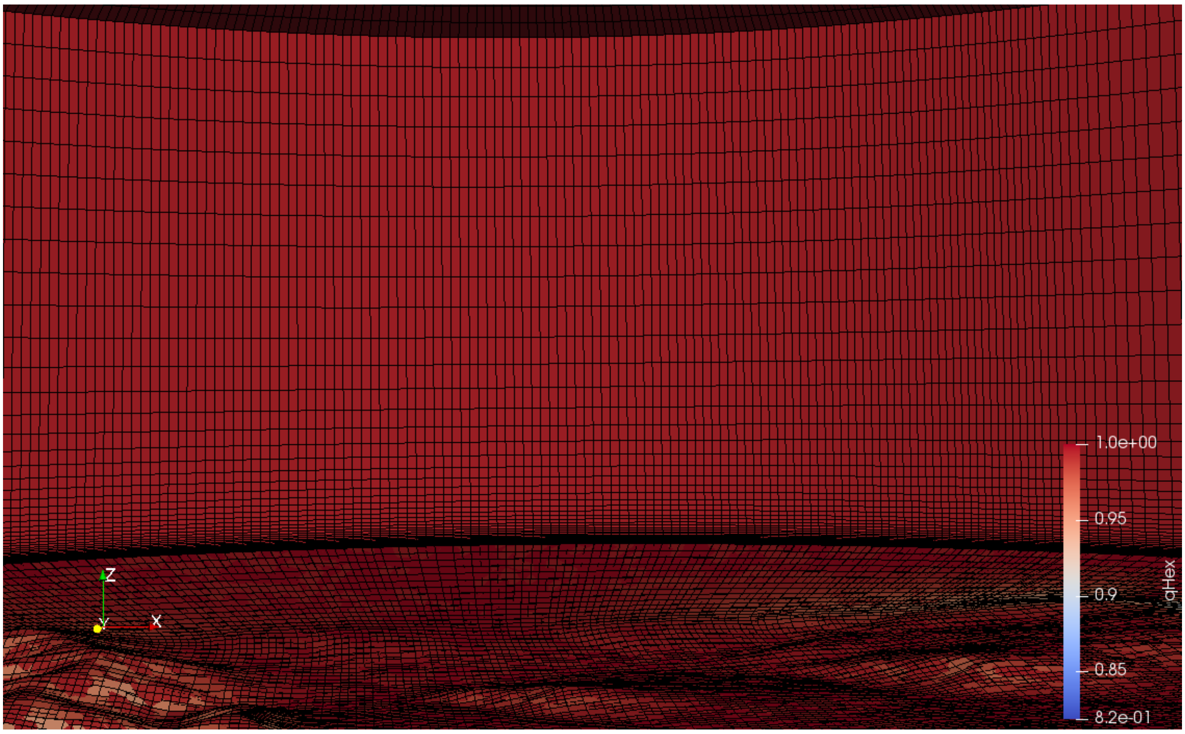

Figure 3.9: ABL mesh generation: zoom inside the volume mesh

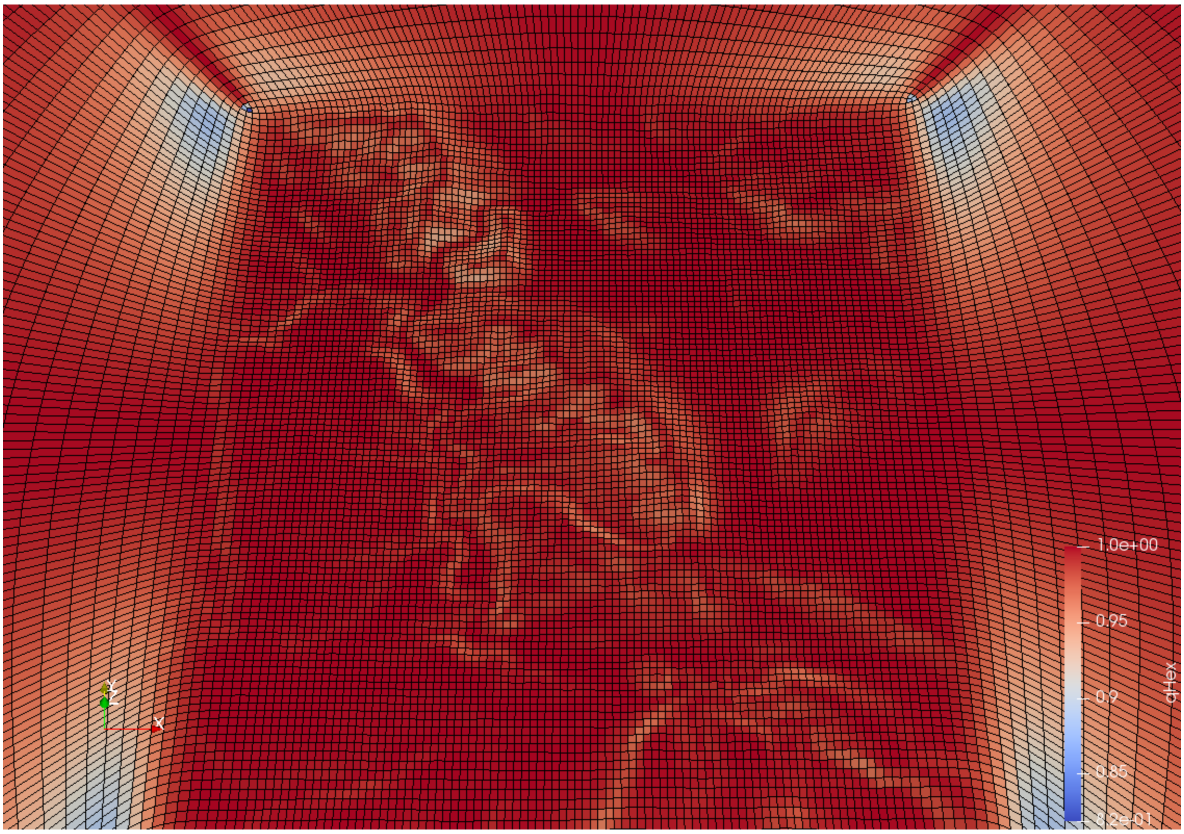

Figure 3.10: ABL mesh generation: quality of the hexahedral elements, top view

3.3 An alternative experimental approach: rotated mesh and buffer impact

This section faces an alternative and computationally easier approach to generate the mesh, that basically consists in rotating the mesh according to the prevailing wind direction (217°, clockwise from the north) and excluding the buffer region.
The aim is to evaluate which is the impact these two differences have on both numerical results and computation time, especially when, as in the present case, the terrain is complex. The procedure adopted to generate that, is the same described in the previous section, and the exclusion of the buffer as well as the mesh rotation angle are imposed directly in the input file; then the Alya mesher, which is automatic and quite robust, will generate the final mesh adapted to the selected (modified) input data.
Also in this case, different mesh cell sizes have been tested (20,30,40 and 60m) and numerical results have been compared between them and w.r.t to the previous full mesh; but before performing numerical simulation, some important considerations, related to these two exceptions, can be made right away.
The first is that, the surrounding of the hill is quite flat and homogenous and so, the mesh quality both of quadrilateral and hexahedral elements, in that region will keep high, above 0.9; when instead moving towards the corners, the terrain preserves

those two characteristics but due to the domain (square) and mesh shape, quality starts decreasing by a lower extent, being always above 0.8 (see figures 3.7, 3.10, 3.15 and 3.16).
Now, imagining to rotate the mesh only, without excluding the buffer, which by definition is set flat and homogenous as well (so as to accomodate the flow and used to impose BCs), it can be easily guessed as, regardless the presence of the corner, the mesh quality is still high in that area and so wind flow conditions would not change to a great extent when crossing the left-long side instead of the corner of the square internal domain. For these reasons, stricly related to the site being analysed, the mesh rotation has a minor effect on numerical results.
The second consideration, instead, is related to the exclusion of the buffer; clearly, by removing that region from the whole domain, the number of nodes and elements used to build the final mesh decrease drastically; this is an obvious advantage that reduces both the time needed to generate the mesh itself and then, the computation time when solving the mathematical model with the Alya solver; but, since the buffer is meant to generate continuity with the wind farm mesh so as to make it smoother, by doing so, this one comes to be more stretched; this drawback, in practice, causes a reduction of the mesh quality, not in the surroundings but in the wind farm area, i.e where terrain gradients are more pronounced; this in turn leads to get slighlty under or overestimated numerical results.

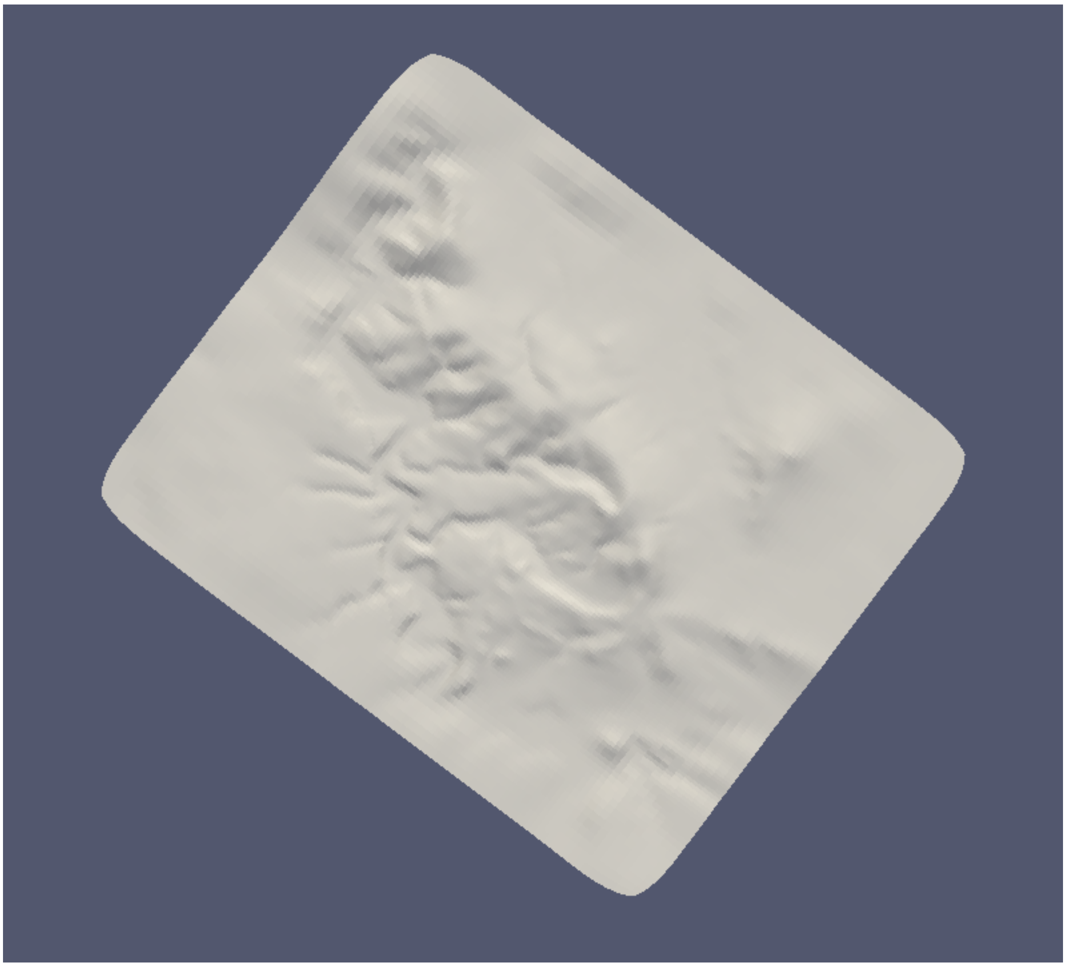

Figure 3.11: Mesh rotation process without buffer: topography, top view

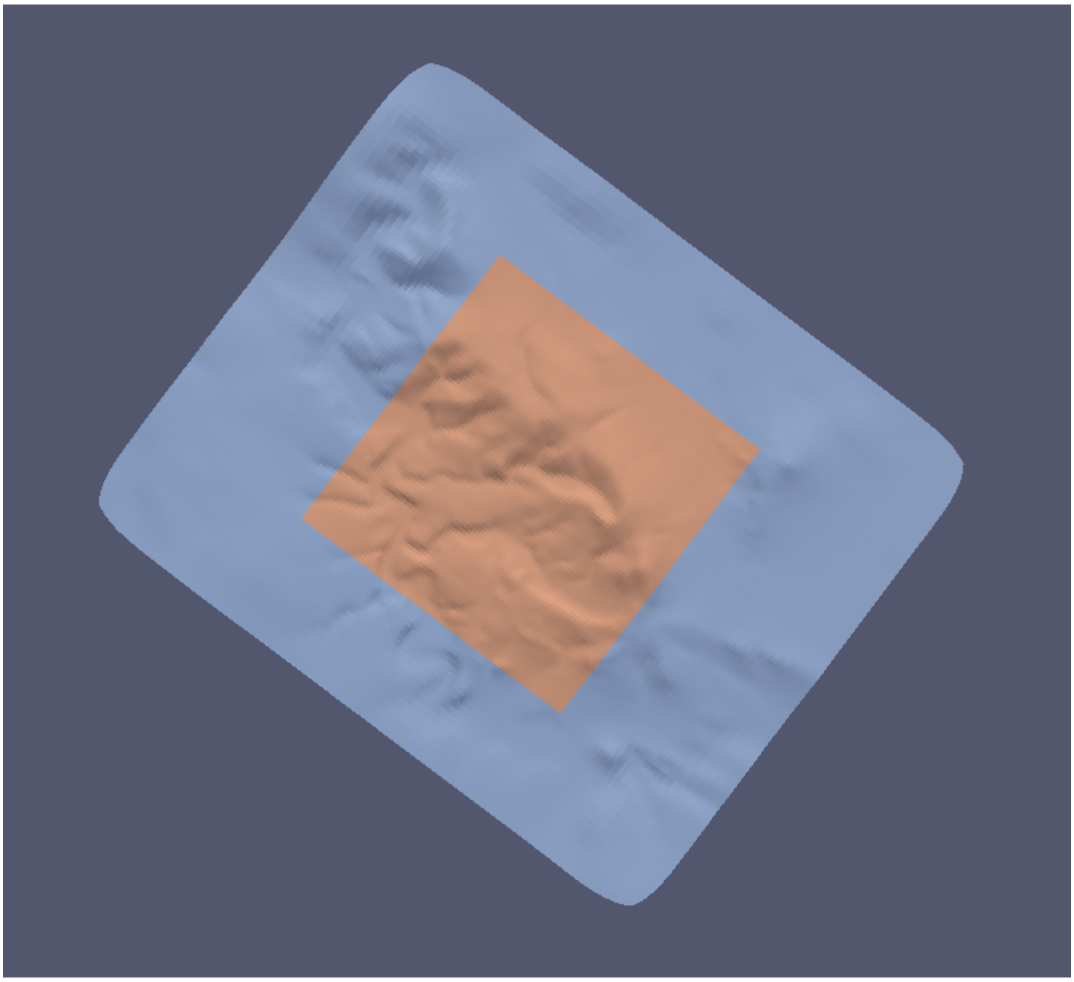

Figure 3.12: Mesh rotation process without buffer: domain regions

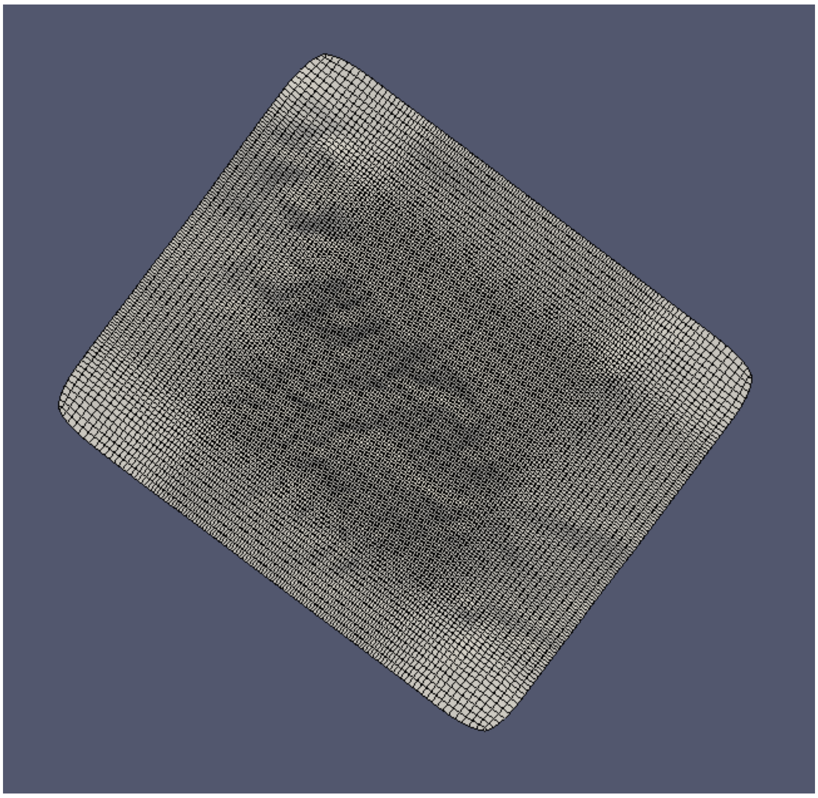

Figure 3.13: Rotated mesh without buffer: quadrilateral topography surface mesh, top view

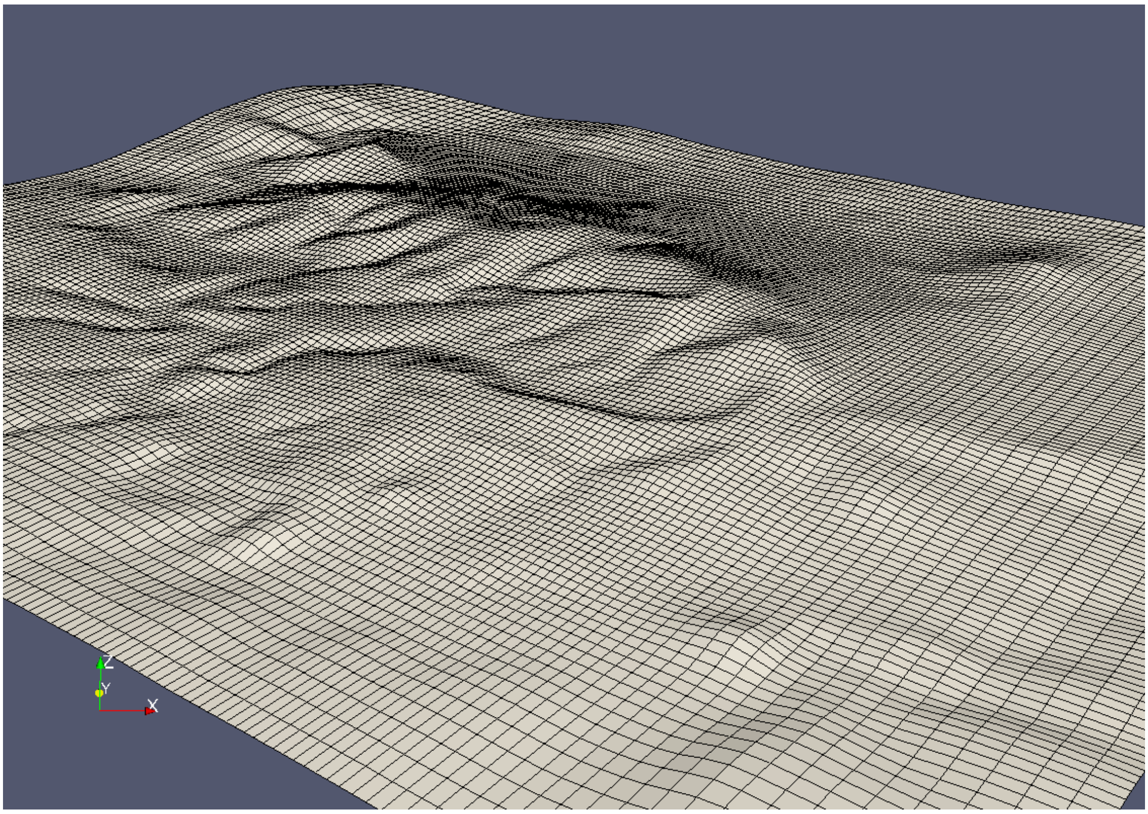

Figure 3.14: Rotated mesh without buffer: quadrilateral topography surface mesh, zoom on the hill

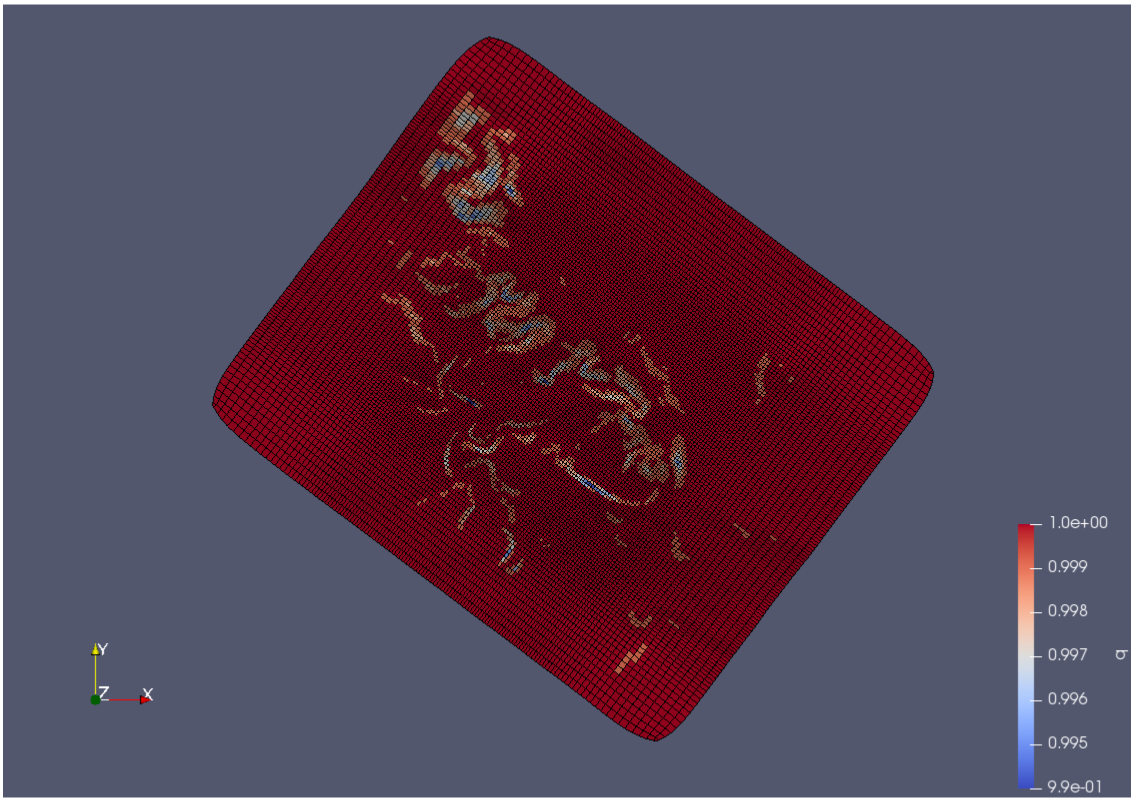

Figure 3.15: Rotated mesh without buffer: optimized topography surface mesh, top view

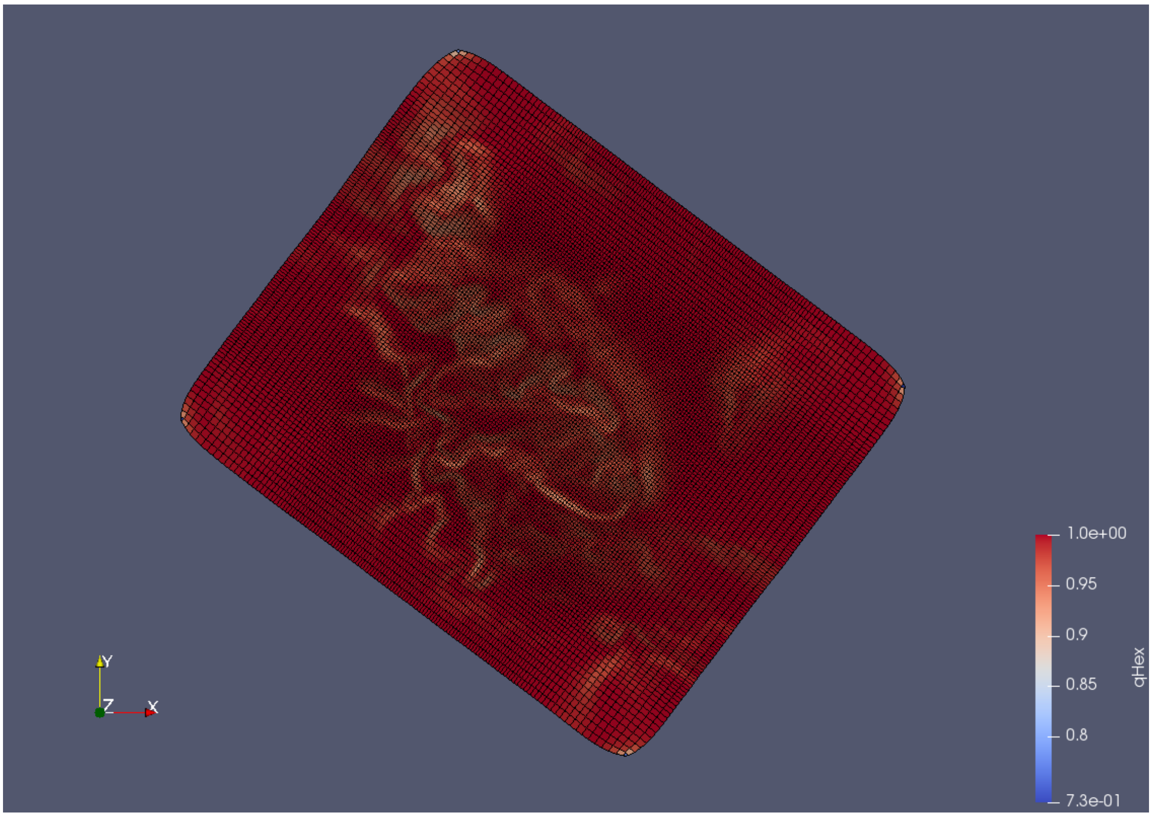

Figure 3.16: Rotated ABL volume mesh without buffer: quality of the hexahedral elements, top view

3.4 Statistics of the meshes

This section provides a list of tables containing the statistics of the generated volume meshes, both non-rotated with buffer (see tables 3.1 and 3.2) and rotated without buffer (see tables 3.3 and 3.4), for different cell sizes of the wind farm area; statistics, for each of the two cases and for each cell size, indicate the number of nodes, hexahedral elements and outer boundaries, the total time required to generate the volume mesh itself and its quality (min, max and mean).

Firstly, considering one only of the two case, e.g the first one (non-rotated mesh with buffer), it can be noticed that, by comparing one mesh cell size w.r.t its double, e.g 20m and 40m, the number of total nodes, elements and boundaries for 20m are about the triple of the 40m ones, as well as the generation time (see Table 3.1, first and third row); the same occurs for 30m and 60m (see Table 3.1, second and fourth row). An identical situation verifies also in the second case (rotated mesh without buffer).

Secondly, by reasoning backwards, i.e comparing the two case but for the same cell size, also in this case the results will be about three times the other (see Table 3.1 and 3.3). So, basically, doubling the cell size, regardless the presence of the buffer, or excluding the buffer by keeping fixed the cell size, have the same impact on the final mesh in terms of number of nodes, elements, boundaries and total time.

However, despite these huge differences, changing the mesh cell size does not affect either minimum or mean quality on a large extent; actually the variations are unperceivable and range from 0.01 to 0.02 (see Table 3.2 and 3.4); when instead the buffer is not accounted for and the cell size is kept fixed, those differences rise to 0.08; the worst condition occurs when also the cell size is modified (increased) and leads to a reduction of the minimum quality up to 0.1.

This demonstrates how the buffer, in comparison with the cell size, has a more relevant impact on the mesh quality. However, it is worthwhile to specify that quality values above 0.75 are indicative of an excellent mesh and so if WTs are not considered, the first case (with the buffer) would be fine since the mesh (min.) quality value is always above 0.8, while the second case (without the buffer) would be at the limit between a good quality mesh and an excellent one, since that varies from 0.74 to 0.72.

Furthermore, it is important to remind that, if instead WTs are considered, the ABL volume mesh is the input for the generation of the wind farm one; during this process WTs are insterted and the mesh around them is refined properly so as to capture the upwind/wake effects; these additional meshing operations increase the number of geometrical constraints, which in turn lower the minimum quality of the final mesh. For this reason in order to keep the minimum quality of the wind farm mesh high, it is mandatory to obtain an excellent one at the previous step, i.e for the ABL volume mesh.

Cell size	#nodes	#elements	#boundaries	Tot. time
20	4940750	4813956	252348	19.404 s
30	2605700	2533986	142530	10.074 s
40	1689000	1639932	97414	6.405 s
60	957750	927668	59620	3.743 s

Table 3.1: Statistics of the meshes: non-rotated mesh with buffer

Min. quality	Max. quality	Mean quality	Standard deviation
0.82	1.00	0.99	0.01
0.82	1.00	0.99	0.01
0.81	1.00	0.98	0.01
0.80	1.00	0.97	0.02

Table 3.2: Statistics of the meshes: non-rotated mesh with buffer

Cell size	#nodes	#elements	#boundaries	Tot. time
20	1725750	1673056	104548	6.525 s
30	895350	864360	61348	3.301 s
40	575000	553014	43446	2.083 s
60	306000	292236	27118	1.092 s

Table 3.3: Statistics of the meshes: rotated mesh without buffer

Min. quality	Max. quality	Mean quality	Standard deviation
0.74	1.00	0.99	0.01
0.74	1.00	0.99	0.01
0.73	1.00	0.98	0.02
0.72	1.00	0.97	0.02

Table 3.4: Statistics of the meshes: rotated mesh without buffer

Chapter 4

Numerical simulation without WTs

In this chapter, the resulting meshes (from Chapter 3) are used to solve the RANS equations with a modified $k-\varepsilon$ turbulence model adapted to a neutral ABL, without WTs (see Chapter 2). More in detail, as discussed in the previous chapters, several simulations have been performed by following two different mesh generation approaches, i.e non rotated mesh (NR) with buffer (B) and rotated mesh (R) without buffer (NOB), and for four wind farm cell sizes, i.e 20, 30, 40 and 60 m; a common pratice, adopted in this work, is to compare results obtained by two wind farm cell sizes, where one is the double of the other.

Section 4.1 focuses on the MetMast MM200, which is located on the Rödeser Berg hill at 386 m above the sea level; besides, this location is forested, and the trees height is about 20 m. Graphs in this section, show the modulus of the horizontal wind speed (or witness speed, i.e the speed of the witnesses points, inserted along the mast and used to simulate sensors), wind direction, turbulent kinetic energy and pressure (vertical) profiles up to 2000 m, which represents the top of the domain, and with a zoom on the first 188 m. This is done in order to evaluate the overall wind behaviour both in the ABL and ASL.

Section 4.2 instead, deals with the mesh convergence analysis and shows the convergence of the residual L_2 trends for both RANS and $k-\varepsilon$ equations.

Eventually, Section 4.3 contains figures displaying the behaviour of all those listed wind flow variables around the ABL, at the ground, and at different heights (horizontal cuts), i.e 60, 70, 80 and 105 m.

4.1 Results at met mast MM200

Once the velocity field $\boldsymbol{u}$ is calculated, it is possible to extract velocity vectors at MM200, so as to obtain information about its components and directions. The three mean speed components are U, V and W and refer respectively to the x, y and z axis. The modulus of the horizontal (mean) velocity is computed as $(U^2+V^2)^{\frac{1}{2}}$ while the TKE as $k=\frac{1}{2}\overline{\boldsymbol{u}'\boldsymbol{u}'}=\frac{1}{2}(\overline{u'^2}+\overline{v'^2}+\overline{w'^2})$,using Eq (27).

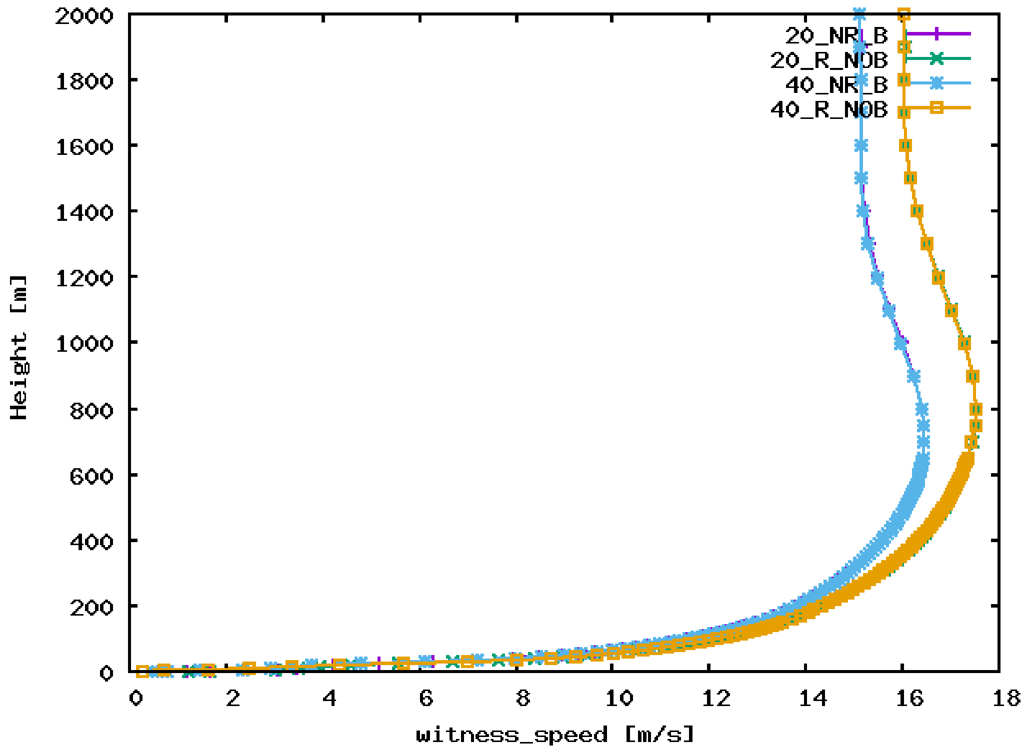

Figure 4.1: Horizontal mean velocity profiles up to 2000 m: comparisons between 20m and 40m cell size for both meshing procedures

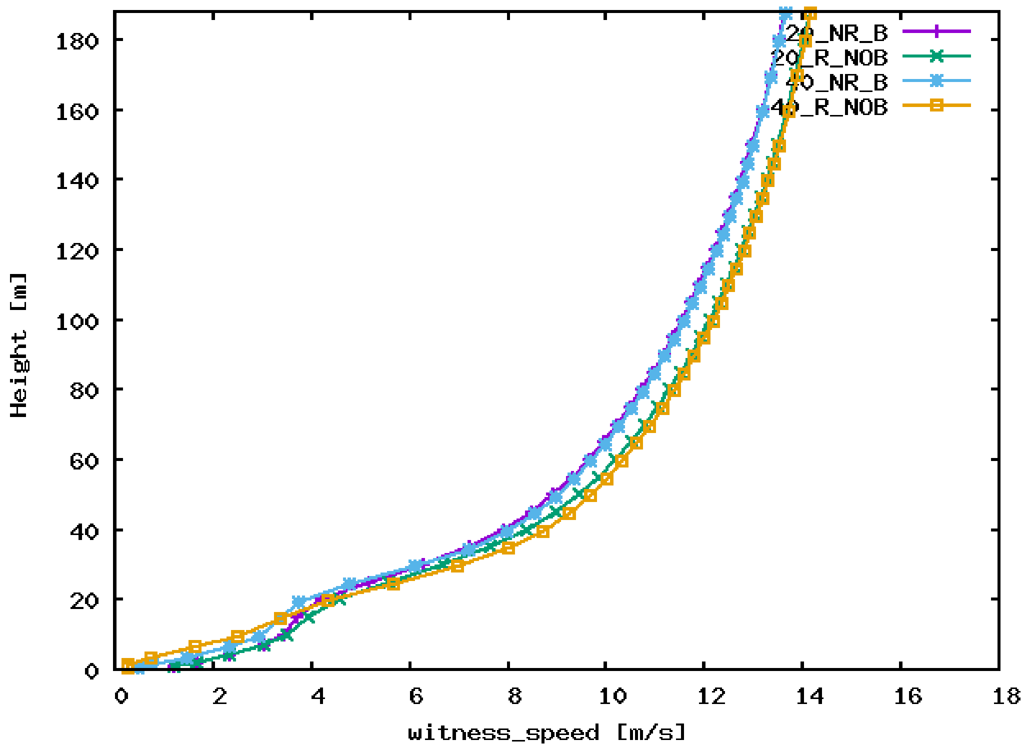

Figure 4.2: Horizontal mean velocity profiles up to 188 m: comparisons between 20m and 40m cell size for both meshing procedures

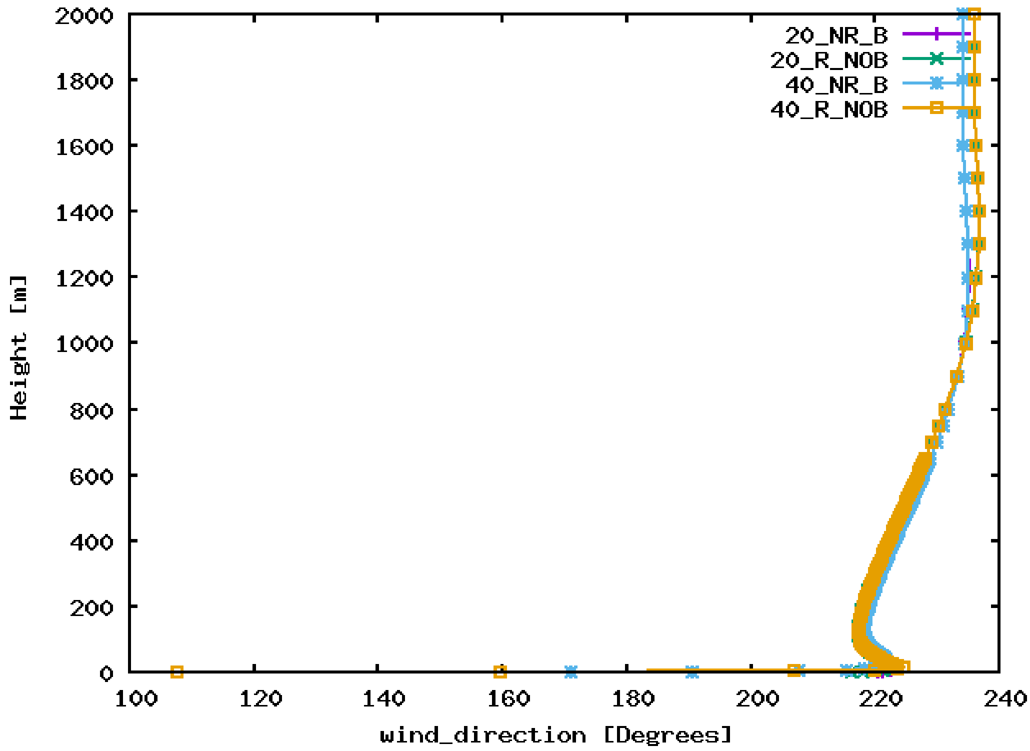

Figure 4.3: Wind direction profiles up to 2000 m: comparisons between 20m and 40m cell size for both meshing procedures

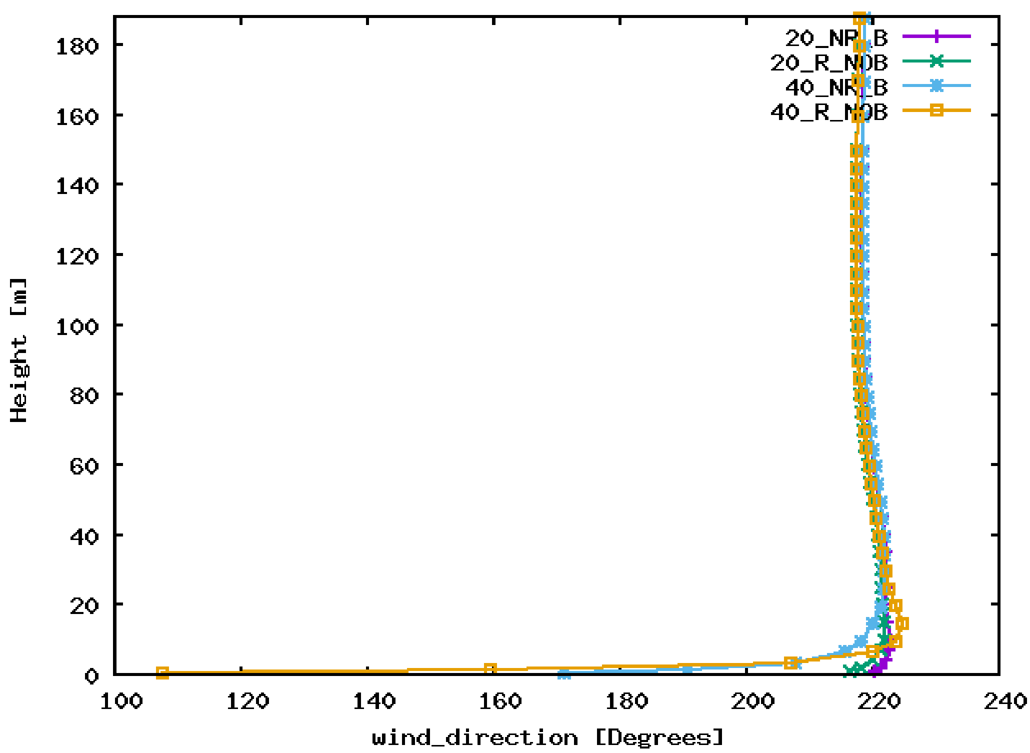

Figure 4.4: Wind direction profiles up to 188 m: comparisons between 20m and 40m cell size for both meshing procedures

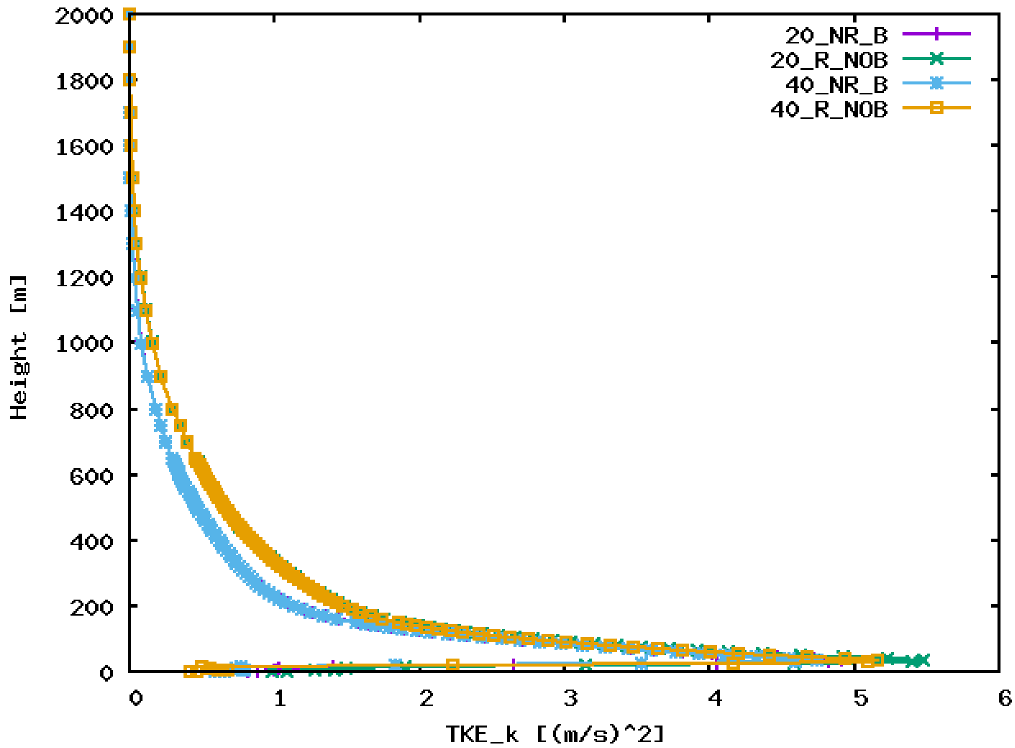

Figure 4.5: TKE profiles up to 2000 m: comparisons between 20m and 40m cell size for both meshing procedures

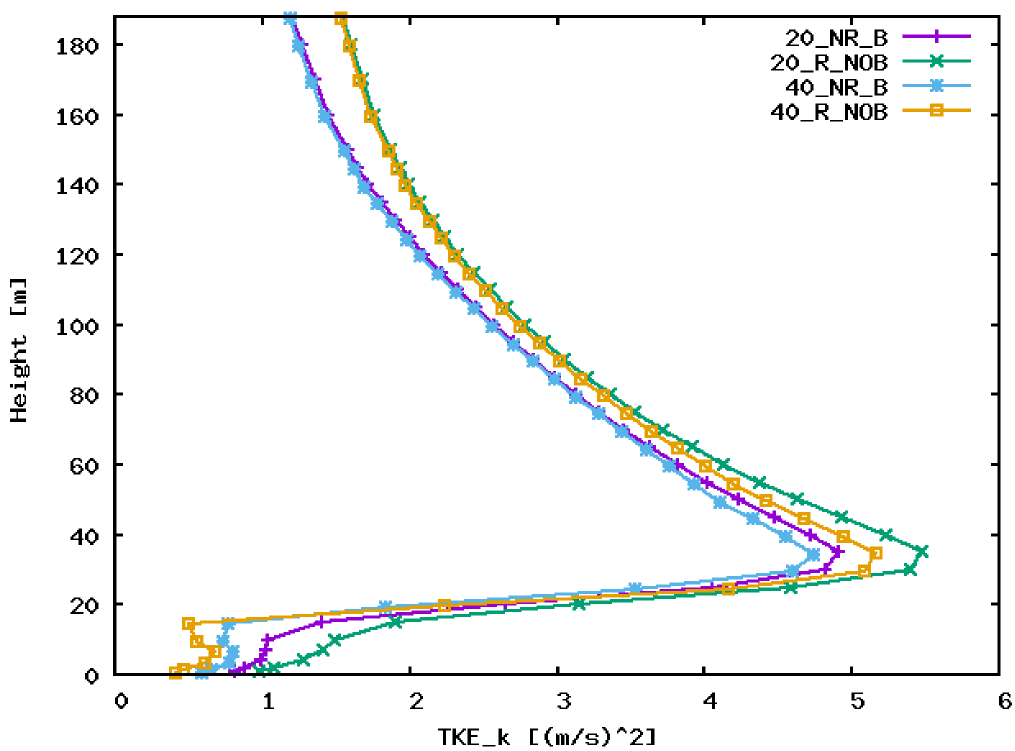

Figure 4.6: TKE profiles up to 188 m: comparisons between 20m and 40m cell size for both meshing procedures

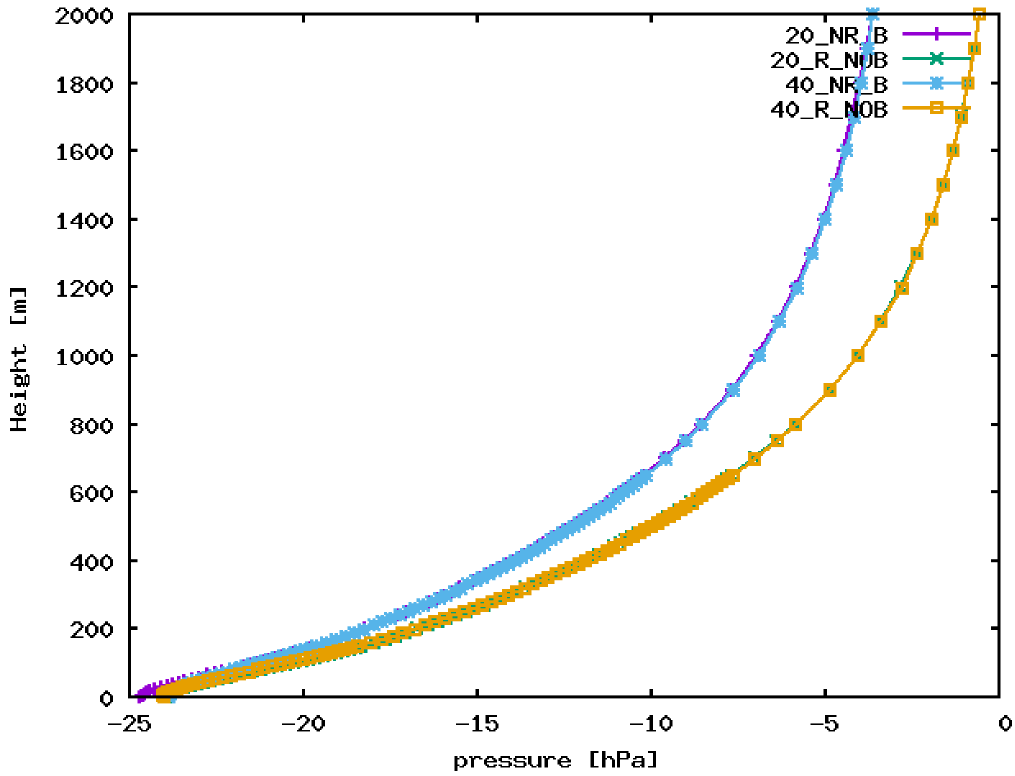

Figure 4.7: Pressure profiles up to 2000 m: comparisons between 20m and 40m cell size for both meshing procedures

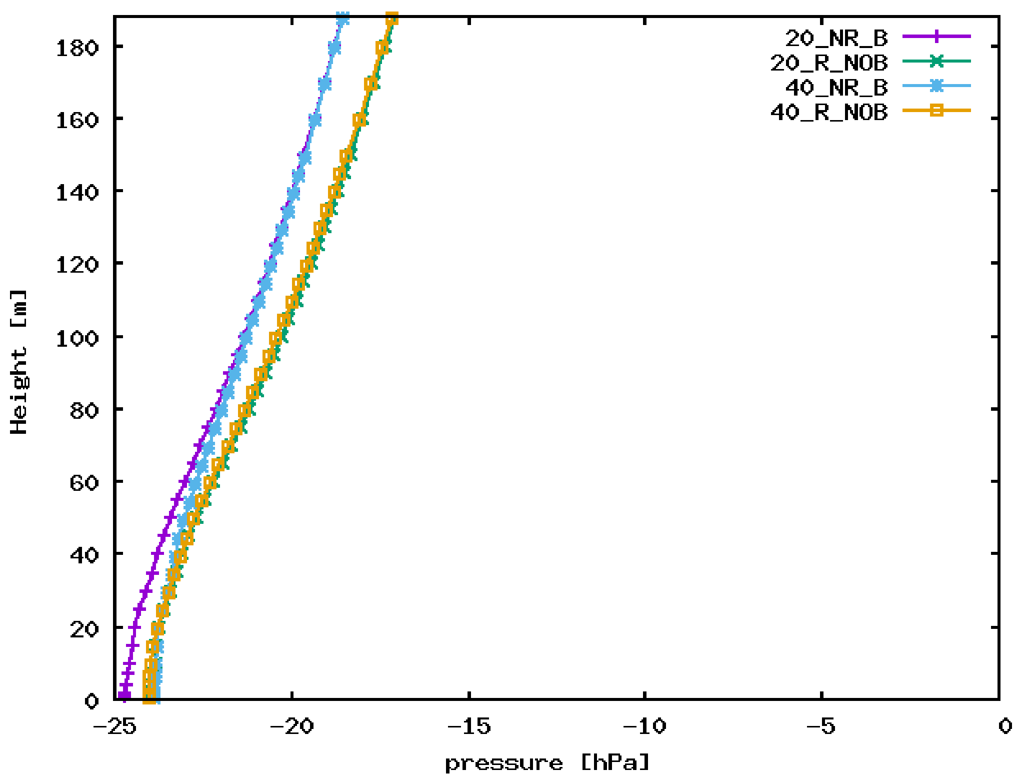

Figure 4.8: Pressure profiles up to 188 m: comparisons between 20m and 40m cell size for both meshing procedures

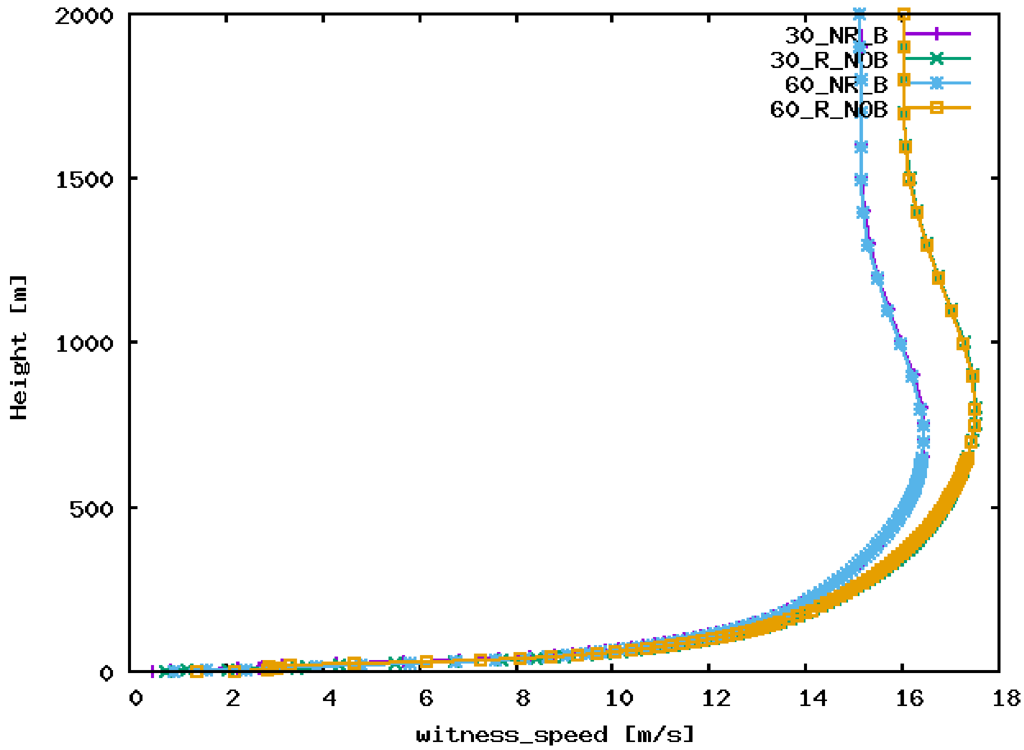

Figure 4.9: Horizontal mean velocity profiles up to 2000 m: comparisons between 30m and 60m cell size for both meshing procedures

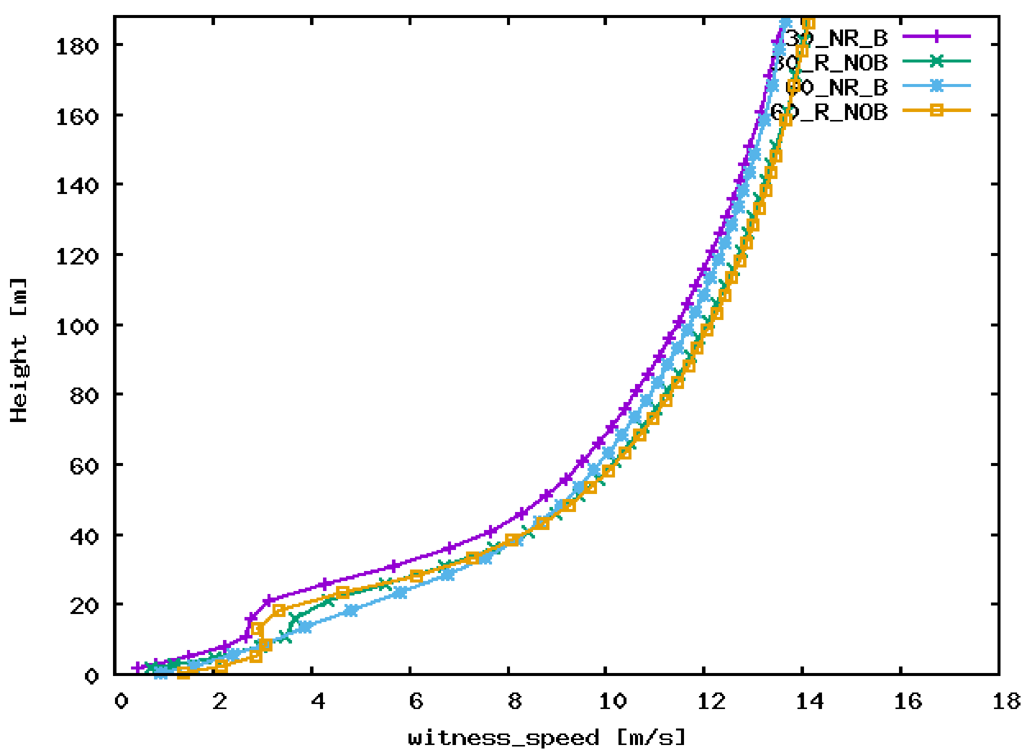

Figure 4.10: Horizontal mean velocity profiles up to 188 m: comparisons between 30m and 60m cell size for both meshing procedures

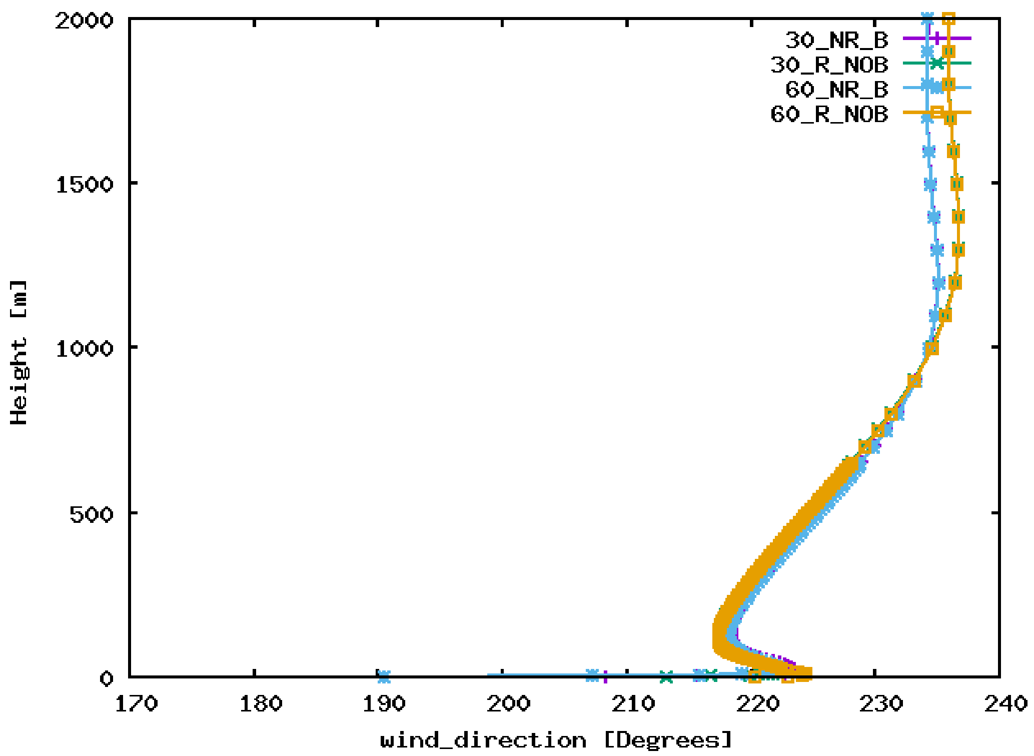

Figure 4.11: Wind direction profiles up to 2000 m: comparisons between 30m and 60m cell size for both meshing procedures

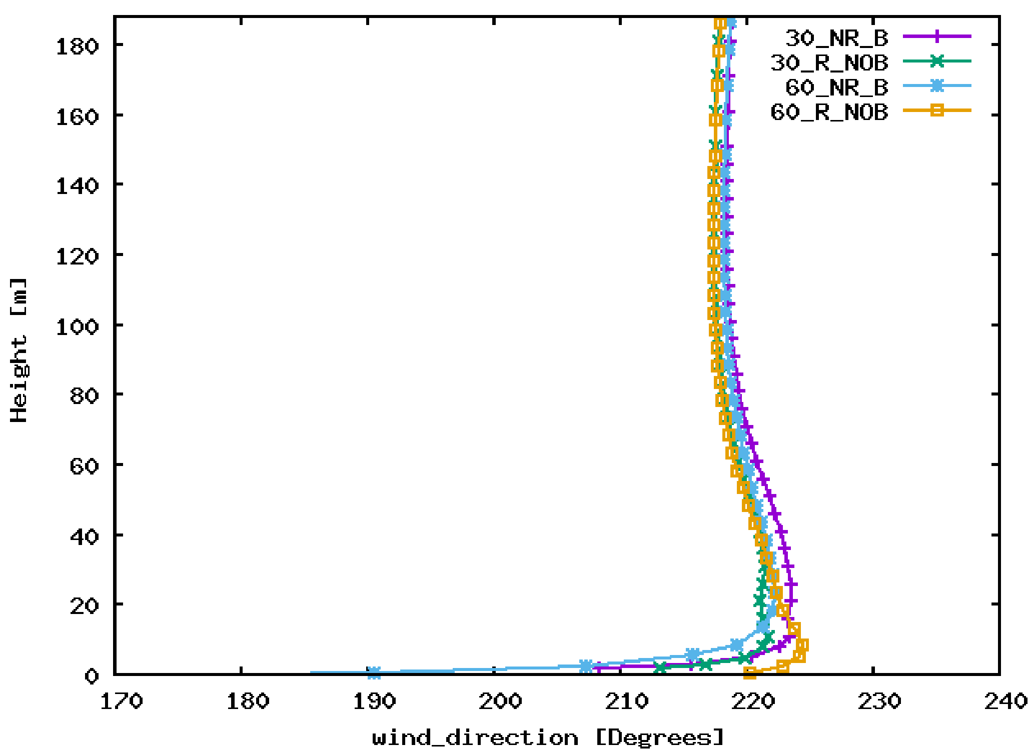

Figure 4.12: Wind direction profiles up to 188 m: comparisons between 30m and 60m cell size for both meshing procedures

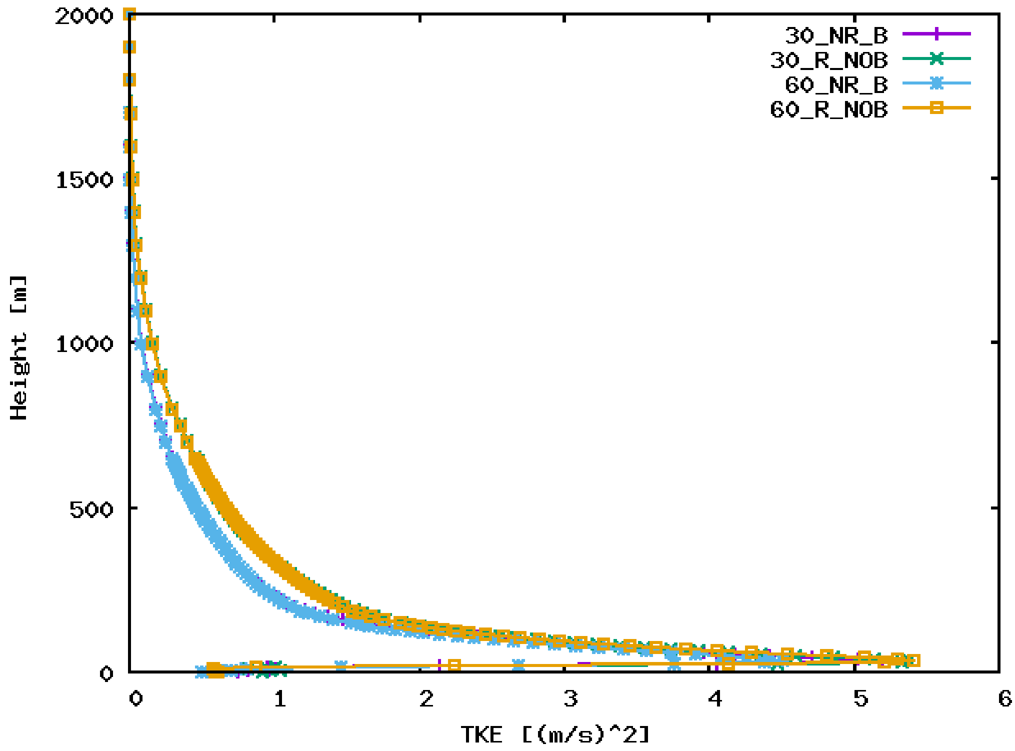

Figure 4.13: TKE profiles up to 2000 m: comparisons between 30m and 60m cell size for both meshing procedures

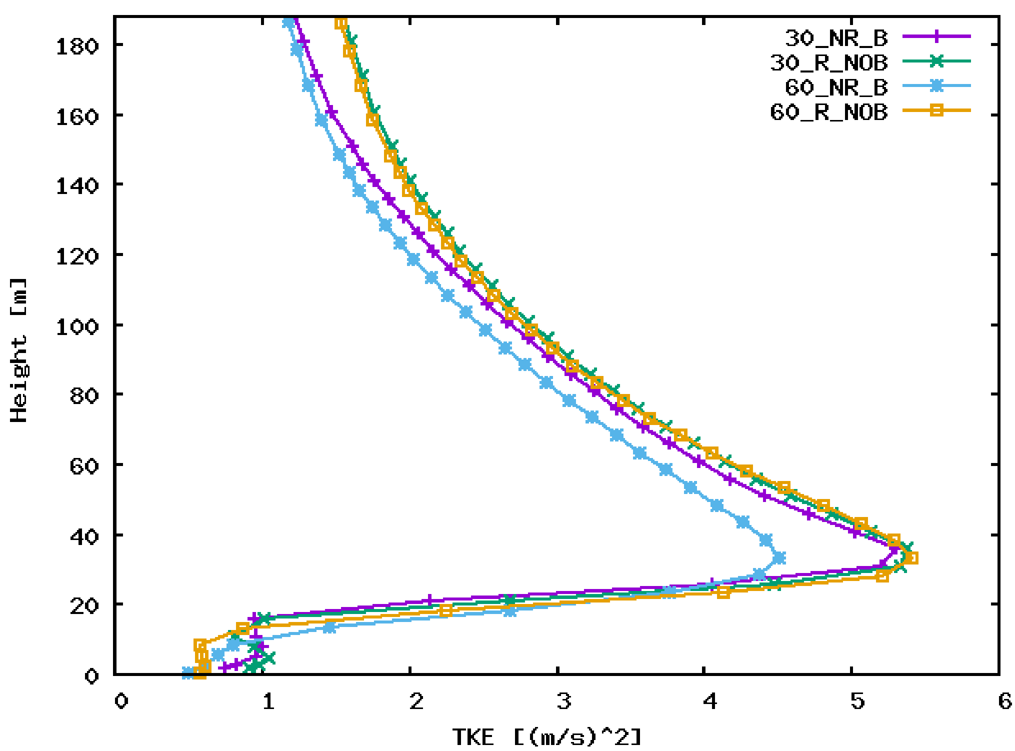

Figure 4.14: TKE profiles up to 188 m: comparisons between 30m and 60m cell size for both meshing procedures

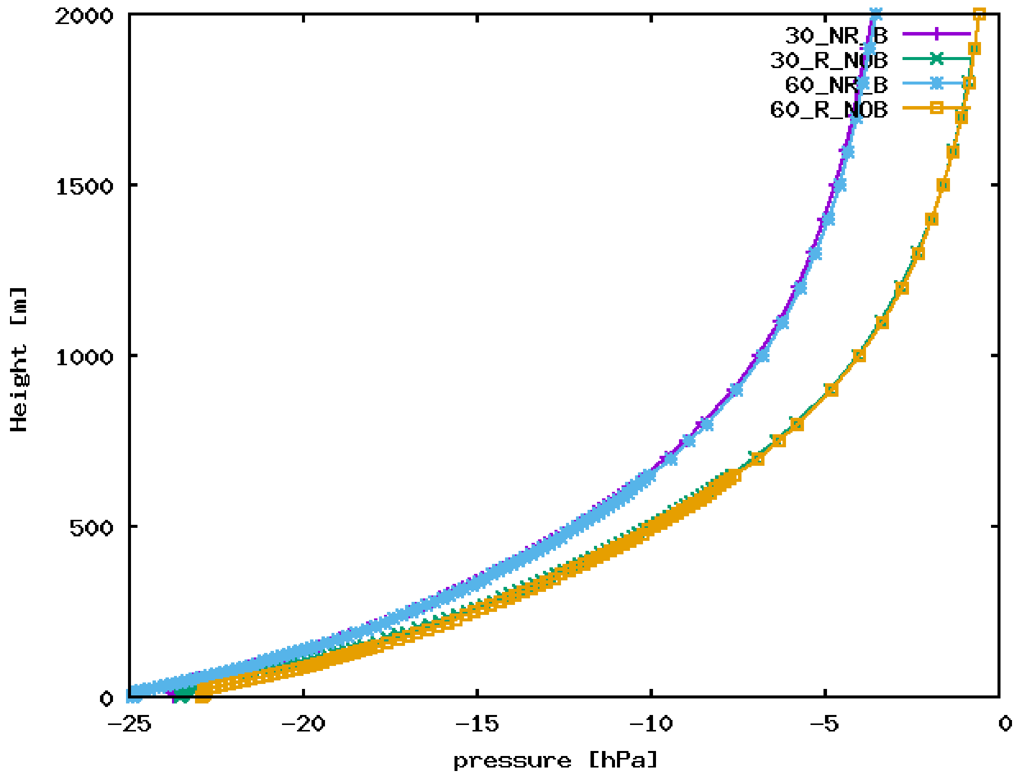

Figure 4.15: Pressure profiles up to 2000 m: comparisons between 30m and 60m cell size for both meshing procedures

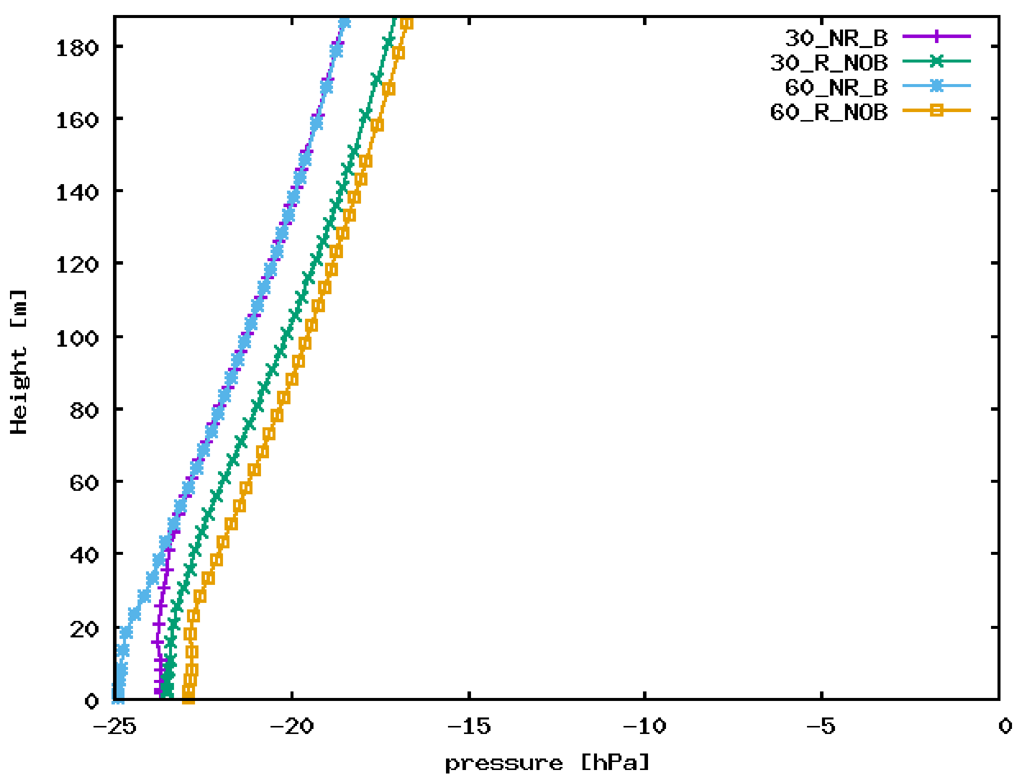

Figure 4.16: Pressure profiles up to 188 m: comparisons between 30m and 60m cell size for both meshing procedures

From these results it can be immediately noticed as the differences between vertical profiles computed for different mesh cell sizes (horizontal resolution) but adopting the same mesh generation procedure, are unperceivable; these differences, instead, enlarge when comparing the two mesh generation approaches by keeping fixed the cell size. Therfore, what really affects the numerical results is the absence of the buffer rather than the value itself of the mesh cell size, thus confirming the considerations made in Section 3.4.

In fact, looking more closely, the difference between the horizontal wind velocity profiles, from 200 meters up, starts to increase, leading to a difference in the geostrophic value of 1.5-2.0 m/s (see Figures 4.1, 4.9). From Figures 4.2 and 4.10 instead, it is possible to visualise the forest effect in between the first 20 m and slighlty above it; the velocity in this region increases slowly due to the resistence offered by the canopy itself, which traduces in strong friction and tubulence effects; once it overcomes the first 40 m, friction and tubulence effects become less important, going to zero for very high heights (see Figures 4.5, 4.6, 4.13, 4.14); in parallel, the (mean) velocity starts increasing more rapidly until it reaches the geostrophic value (above 1600 m).
The wind direction instead does not experience large variations either in the ASL or in the whole ABL (see Figures 4.3, 4.4, 4.11, 4.12). In contrast, pressure profiles (Figures 4.7, 4.8, 4.15, 4.16) obtained with the two meshing procedures, experience an increasing difference from the bottom to the top, reaching a maximum value of 5 hPa. The negative sign is just indicating the presence of two main areas, out of which the first is characterized by high pressure value while the second by a low one. Table 4.1 shows the experimental data that need to be matched with the numerical ones so as to drive the simulation correctly all over the terrain. Table 4.2 instead, lists the numerical results.

	at 60 m	at 188 m
Wind speed	9.6 m/s	13.9 m/s
Wind direction	219.7°	221.7°

Table 4.1: Experimental data at MM200

		Wind Speed		Wind Direction	
Cell size	Mesh_Buffer	at 60 m	at 188 m	at 60 m	at 188 m
20	NR_B	9.6 m/s	13.7 m/s	220.25°	218.8°
20	R_NOB	10.3 m/s	14.2 m/s	219.2°	217.95°
30	NR_B	9.6 m/s	13.7 m/s	220.8 °	218.9°
30	R_NOB	10.3 m/s	14.2 m/s	219.4 °	217.95°
40	NR_B	9.8 m/s	13.6 m/s	220.6 °	218.7°
40	R_NOB	10.5 m/s	14.2 m/s	220.0 °	218.0°
60	NR_B	10.0 m/s	13.6 m/s	220.1°	218.8°
60	R_NOB	10.3 m/s	14.3 m/s	219.3°	218.0°

Table 4.2: Numerical results at MM200

Then by means of $rel_{err}[\%] = (\frac{S_{num}-S_{exp}}{S_{exp}})100$ is possible to compute the relative errors in percentage.

		Relative error [%]			
		Wind Speed		Wind Direction	
Cell size	Mesh_Buffer	at 60 m	at 188 m	at 60 m	at 188 m
20	NR_B	0	-1.4	0.25	-1.3
20	R_NOB	7.3	2.15	-0.22	-1.7
30	NR_B	0	-1.4	0.5	-1.3
30	R_NOB	7.3	2.15	-0.22	-1.7
40	NR_B	2.1	-2.15	0.5	-1.3
40	R_NOB	9.4	2.15	0.1	-1.7
60	NR_B	4.2	-2.15	0.1	-1.3
60	R_NOB	7.3	2.87	-0.22	-1.7

Table 4.3: Relative errors in percentage at MM200

From Table 4.3 it can be noticed that in all the tested cases the relative errors of direction are very low and keep always within a limited range, whereas the ones of the wind velocity are higher, especially for the cases without buffer. On top of these results, the final optimal horizontal mesh resolution results to be 30 m and the choice to insert the buffer comes out to be compulsory.
So for now on, only one wind farm cell size (or horizontal mesh resolution) will be used and the final mesh will be characterized by the presence of the buffer.

4.2 Convergence analysis

This section shows the convergence trends of the continuity, momentum, turbulent kinetic energy k and dissipation rate ε equation for both meshing procedures and for one only mesh resolution, the optimal one (30 m). This is done just because the order of magnitude of L_2-norm of the error, computed as $\|e\|_2 := (\int e^2)^{\frac{1}{2}}$, keeps constant when changing only the mesh resolution. Actually in the first case (non rotated mesh with buffer) the L_2-norm of the error of the momentum equation has an order of magnitude of 10^{-7}, while in the second (rotated mesh with buffer) is 10^{-6}. Furthermore as it can be seen from Figures (4.17, 4.18, 4.19, 4.20) the number of solver iterations is in one case 500 while in the other is 400; this clearly is due to the absence of the buffer which makes the computation faster. In addition, it also causes the convergence trend of the momentum equation to be less smooth.
All the simulations have been run with a Lenovo Legion Y520 Intel Core i7 CPU and with 864 cores and for these two cases the CPU times are respectively 1027.5 s (17.125 min) and 321.46 s (5.36 min). The absence of the buffer leads to reduced computational times, not only for the mesh generation process but also for the simulation itself.

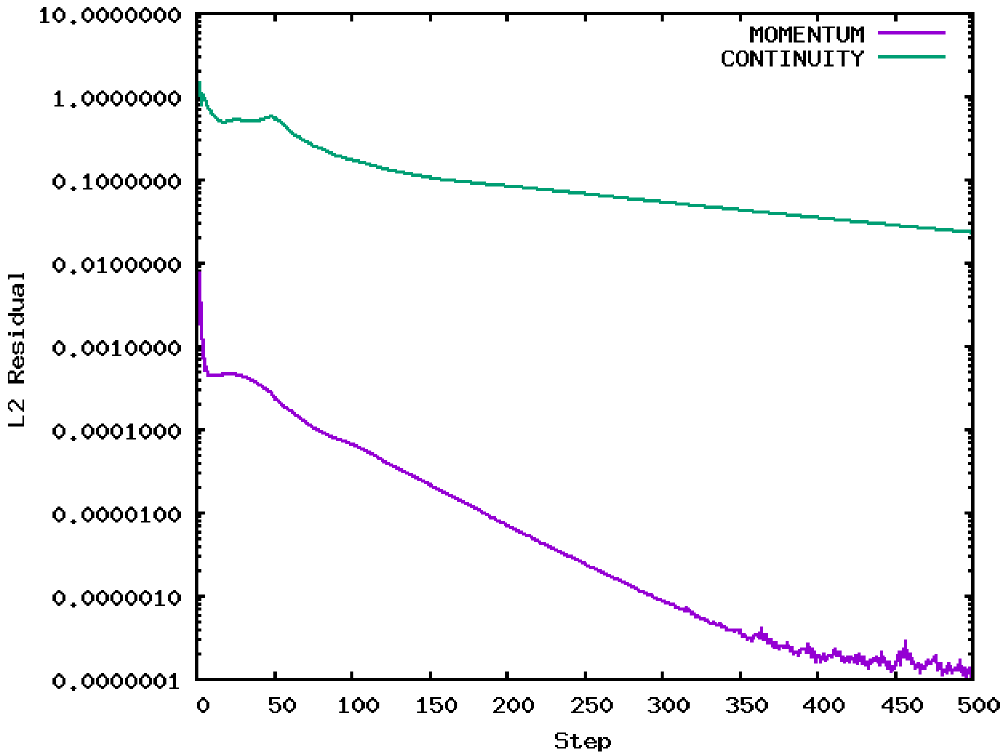

Figure 4.17: Convergence trend of both momentum and continuity equation for the non-rotated mesh with 30m cell size

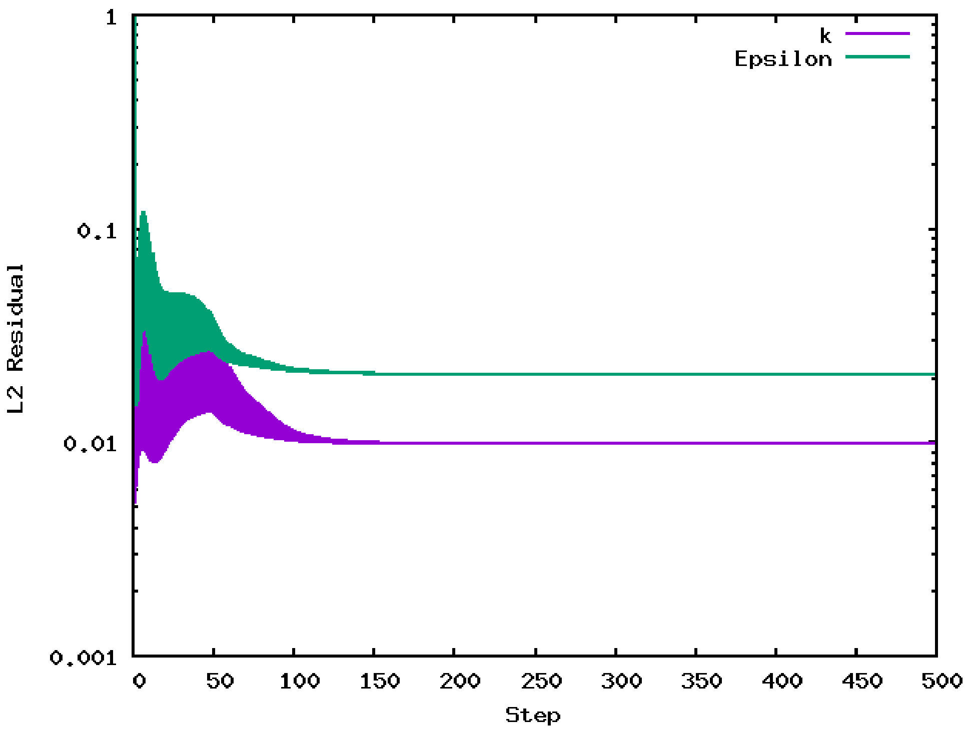

Figure 4.18: Convergence trend of both k and dissipation ε equation for the non-rotated mesh with 30m cell size

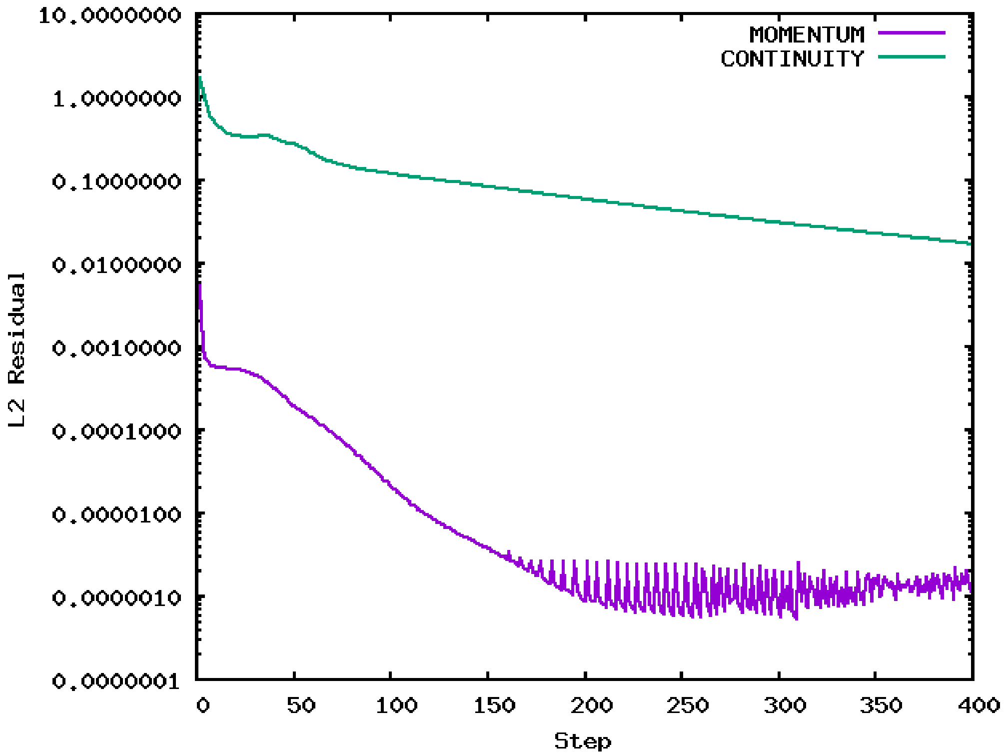

Figure 4.19: Convergence trend of both momentum and continuity equation for the rotated mesh with 30m cell size

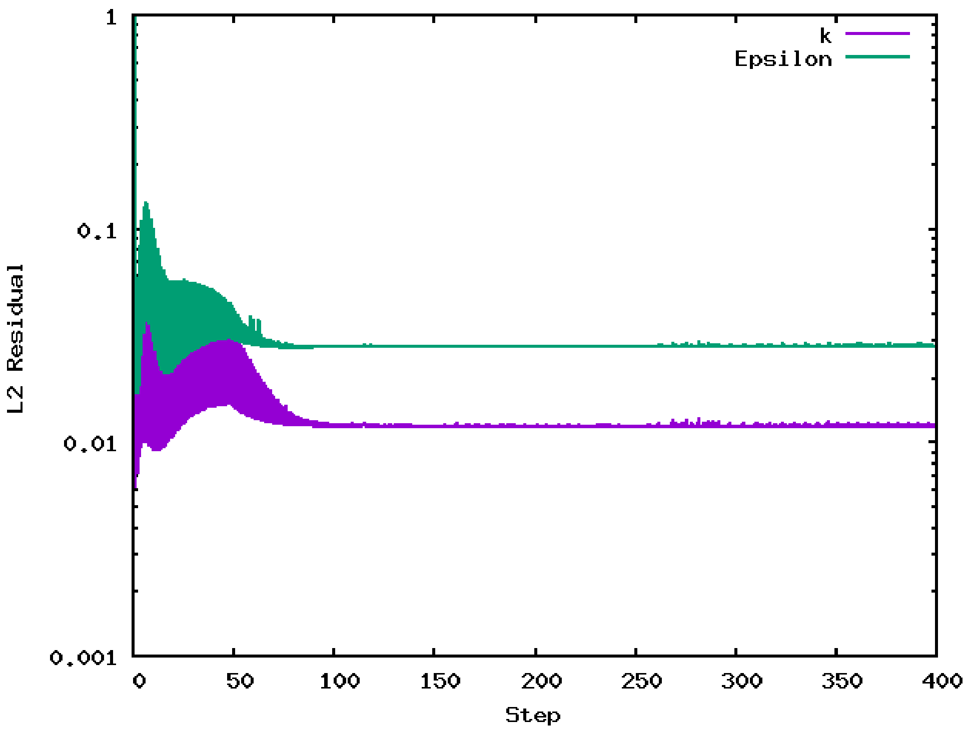

Figure 4.20: Convergence trend of both k and dissipation ε equation for the rotated mesh with 30m cell size

4.3 Postprocess

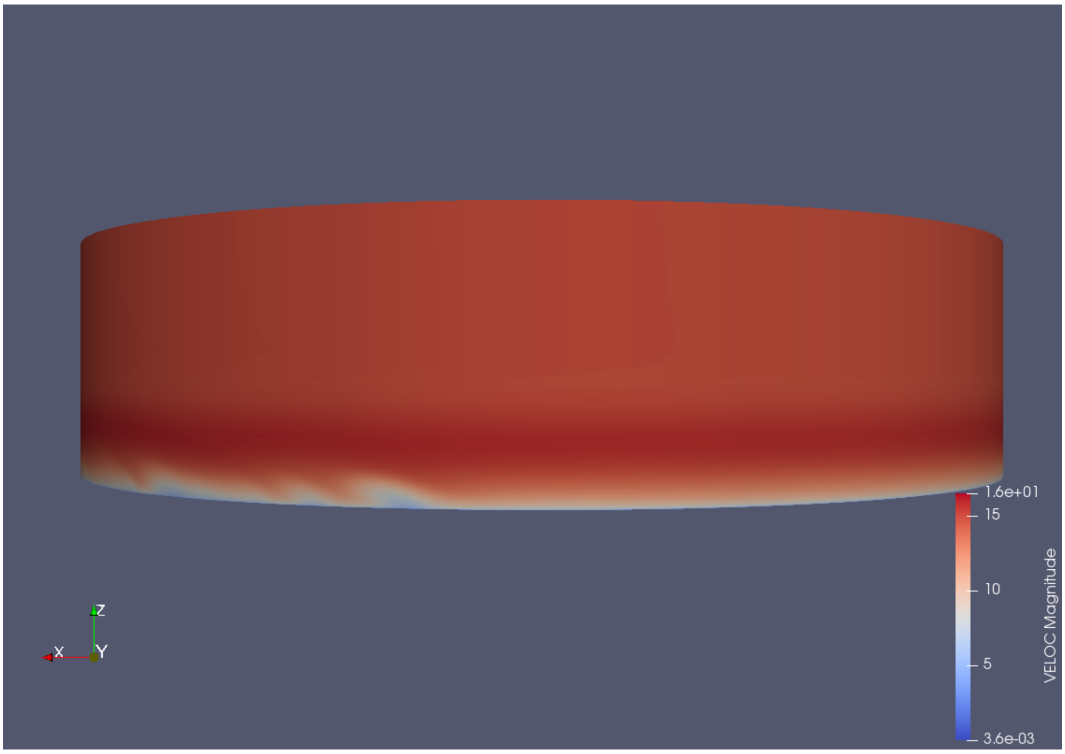

Figure 4.21: Postprocess: Horizontal mean velocity field around the ABL for the non-rotated mesh with buffer and 30m cell size

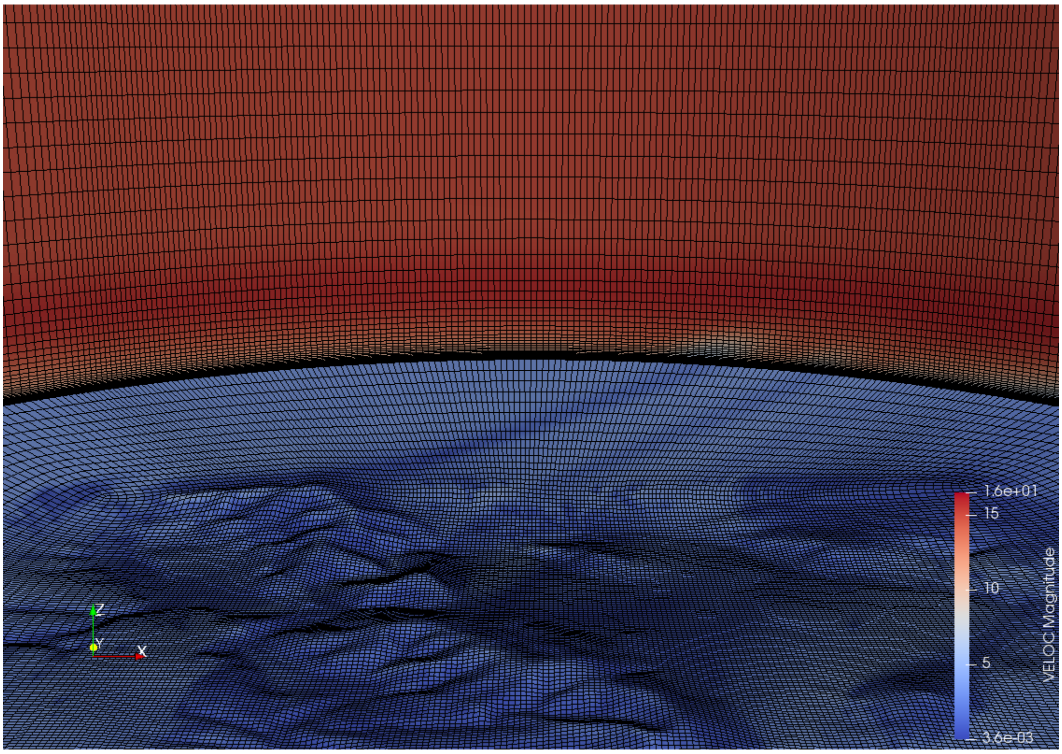

Figure 4.22: Postprocess: Horizontal mean velocity field at the ground for a non-rotated mesh with buffer and 30m cell size

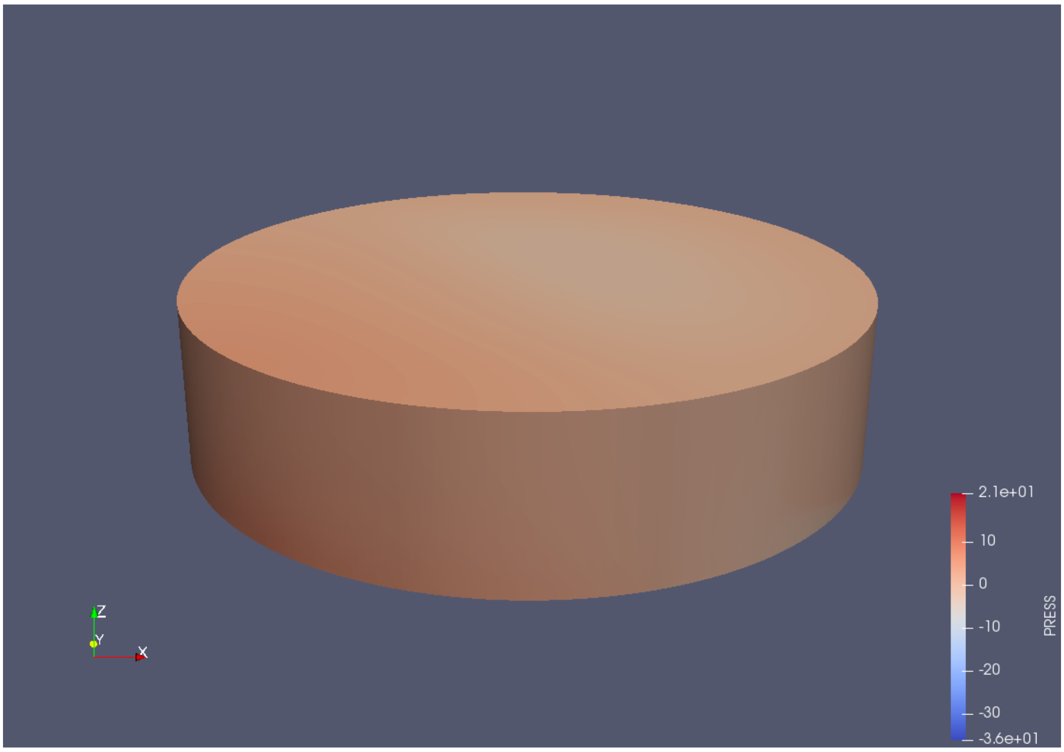

Figure 4.23: Postprocess: pressure field around the ABL for the non-rotated mesh with buffer and 30m cell size

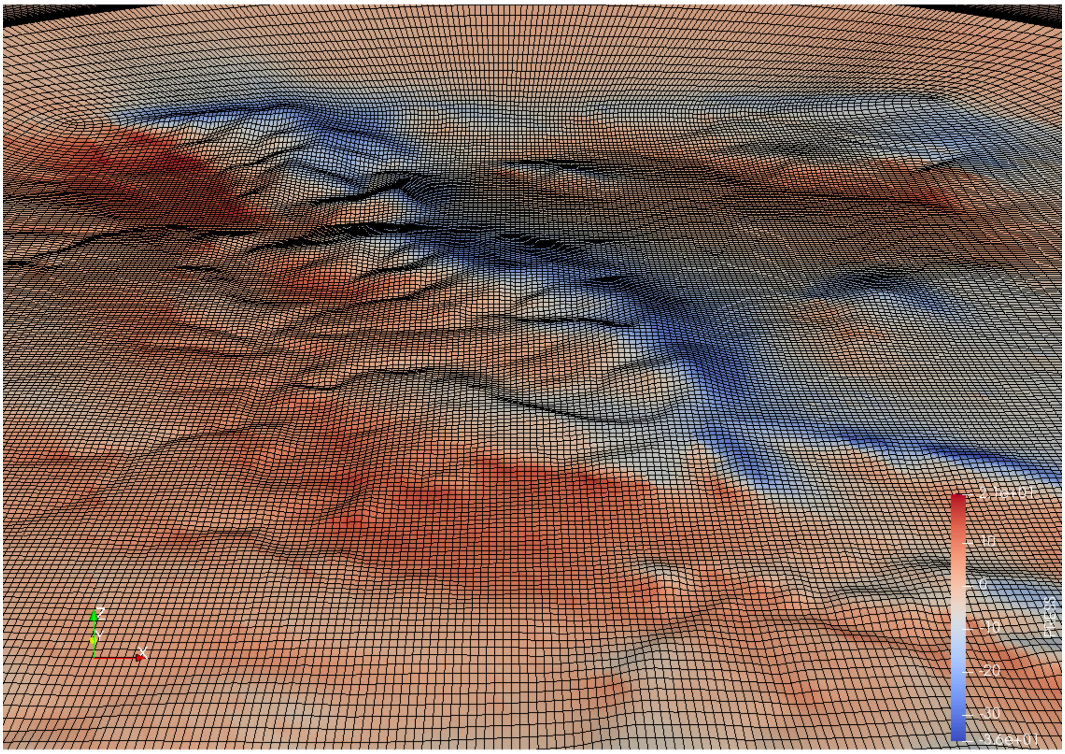

Figure 4.24: Postprocess: pressure field at the ground for the non-rotated mesh with buffer and 30m cell size

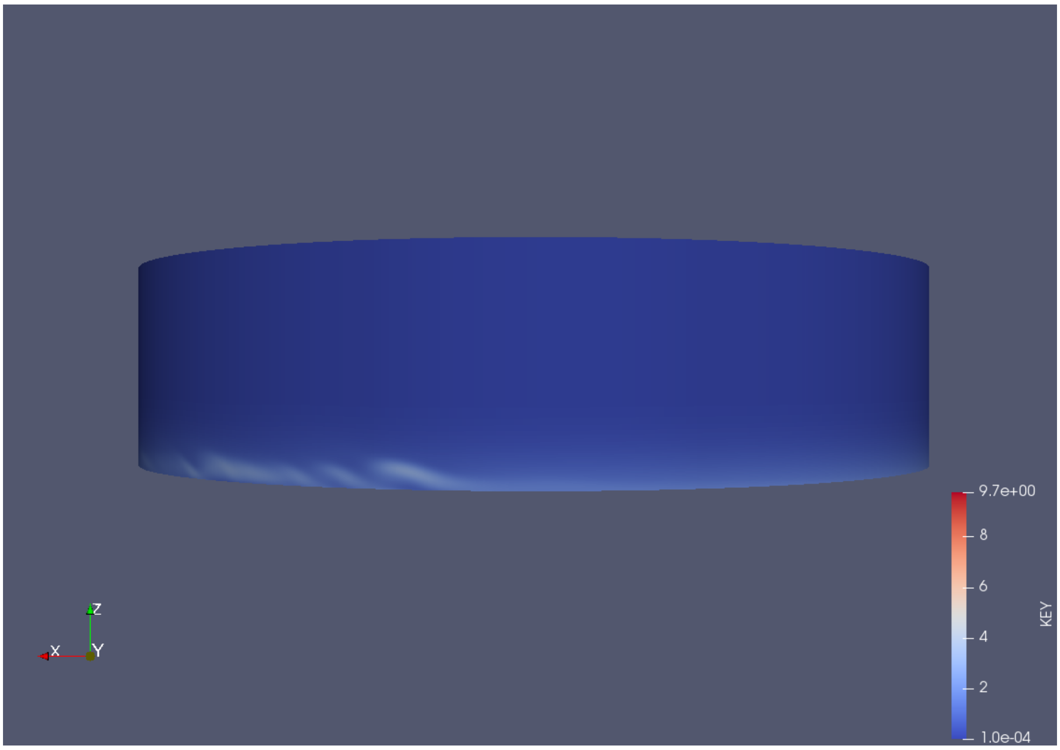

Figure 4.25: Postprocess: TKE (k) field around the ABL for the non-rotated mesh with buffer and 30m cell size

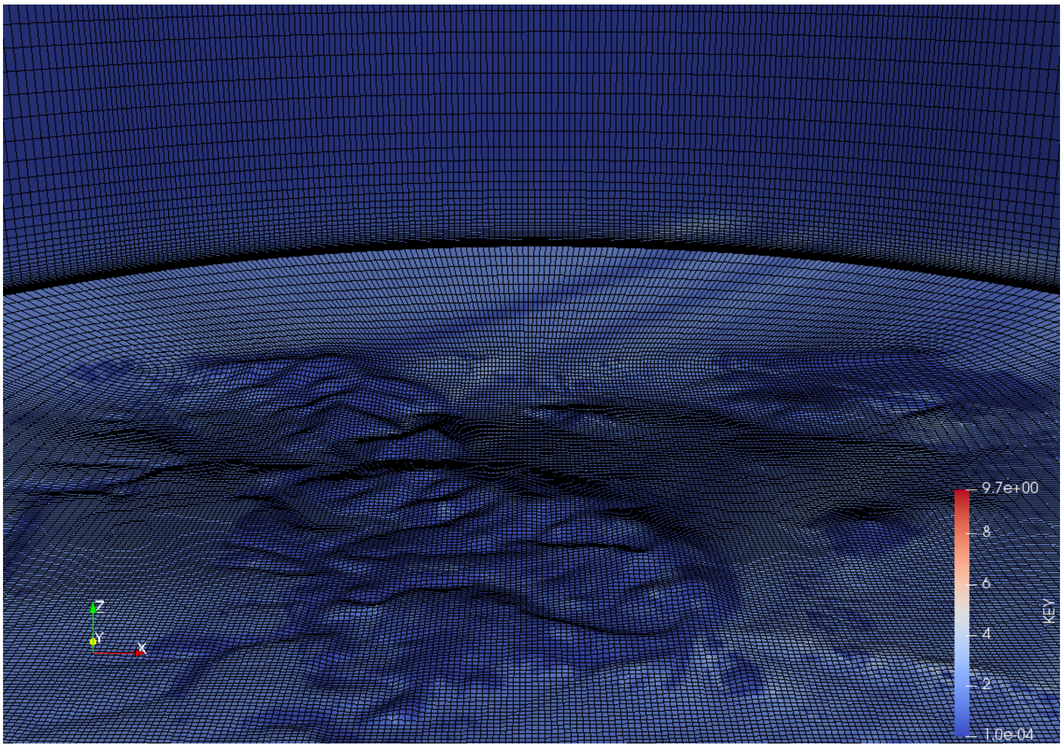

Figure 4.26: Postprocess: TKE (k) at the ground for the non-rotated mesh with buffer and 30m cell size

Figure 4.27: Postprocess: Dissipation rate ε field around the ABL for the non-rotated mesh with buffer and 30m cell size

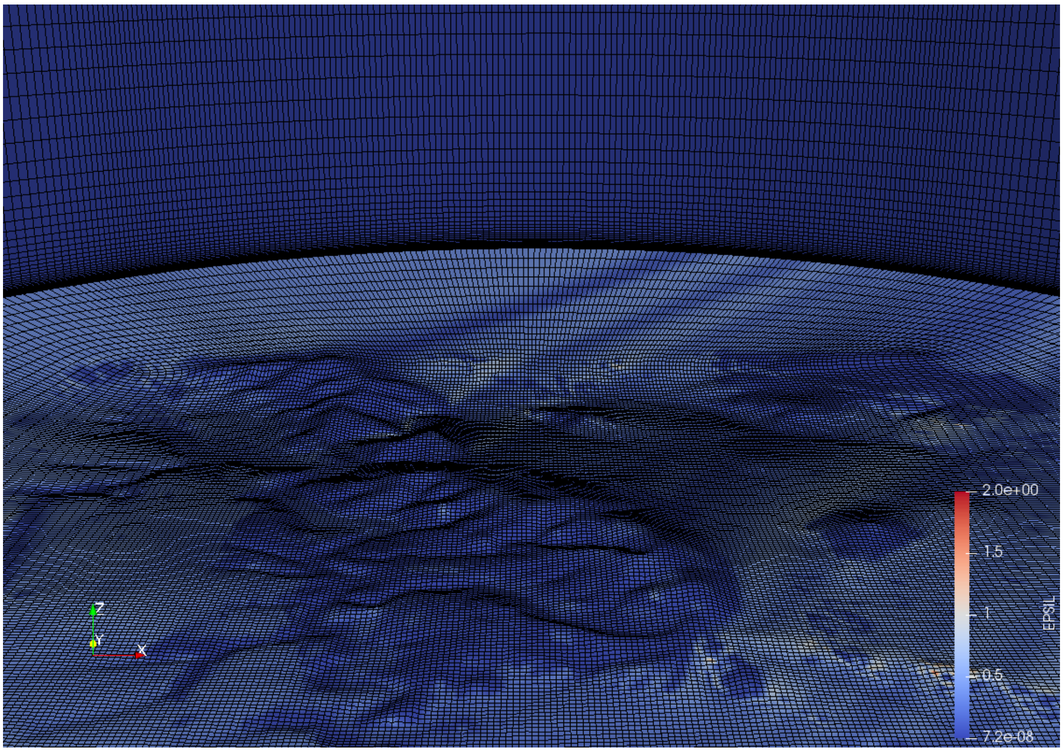

Figure 4.28: Postprocess: Dissipation rate ε at the ground for the non-rotated mesh with buffer and 30m cell size

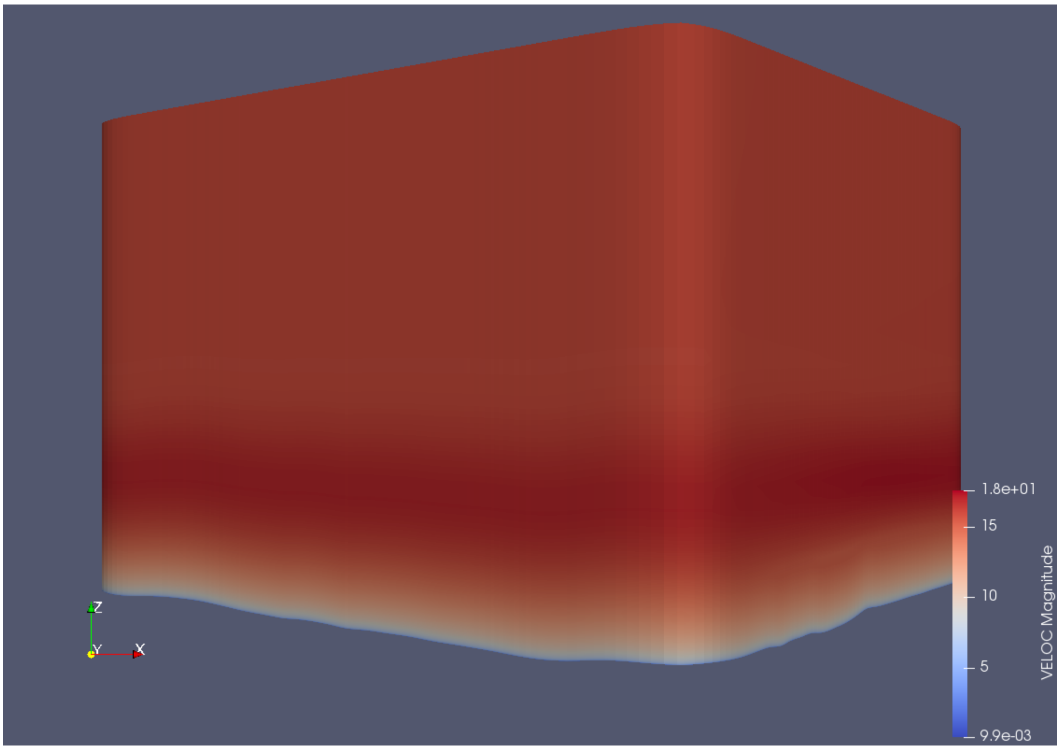

Figure 4.29: Postprocess: Horizontal mean velocity field around the ABL for the rotated mesh without buffer and 30m cell size

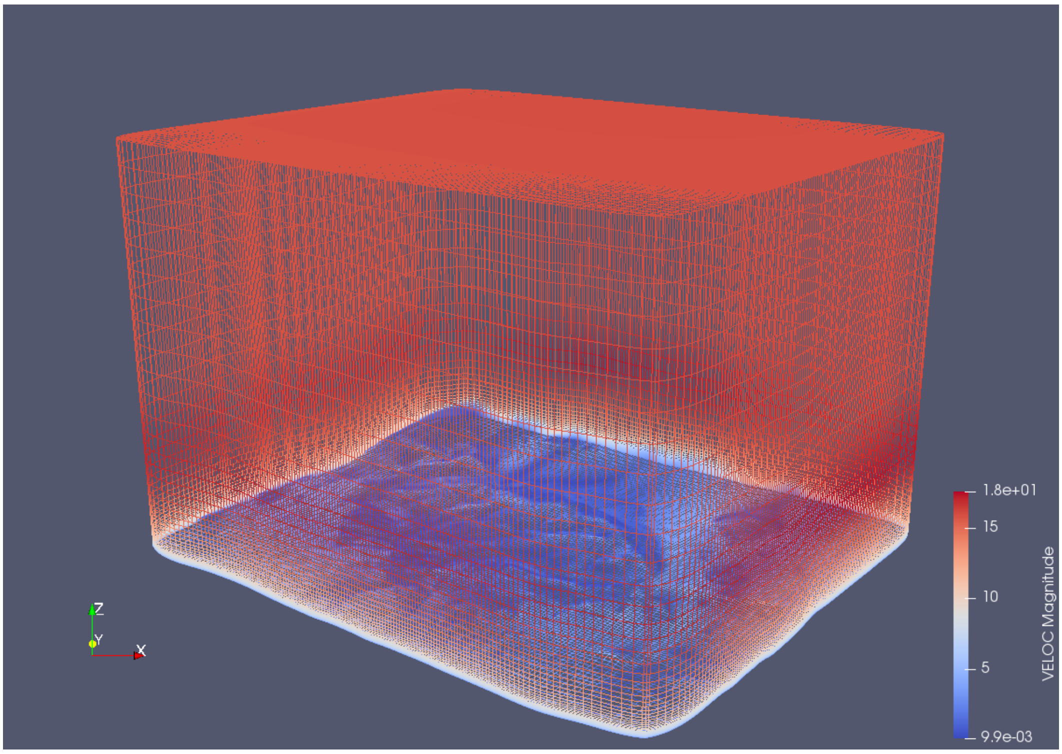

Figure 4.30: Postprocess: Horizontal mean velocity field at the ground for the rotated mesh without buffer and 30m cell size

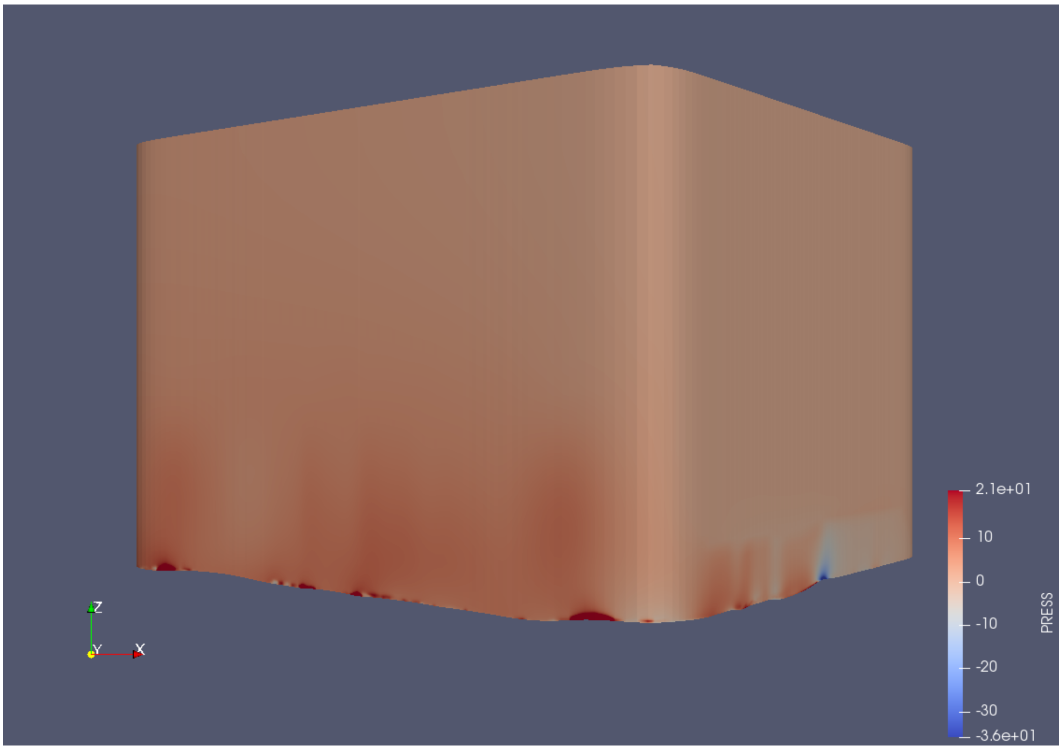

Figure 4.31: Postprocess: pressure field around the ABL for the rotated mesh without buffer and 30m cell size

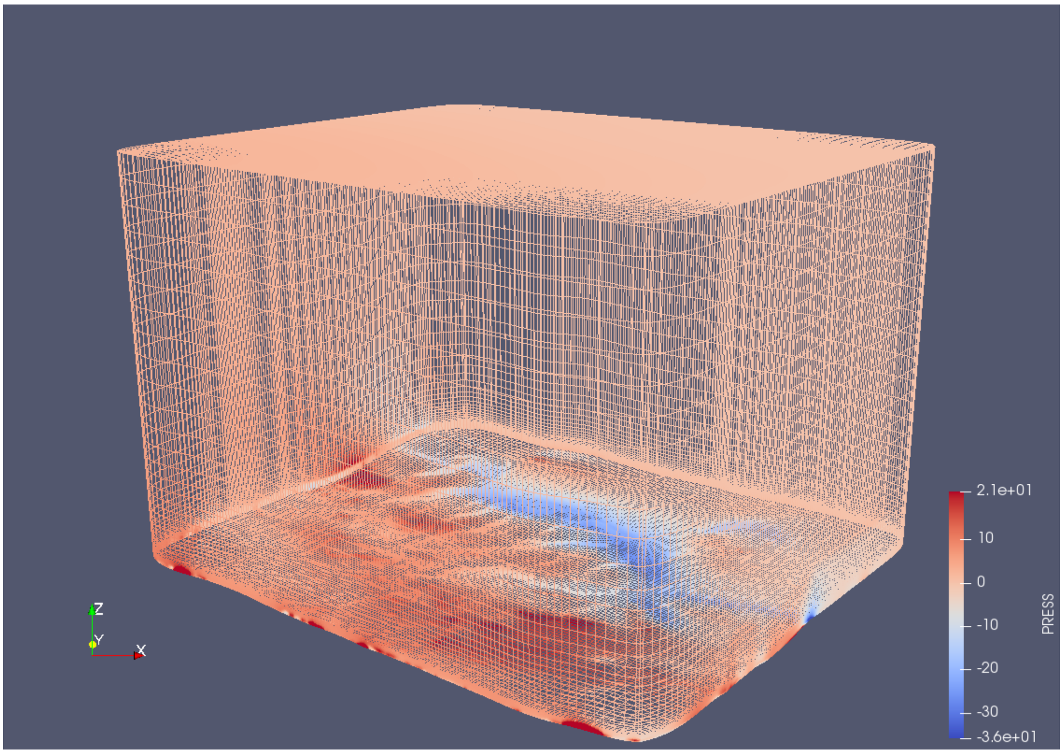

Figure 4.32: Postprocess: pressure field at the ground for the rotated mesh without buffer and 30m cell size

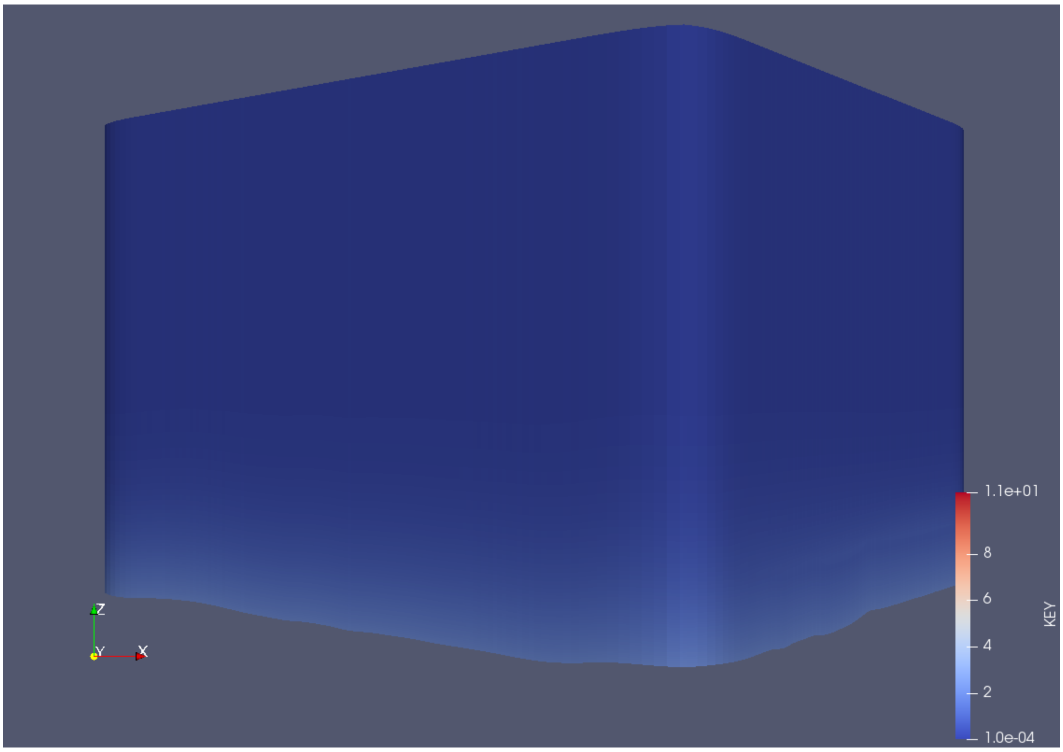

Figure 4.33: Postprocess: TKE (k) field around the ABL for the rotated mesh without buffer and 30m cell size

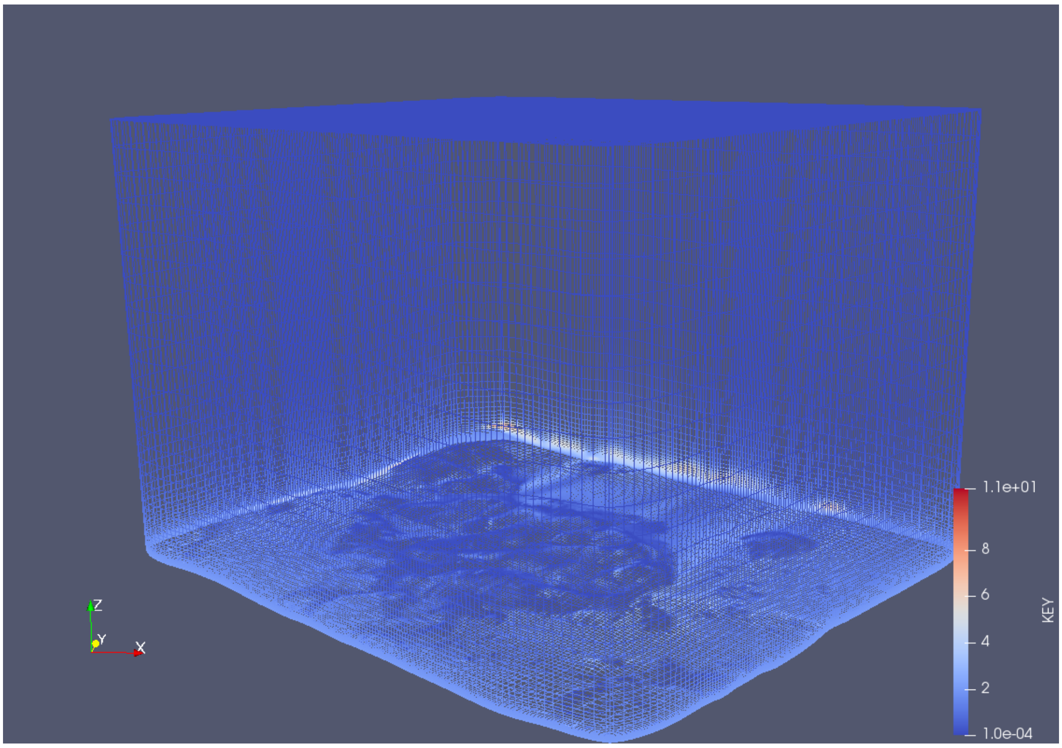

Figure 4.34: Postprocess: TKE (k) field at the ground for the rotated mesh without buffer and 30m cell size

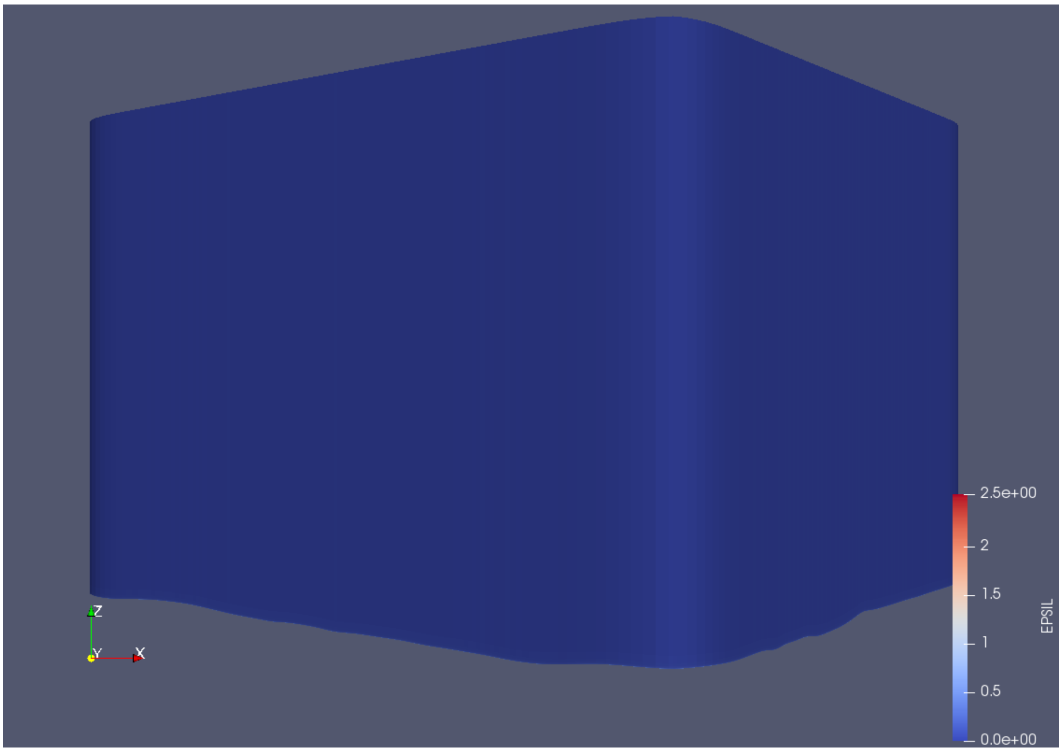

Figure 4.35: Postprocess: Dissipation rate ε field around the ABL for the rotated mesh without buffer and 30m cell size

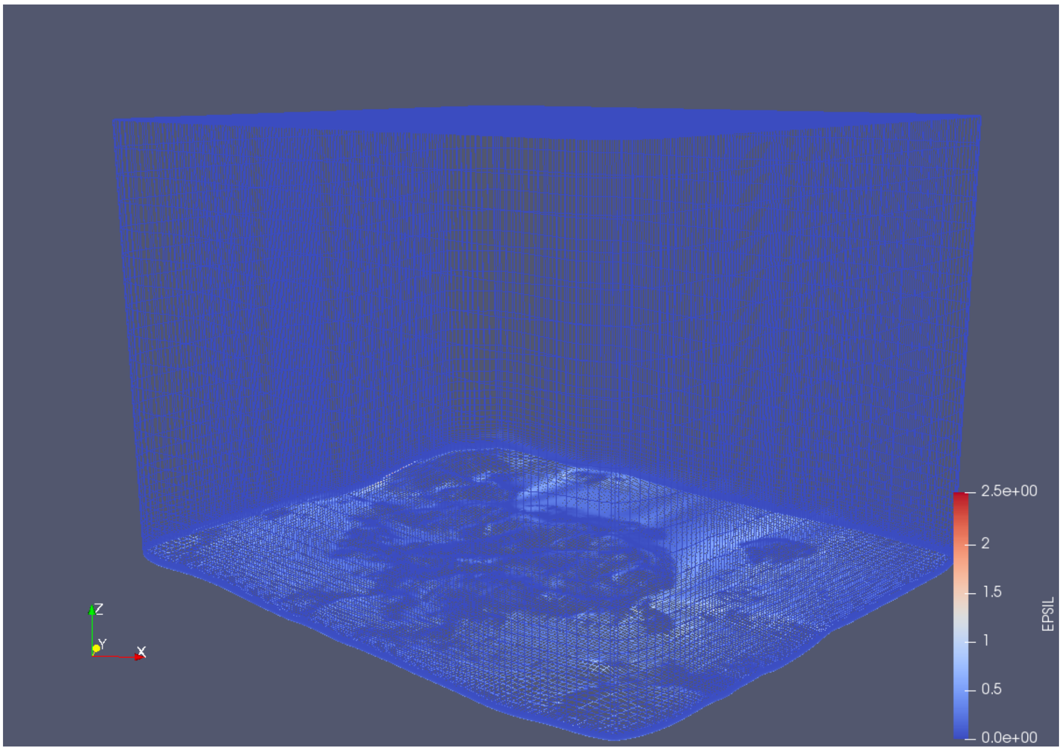

Figure 4.36: Postprocess: Dissipation rate ε field at the ground for the rotated mesh without buffer and 30m cell size

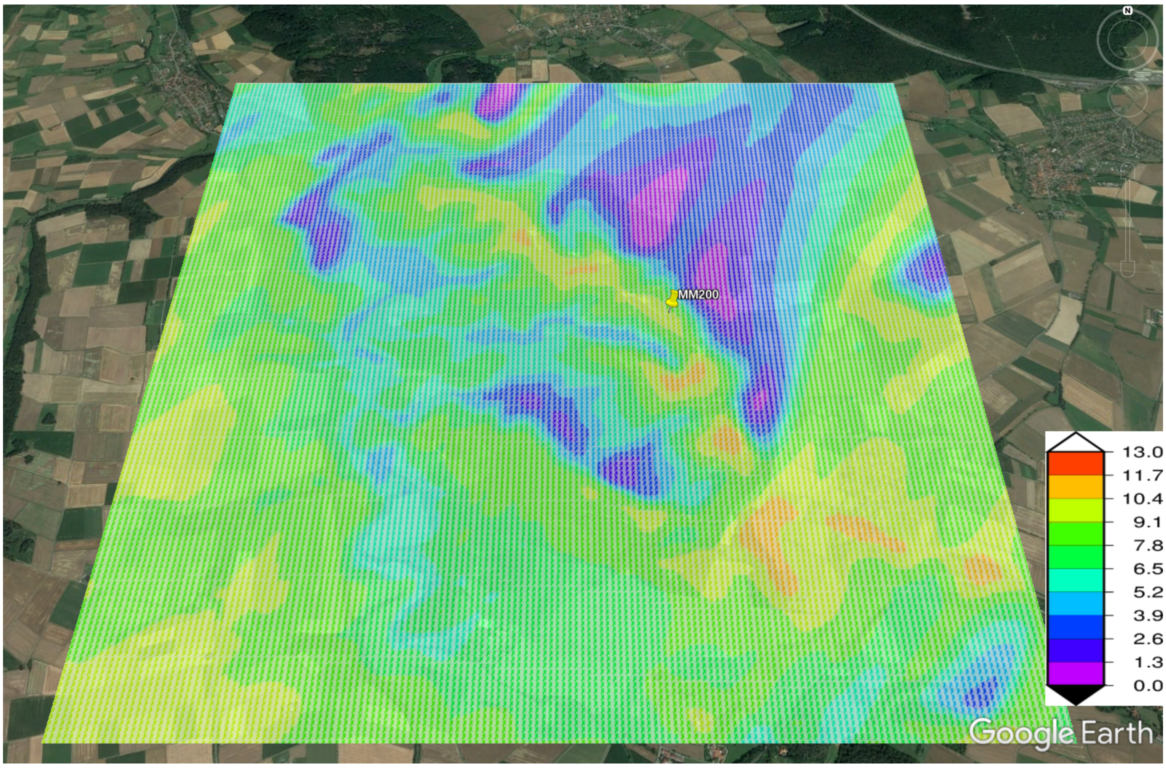

Figure 4.37: Postprocess: Horizontal mean velocity field for the non-rotated mesh at 60 m height w.r.t MM200

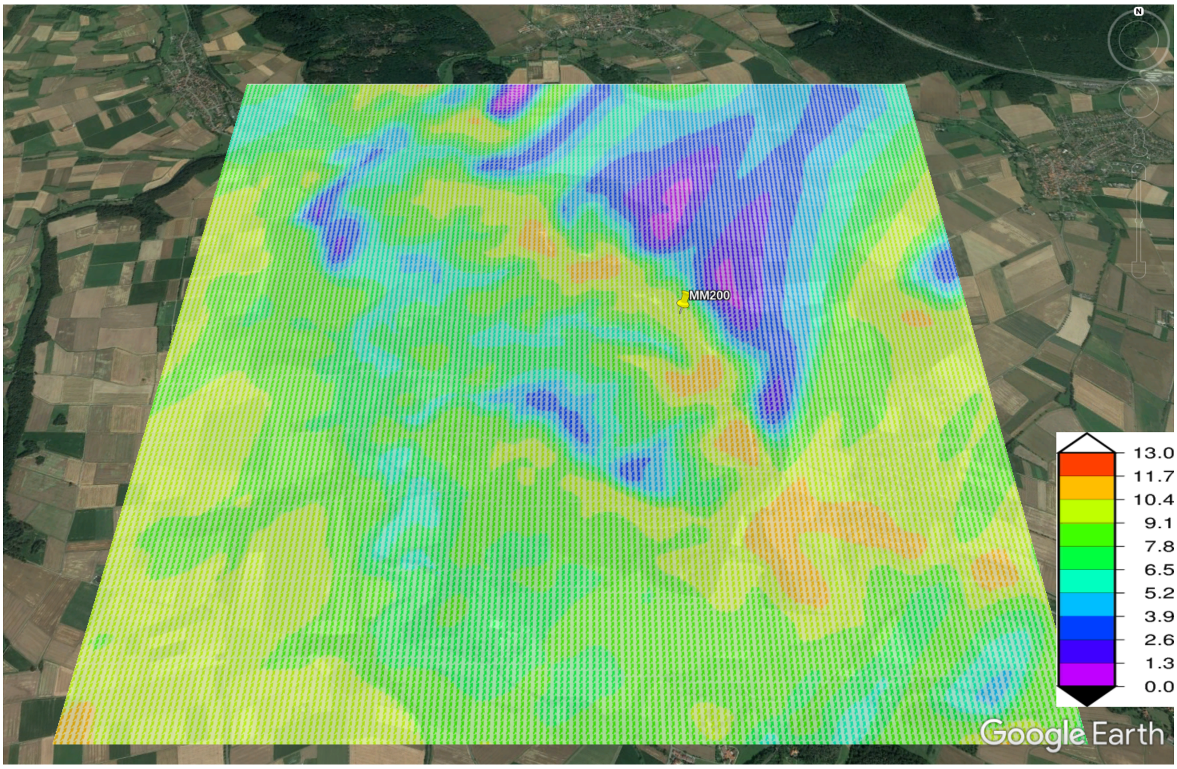

Figure 4.38: Postprocess: Horizontal mean velocity field for the non-rotated mesh at 70 m height w.r.t MM200

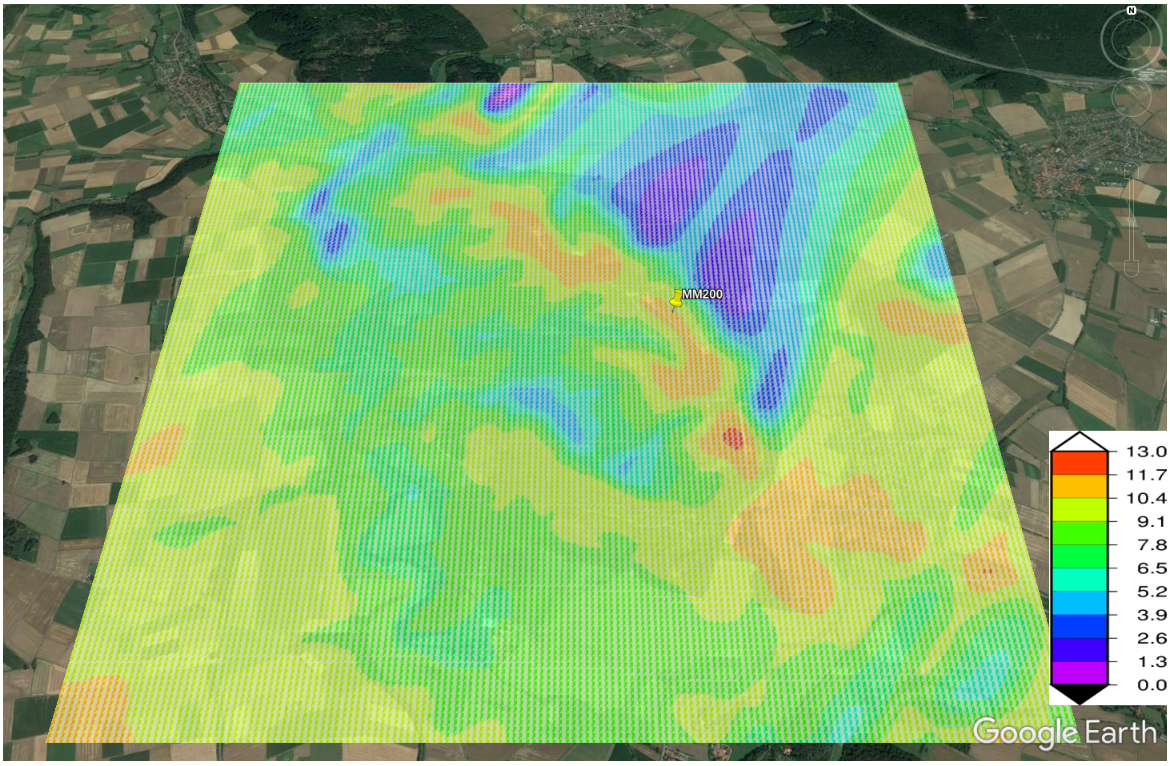

Figure 4.39: Postprocess: Horizontal mean velocity field for the non-rotated mesh at 80 m height w.r.t MM200

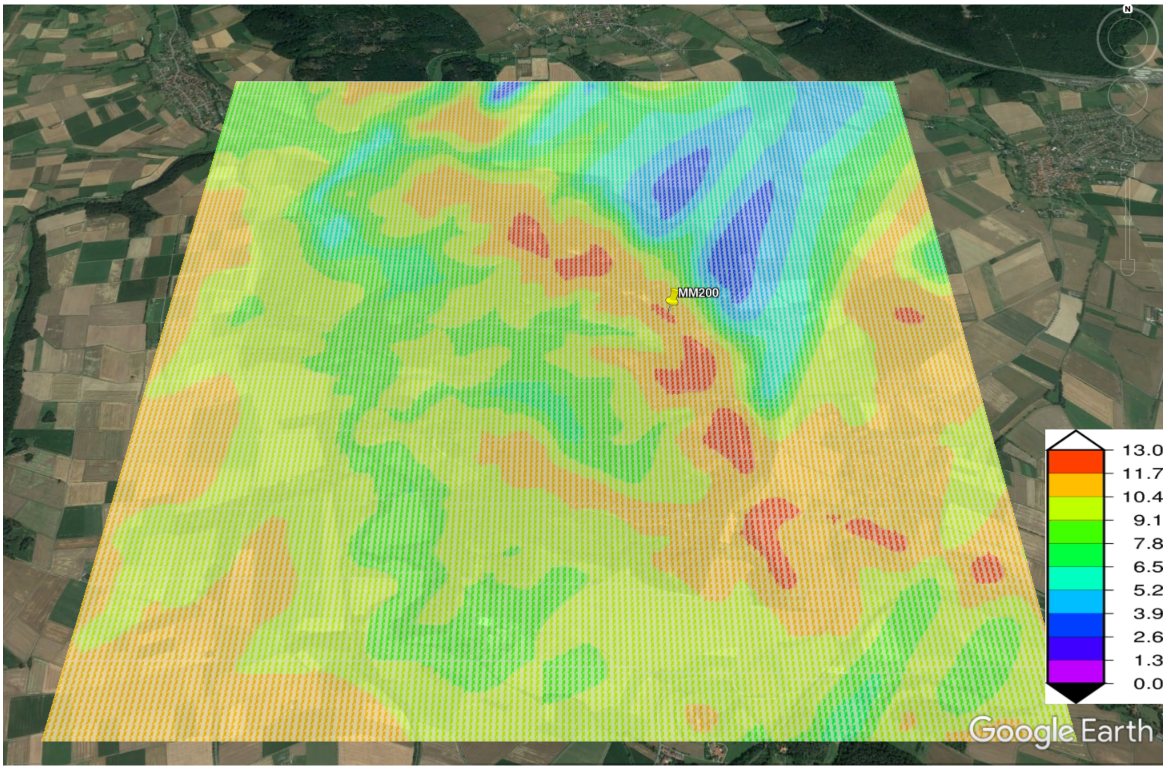

Figure 4.40: Postprocess: Horizontal mean velocity field for the non-rotated mesh at 105 m height w.r.t MM200

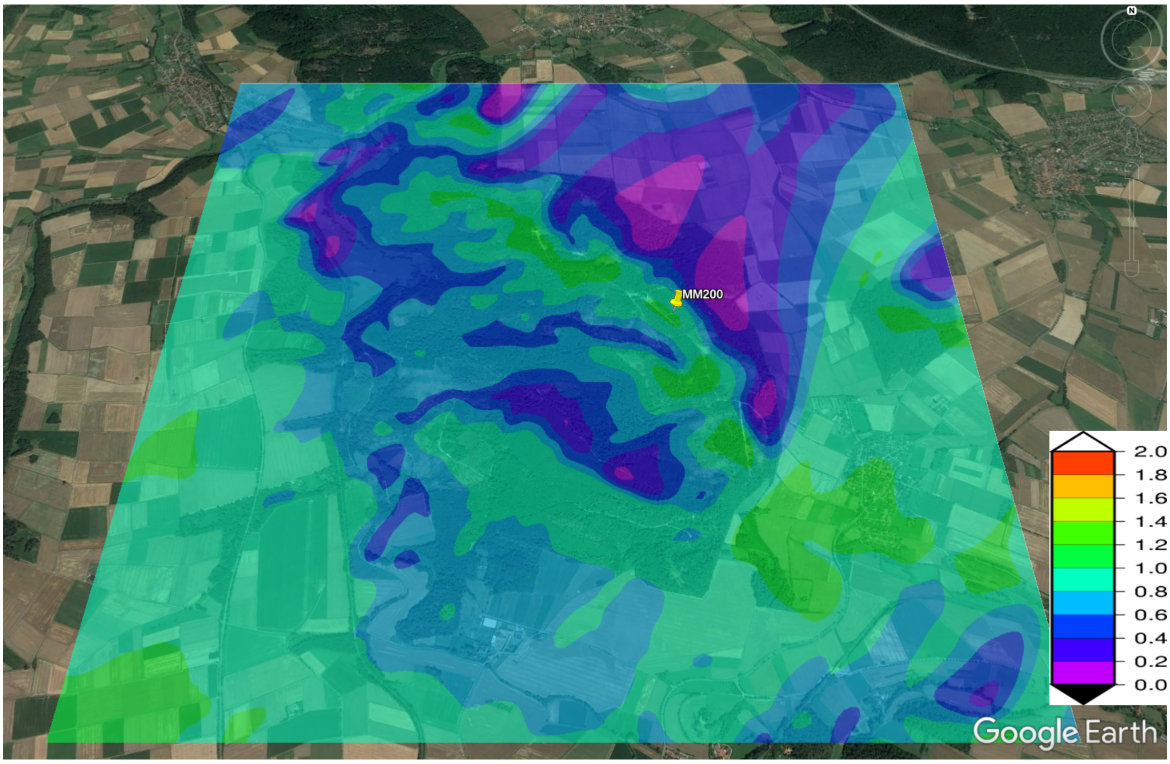

Figure 4.41: Postprocess: Velocity speed-up field for the non-rotated mesh at 60 m height w.r.t MM200

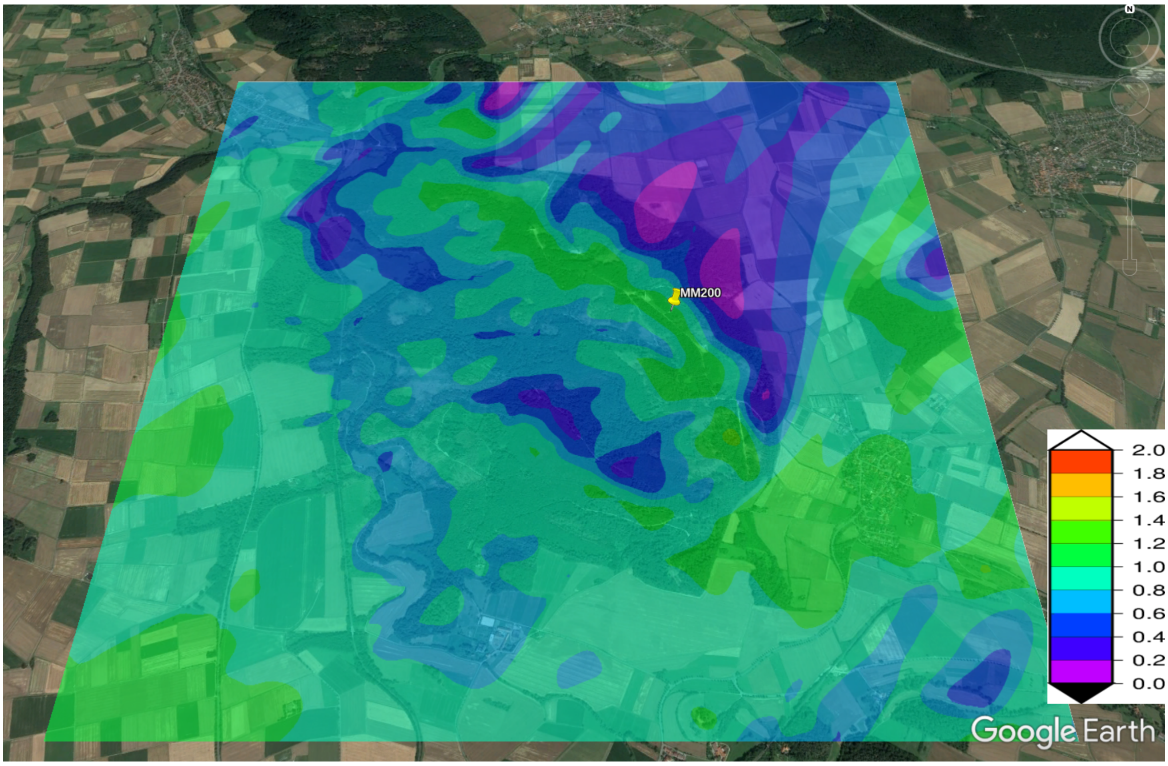

Figure 4.42: Postprocess: Velocity speed-up field for the non-rotated mesh at 70 m height w.r.t MM200

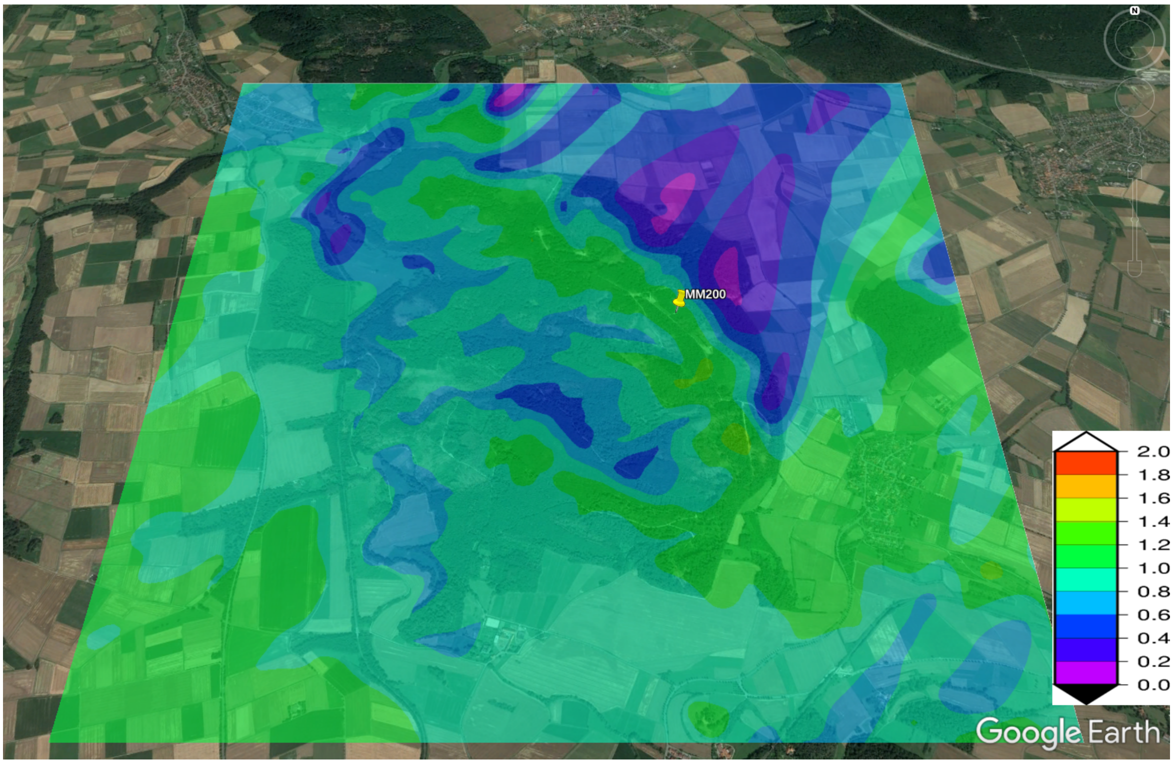

Figure 4.43: Postprocess: Velocity speed-up field for the non-rotated mesh at 80 m height w.r.t MM200

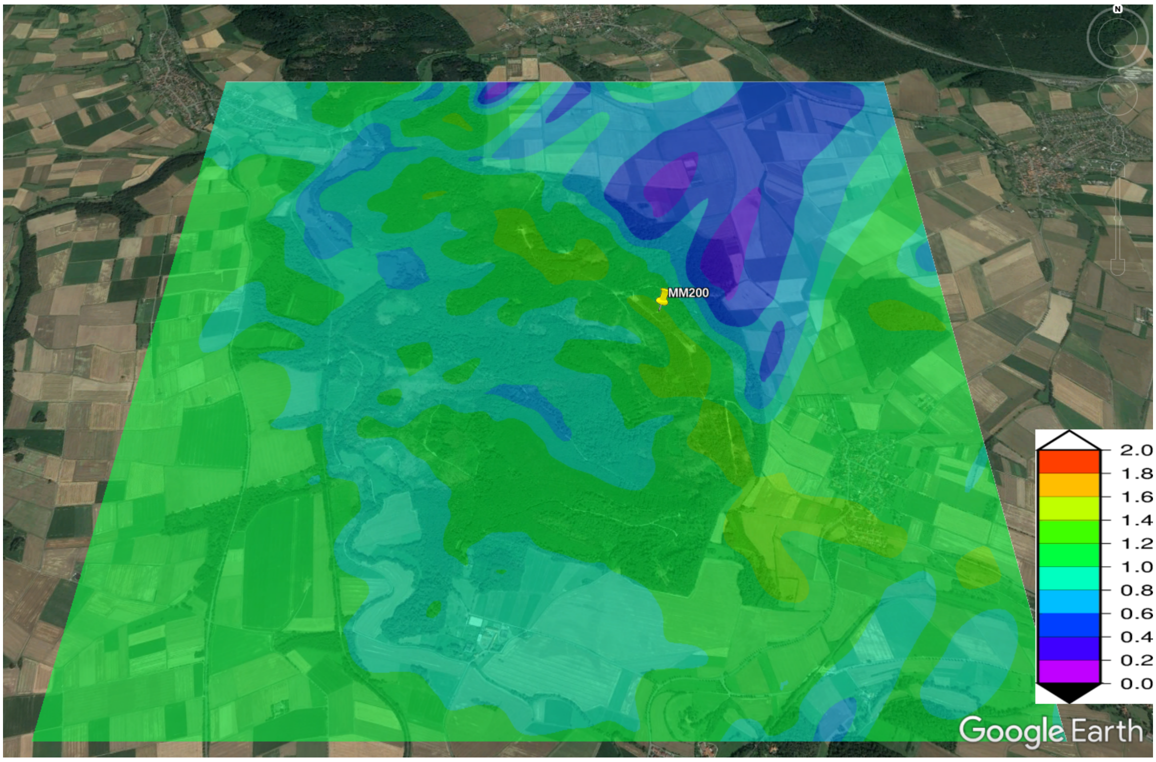

Figure 4.44: Postprocess: Velocity speed-up field for the non-rotated mesh at 105 m height w.r.t MM200

Chapter 5

Power generation

At this point, once the proper cell size of the wind farm area has been determined , the present work aims to simulate, with that optimal cell size (30 m), the same wind flow condition but with the addition of WTs, which are modeled as actuator discs. This chapter articulates in three sections: the first one describes how to choose a WT, its main characteristics and where positioning them; the second section, instead, focuses on the mesh generation process of the wind farm while in the third one the numerical simulation is performed.

5.1 Choice of the WT and positioning

The choice of the WT, as well as its positioning, represents a crucial aspect when designing a wind farm, since the target is to maximize wind energy production. Recalling Eq (2.46)-(2.47), the first consideration to be made, is that power is proportional to the cube of the velocity, therefore the higher the (undisturbed) wind speed U_∞) the greater the power production.
Nevertheless, power is also function of $C_p(U_\infty)$ which does not increase/decrease proportionally with U_∞).
Thus, despite WTs are designed to work at the rated wind speed, in reality the wind speed reference value will be slighlty lower; the reason for this, is due to the fact that, usually, at the rated wind speed, the C_p value (or equivalently the C_t for the thrust force) is not the optimal one.

Thus, when choosing a WT, it is necessary to determine the right trade-off between U_∞) and $C_p(U_\infty)$. In the present case, from Figures 4.37, 4.38, 4.39 and 4.40, it is possible to notice as the area experiencing the highest speed values is definetely the hill.
Furthermore these values increase with the height, reflecting the Horizontal mean wind speed profile behaviour at MM200. This consideration is made by always keeping in mind that the prevailing wind direction is 217° from SW to NE. In particular wind velocities above the hill, at 105 m height w.r.t MM200 (see Figure 4.20), are in between $12 - 13m/s$.
Therefore, on top of these considerations, for this particular case a Vestas V90-3MW has been choosen. Table 5.1 lists its main characteristic, whereas Figure 5.1 and Table 5.2 show respectively its power curve and C_p and C_t values as function of U_∞). From these two figures it is possible to determine the wind speed reference

value, i.e $13m/s$, after which C_p and C_t values start decreasing (see Table 5.2), and the corresponding power which is about $2800kW/s$.

Rated power	3,000.0 kW
Cut-in wind speed	4.0 m/s
Rated wind speed	15.0 m/s
Cut-out wind speed	25.0 m/s
Diameter	90.0 m
Hub height	105 m
Swept Area	6362.0 m^2

Table 5.1: Technical specifications of Vestas V90-3MW [8]

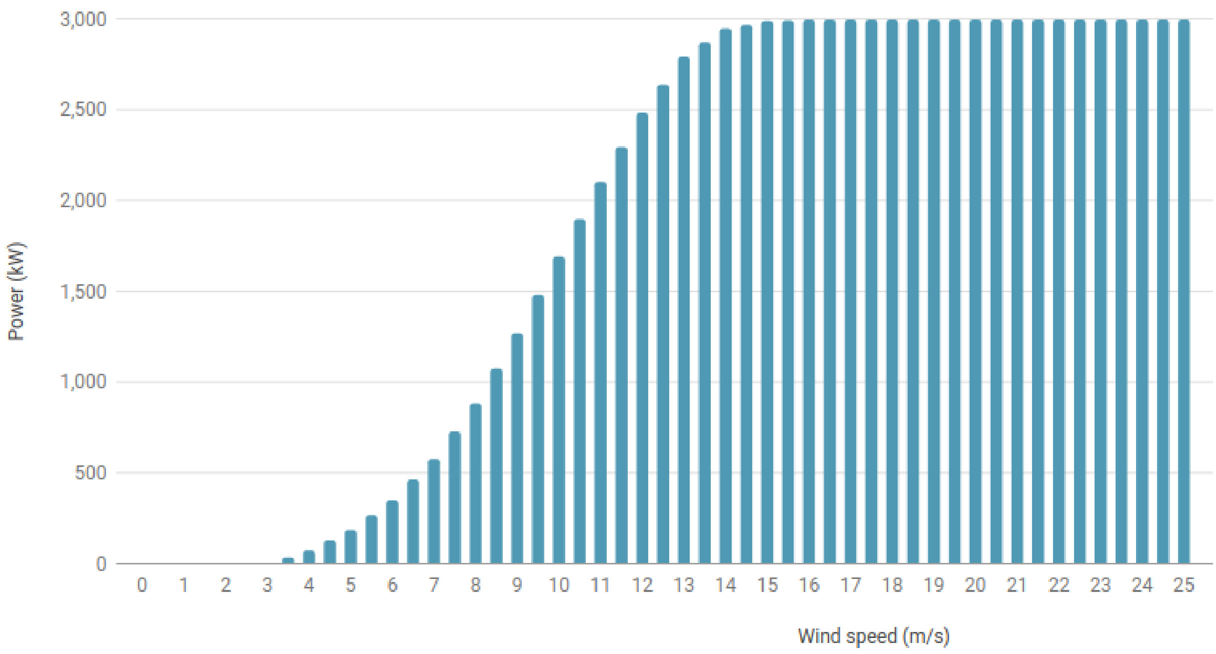

Figure 5.1: Power curve of Vestas V90-3MW [7]

Wind Speed U_∞ [m/s]	C_t	C_p
4	0.912	0.309
5	0.879	0.39
6	0.852	0.419
7	0.851	0.435
8	0.830	0.444
9	0.810	0.448
10	0.739	0.439
11	0.660	0.414
12	0.578	0.378
13	0.489	0.331
14	0.407	0.277
15	0.327	0.228
16	0.263	0.188
17	0.217	0.157
18	0.181	0.132
19	0.154	0.112
20	0.132	0.096
21	0.114	0.083
22	0.100	0.072
23	0.088	0.063
24	0.078	0.056
25	0.070	0.049

Table 5.2: C_t and C_p values as function of U_∞

# WT	X_{coord}	Y_{coord}
WT1	513762.00 m	5689921.00 m
WT2	513440.00 m	5690294.00 m
WT3	513045.00 m	5690650.00 m
WT4	512760.00 m	5690841.00 m

Table 5.3: WTs locations

So in the end four Vestas V90-3MW will be positioned on the hill (see Table 5.3), facing the inflow prevailing wind direction and at a distance equal or greater than 5 times the diameter of the WT.

5.2 Mesh generation of the wind farm: discs insertion

Recalling the background non-rotated volume mesh generated in section 3.2 (with the buffer and 30 m cell size), the mesher modifies it to obtain a new mesh adapted to the WTs. The actuator discs, used to simulate WTs, are characterized by the same diameter value and by a width which is set to the 6% of the diameter itself (i.e 5.4 m). The Alya mesher, also in this case is quite robust and automatic, and for this particular task it requires only few additional input data related to the WTs characteristics, such as location, diameter and hub height, and, as input mesh parameter, the cell size value that will be used to discretize the actuator discs (set to 10%D, i.e 9 m).
The meshing procedure, which was used by considering four Vestas V90-3MW, articulates in four main steps:

1. Empty the area surrounding the WTs.
   Knowing the location of the turbines, the mesher a priori calculates the region that will cover the adapted mesh for each disc and detects and removes the hexahedra that intersect this region[6]. Figure 5.1 shows the region of elements to be removed from the ABL mesh.

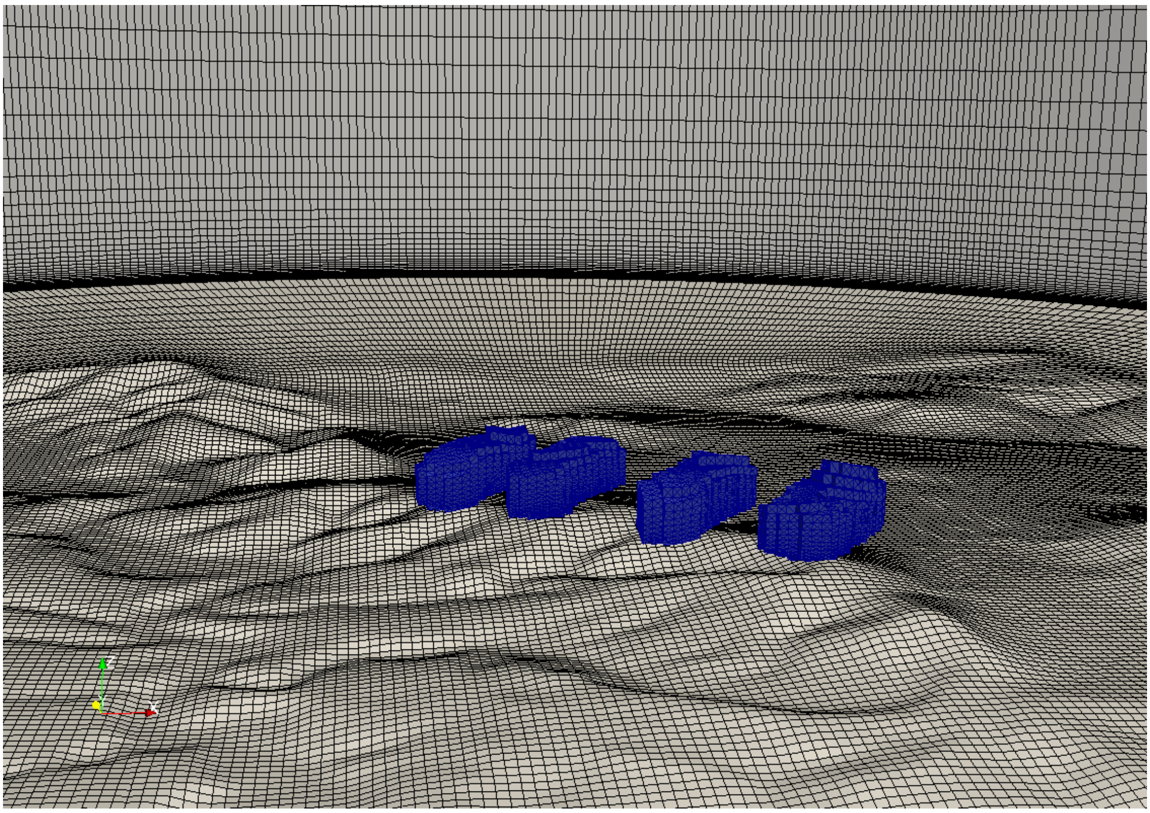

Figure 5.2: Mesh generation of the wind farm: ABL volume mesh and regions to be removed

2. Generate an adapted mesh to the actuator discs.
   To generate the disc meshes, the program first meshes with the desired cell size a planar disc having the diameter of the wind turbine using a quadrilateral mesh. Next, it generates a volume mesh by extruding the 2D quadrilateral mesh with the desired number of layers (one single layer of hexahedra by default) and inserts the disc at the hub height with an orientation perpendicular to the wind inflow direction[6]. The normal direction to the WTs is estimated performing a precursor simulation using only the ABL volume mesh without WTs (from Chapter 4). At this point, the (background) ABL mesh and the mesh surrounding each disc are disconnected.

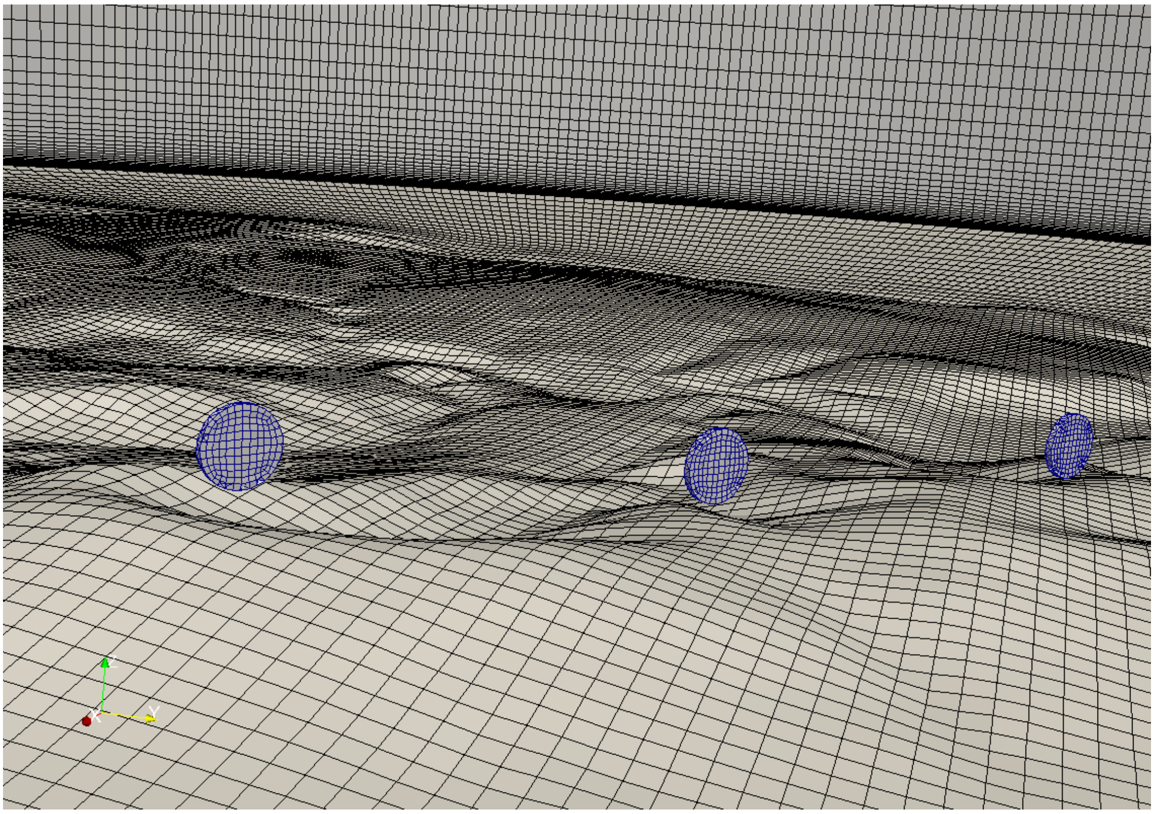

Figure 5.3: Mesh generation of the wind farm: disc generation and meshing

Furthermore, it is important to remind that, in order to capture the wake

effects induced by the WTs, the final mesh has to modified and refined with a higher resolution radially, upstream and downstream of WTs (w.r.t the outer one).
Thus, the following step consists in generating the mesh surrounding WT ensuring the correct mesh sizing transition so as to match the different scales of the ABL volume and disc meshes. In the disc radial, downstream and upwind direction, the growing factor was set to 1.05. Other mesh parameters, instead, such as the tetrahedral size or the extension of the refined region around each WT are automatically determined by the mesher.

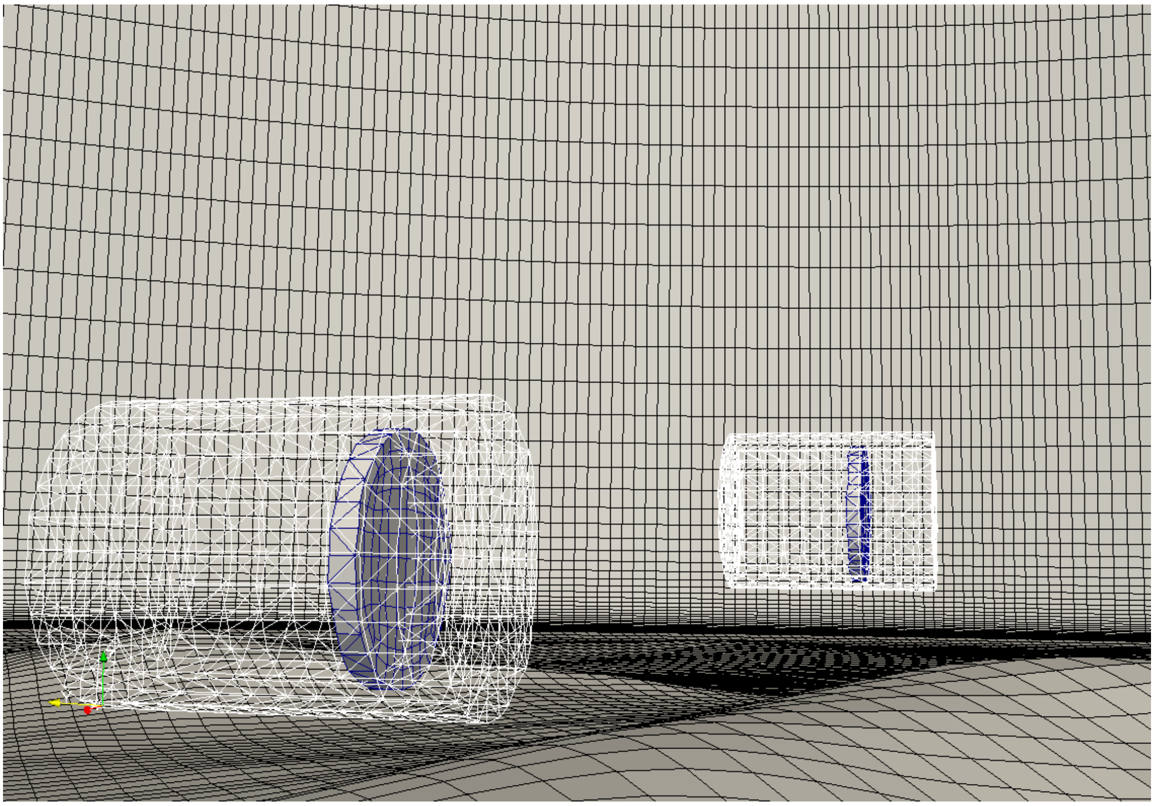

Figure 5.4: Mesh generation of the wind farm: upwind/downstream disc mesh

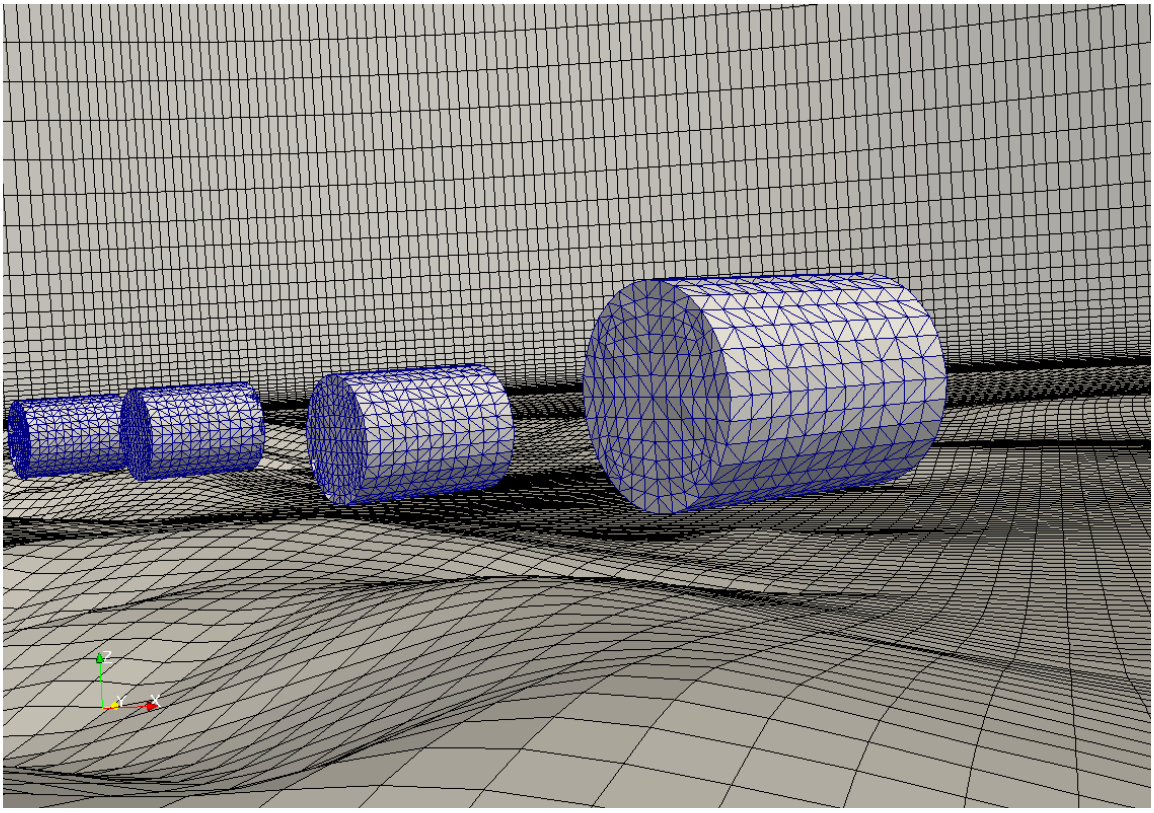

Figure 5.5: Mesh generation of the wind farm: upwind/downstream disc mesh

3. Conform the ABL volume and adapted actuator disc meshes.
   This step consists in splitting the hexahedra between the two hexahedral meshes, i.e the ABL volume and discs one, into tetrahedra and pyramids so as to create a conformal connection between the two meshes. The resulting mesh is a hex-dominant hybrid mesh. This is done in order to provide smooth element size transitions across scales so as to avoid extending the higher resolution zone around the discs, all over the domain, that would lead to an unnecessarily increase in the number of computational cells.

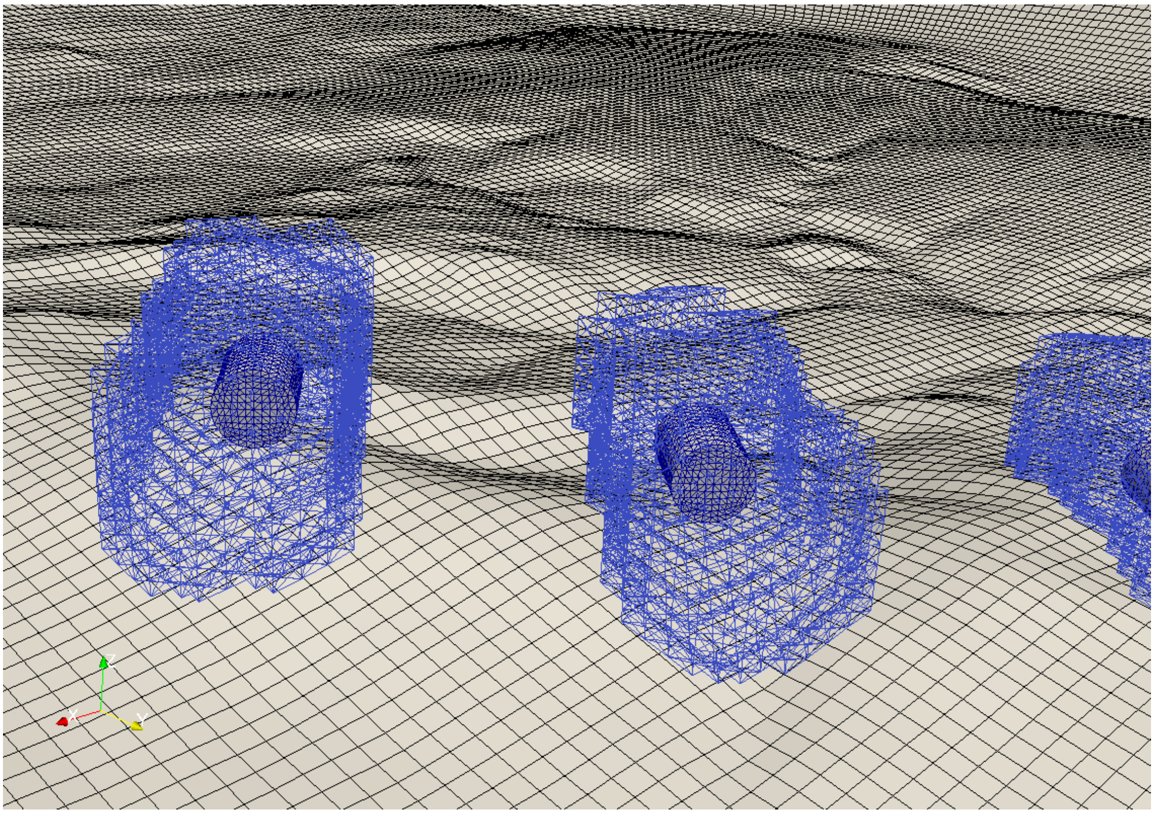

Figure 5.6: Mesh generation of the wind farm: splitting upwind/downstream mesh

4. Optimizing hybrid mesh.
   The resulting mesh comes out to be highly constrained since it discretizes the topography, resolves the ABL and is conformal with the actuator discs. For this reason, as done previously with the other meshes (surface and volume ones), it is fundamental to determine the quality of the mesh itself and if necessary, optimize it. The procedure to determine the quality is the same discussed before and consists in defining the corresponding ideal element for each element of the mesh. The ideal elements corresponding to the hexahedra of the ABL mesh have already been set automatically by the mesher in the previous meshing steps; instead, for what concerns the ones related to the new hexahedra around the disc, tetrahedra and pyramids, they are set at this stage. Once the mesher has defined the ideals of all the elements, it optimizes the final mesh.

Mesh	#elements	Min. quality	Max. quality	Mean quality	Standard deviation
Hybrid	2723400	0.65	1.00	0.95	0.04
Hexahedra	2529563	0.68	1.00	0.96	0.03
Tetrahedra	171793	0.65	1.00	0.8	0.10
Pyramids	22044	0.70	1.00	0.97	0.03

Table 5.4: Statistics of the final hybrid mesh

Table 5.4 shows the statistics of the final hybrid mesh. The total number of elements in this mesh (2723400) is higher than the one computed before (2605700), without WTs (see Table 3.1, second line). This slight difference is basically due to the discs insertion.
Besides, the minimum quality of the final mesh (hybrid mesh) further decreases compared to the previous background mesh (hexahedral mesh without WT); this is due to the additional constraints applied to the mesh; in fact, the resulting mesh must not only discretize the topography and resolve the ABL, but it must also be conform with the actuator discs. Finally, the total time needed to insert discs is 13.195 s (0.220 min) whereas the one necessary to perform optimization is 4.333 s (0.072 min).

5.3 Numerical simulation with WTs

5.3.1 Results

# WT	C_t	C_p	U_∞ [m/s]	U_{hub} [m/s]	$U_{av.}$ [m/s]	P [kW]
WT1	0.5369	0.3563	12.4616	10.4702	10.4076	2678.2251
WT2	0.5233	0.3491	12.6148	10.5884	10.6013	2722.0774
WT3	0.5651	0.3712	12.1452	10.0217	10.0095	2582.8275
WT4	0.5352	0.3554	12.4809	10.4651	10.4319	2683.8315

Table 5.5: Numerical results at the four Vestas V90-3MW

Table 5.5 lists numerical results for each turbine; $U_{av.}$ is indicating the average velocity along the whole rotor diameter, whereas P is the power generated by each wind turbine; then by summing up all those four values, it is possible to determine the total power generated by the wind farm, that is 10666.615 kW whereas the total nominal one is 12000 kW; this means that the wind farm, in this particular condition, is working at about the 90% of the nominal one, which represents a very good result.

5.3.2 Convergence analysis

Figure 5.7 shows the convergence trend of both momentum and continuity for the final mesh, i.e the one with WTs. Despite the addition of the disc force term, the two trend does not show huge differences compared to the two in Figure 4.17. Figure 5.8, instead, displays, for the same mesh, the convergence trend of both k and dissipation ε equation; in this case, comparing these two with the ones in Figures 4.18, it can be noted that the number of solver iterations required to achieve the steady-state solution is higher making the iteration slightly more complex. This is basically due to the wake effects induced by WTs.

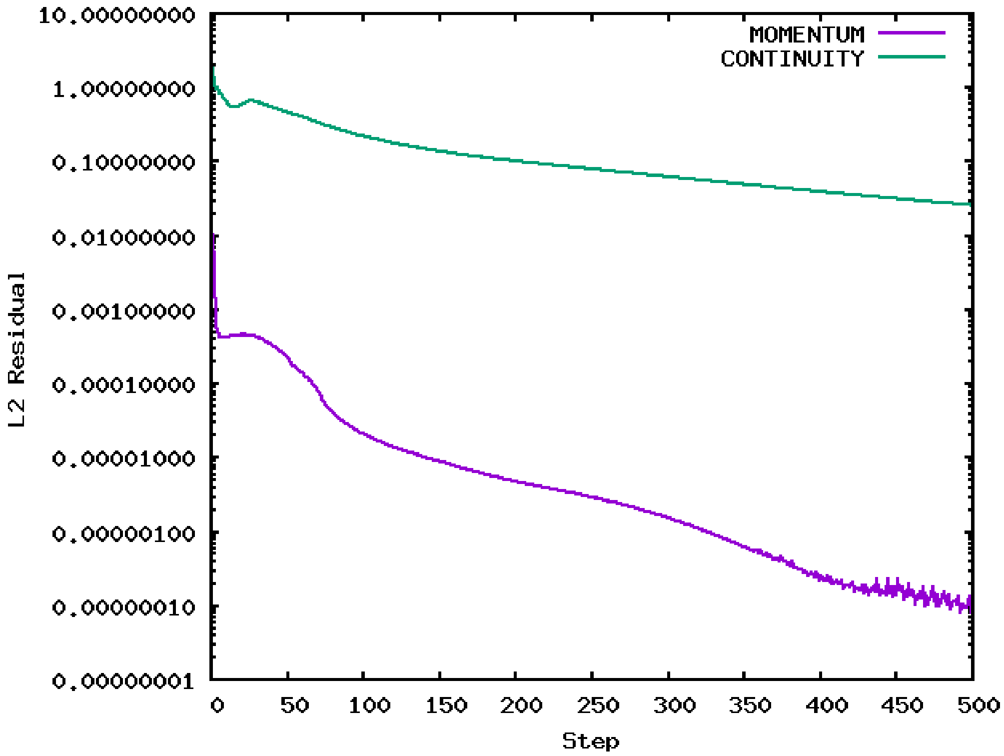

Figure 5.7: Convergence trend of both momentum and continuity equation for the final hybrid mesh

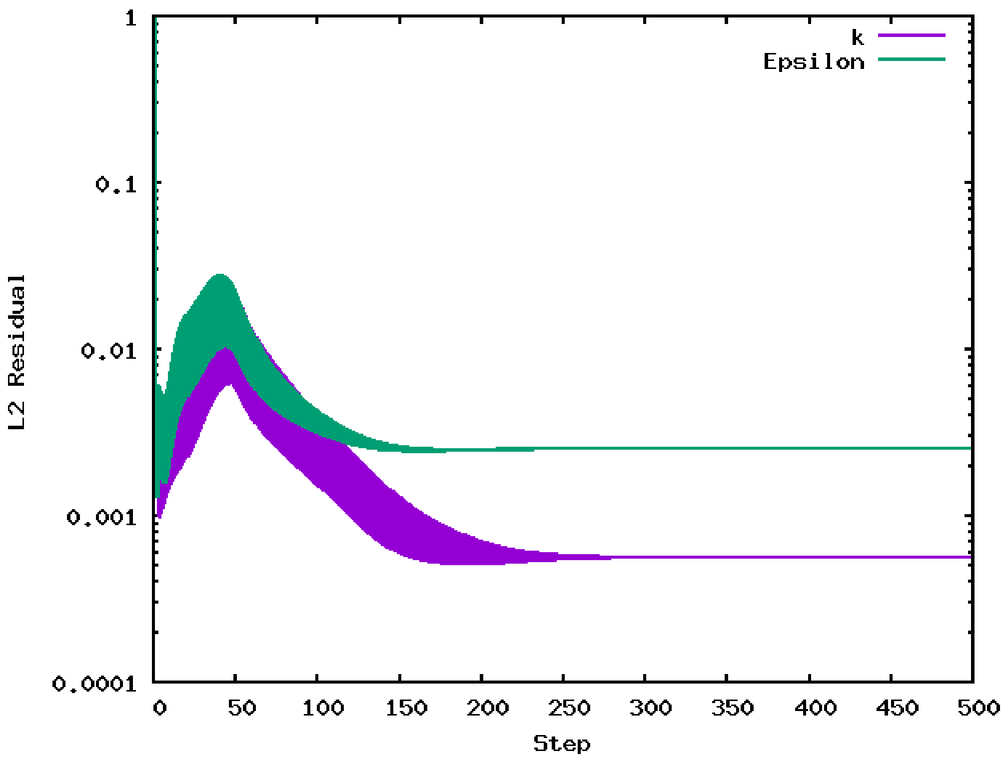

Figure 5.8: Convergence trend of both k and dissipation ε equation for the final hybrid mesh

5.3.3 Postprocess

Figure 5.9, compared to Figure 4.40, shows how the horizontal mean velocity field modifies when inserting WTs; the same, clearly, occurs for the velocity speed-up field (see Figure 5.10 and 4.44). Looking more closely, it is possible to visualise the wake effects downstream of WTs, such as the expanding wake area and the velocity deficit downstream of the WTs.

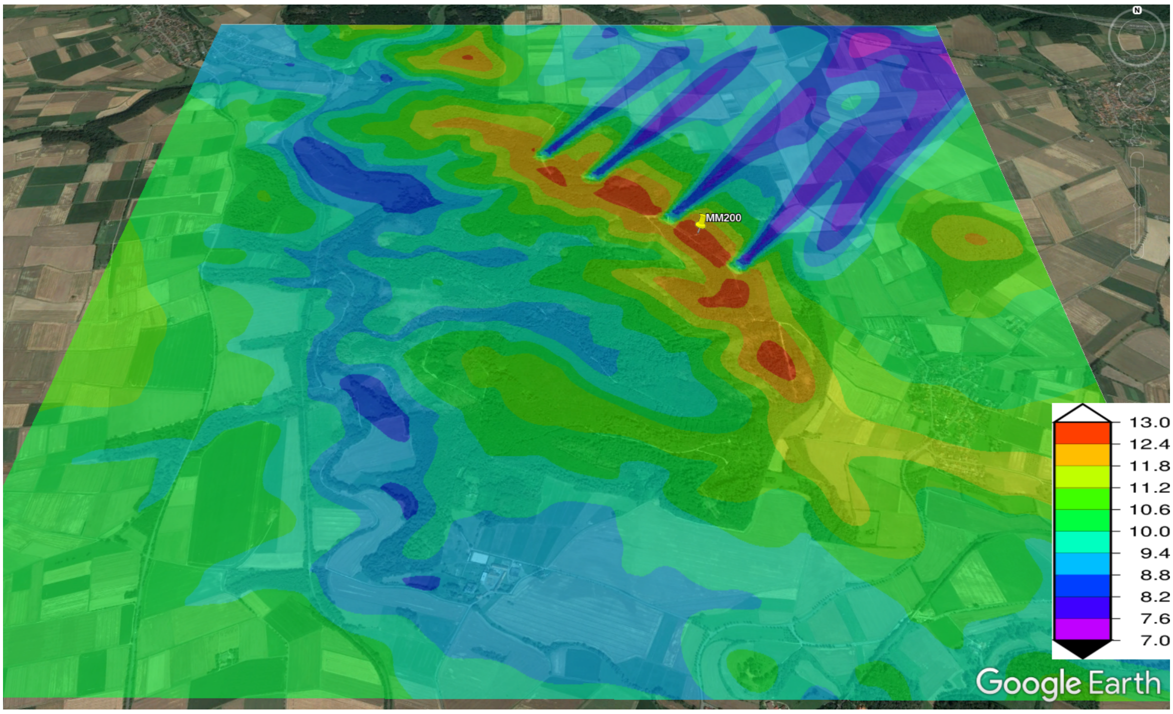

Figure 5.9: Postprocess: Horizontal mean velocity field (modulus only) for the final hybrid mesh at 105 m (hub height) w.r.t MM200

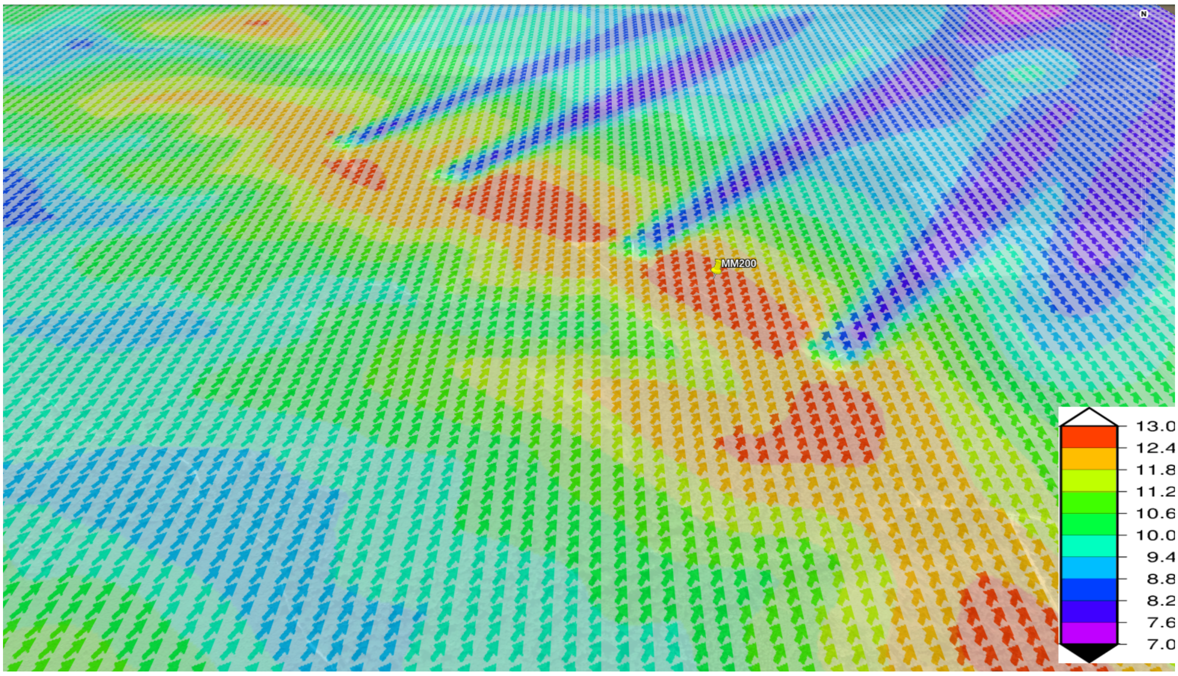

Figure 5.10: Postprocess: Horizontal mean velocity field (vectors) for the final hybrid mesh at 105 m (hub height) w.r.t MM200

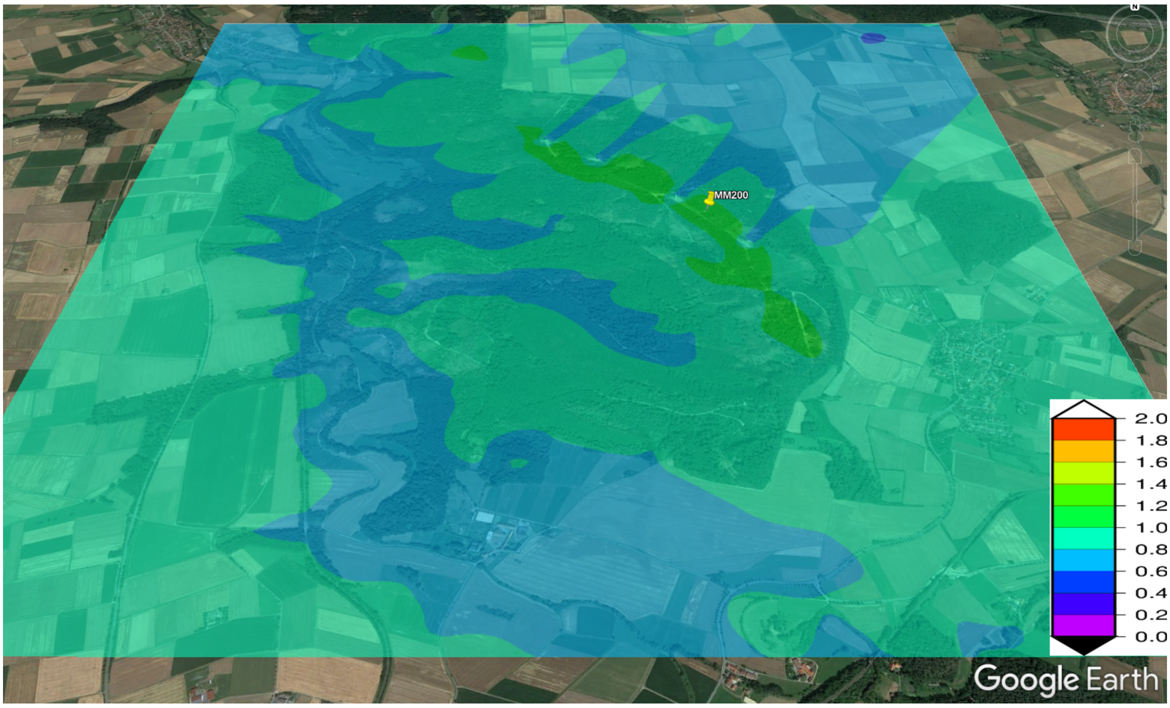

Figure 5.11: Postprocess: Velocity speed-up field for the final hybrid mesh at 105 m (hub height) w.r.t MM200

Chapter 6

Conclusions

In this work, developed by means of Alya, several windflow simulations of a neutral ABL have been performed over the forested and complex Rödeser Berg site, by testing different mesh resolutions and evaluating the impact of the buffer. The former does not affect either mesh quality or numerical results to a great extent, since the numerical errors, for wind speed and direction, between the four tested mesh cell sizes, keep always below 2.15% except when dealing with the greatest mesh cell size (60m), where they rise up to 4.2%; the latter instead accounts to a major effect, leading to a strong reduction of the mesh quality and consequently to higher numerical errors up to 7.3%.

Therefore, despite the complexity of the site, Alya mesher results to be quite robust, providing high-quality meshes, even when the buffer is considered. In parallel also the computational time for each tested case has been evaluated so as to find the right compromise between computational cost and numerical accuracy. For this reason 30 m has been choosen as the optimal horizontal mesh resolution.

In addition this thesis evaluates the effect induced by the forest on wind profiles and describes how to define the ABL and the importance of the Coriolis force.
At this point, once the correct mesh cell size has been selected, a further simulation is performed but with the addition of WTs, modeled as actuator discs and discretized with a very fine mesh (9 m), so as to evaluate the performance of the wind farm, in terms of generated power; this one comes out to be equal to about the 90% of the total nominal power, which represents a fairly good result.

Also the Alya solver, as well as the Alya mesher, comes out to be quite consistent, since in all the tested cases both RANS and turbulence equations reach convergence. Finally the wake effects and their related features are analyzed through the post-process showing in particular the velocity speed deficit downstream of WTs.

Bibliography

[1] BWE: Bundesverband Wind Energy, www.wind-energie.de,
URL: `https://www.wind-energie.de/english/statistics/international-statistics/`

[2] UKA GROUP, www.uka-gruppe.de,
URL: `https://www.uka-gruppe.de/en/citizens-and-communities/operating-principle-of-a-wind-turbine/`

[3] Julie Kay Lundquist and Andrew Clifton. *"How turbulence can impact power performance"*. North American Windpower, September 2012.
URL: `https://www.wind-watch.org/documents/how-turbulence-can-impact-power-performance/`

[4] Martin Dörenkämper, Tobias Klaas, Paul Kühn, Björn Witha, Bernhard Stoevesandt, *"NEWA Rödeser Berg 2017 - Blind Test -"*, 20171220-NEWA-KS-Benchmarks-Kickoff-DoeMar,
URL: `https://windbench.net/newa-r-deser-berg-2017-blind-test`

[5] Alexander Basse et al. , *"Experiment documentation, NEWA FORESTED HILL EXPERIMENT"*, technical report IWES-KS-2017-214-V1.pdf,
URL: `https://windbench.net/newa-r-deser-berg-2017-blind-test`,
URL: `https://b2drop.eudat.eu/s/JXOpzmsOkHwSfTB`

[6] Abel Gargallo-Peiró et al. , *"Mesh generation, sizing and convergence for onshore and offshore wind farm Atmospheric Boundary Layer flow simulation with actuator discs"*, in Journal of Computational Physics 375 (2018) pp. 209–227,
URL: `https://doi.org/10.1016/j.jcp.2018.08.031`

[7] www.thewindpower.net ,
URL: `https://www.thewindpower.net/turbine_en_33_vestas_v90-3000.php`

[8] https://en.wind-turbine-models.com/ ,
URL: `https://en.wind-turbine-models.com/turbines/603-vestas-v90-3.0`

[9] APSLEY, D.D., CASTRO, I.P., *"A limited-length-scale $k-\epsilon$ model for the neutral and stably-stratified atmospheric boundary layer"* , Boundary-Layer Meteorology 83, pp. 75–98 (1997),
URL: `https://doi.org/10.1023/A:1000252210512`

[10] Panofsky, Hans A., and John A. Dutton, 1984, *"Atmospheric turbulence, models and methods for engineering applications"*, New York: Wiley

[11] Réthoré P E 2009 Wind Turbine Wake in Atmospheric Turbulence Ph.D. thesis Riso National Laboratory for Sutanaible Energy Technical University of Denmark

[12] Paul van der Laan and Niels N. Sørensen, *"Why the Coriolis force turns a wind farm wake clockwise in the Northern Hemisphere"*, English. In: Wind Energy Science 2 (2017), pp. 285–294. ISSN : 2366-7443,
`DOI : 10.5194/wes-2-285-2017`

[13] Zilitinkevich S S and Esau I N 2002 *"Boundary-Layer Meteorol."* 104 371–379

[14] Hess G D 2004 *"Boundary-Layer Meteorol."* 110 319–355

[15] Phillip McKay, Rupp Carriveau, David S-K Ting and Timothy Newson (November 21st 2012). Turbine Wake Dynamics, Advances in Wind Power, Rupp Carriveau, IntechOpen,
`DOI: 10.5772/53968.`
`URL: https://www.intechopen.com/books/advances-in-wind-power/turbine-wake-dynamics`